이학박사 학위논문

나노갭 에서의 전기장 증폭도 및 터널링 현상에 관한 연구

Optical field enhancement and tunneling phenomena in nanogaps

2018 년 2 월

서울대학교 대학원

물리천문학부

강 태 희

Optical field enhancement and tunneling phenomena in nanogaps

지도 교수 김 대 식

이 논문을 이학박사 학위논문으로 제출함
2018 년 2 월

서울대학교 대학원
물리천문학부
강 태 희

강태희의 이학박사 학위논문을 인준함
2018 년 2 월

위 원 장 차 국 린 (인)

부위원장 김 대 식 (인)

위 원 박 건 식 (인)

위 원 박 철 환 (인)

위 원 현 가 담 (인)

Abstract

In this thesis, I studied strong light-matter interaction in vertically aligned metal-insulator-metal nanogaps. Prepared nanogaps were evaluated by optical transmission measurement, exploiting Kirchhoff integral formalism and interferometric method. The measured optical field enhancements were in the order of ~ 10 and showed Fabry-Pérot resonance behavior coming from the waveguide mode of the nanogap. Due to the strong coupling between light field and metallic nanogaps, the transmitted light or photoluminescence of metal were greatly enhanced. For the field strength across the gap over ~ 1 V/nm regime, quantum tunneling process emerges, and it greatly modifies the optical response of the nanogaps. I measured and quantified the electromagnetically-driven ultrafast tunneling current using conventional electronics, exploiting the macroscopic symmetry of the closed ring barrier. Strong THz pulse was fully-rectified in the ring, and the spatiotemporal dynamics of the THz current was experimentally visualized by the optical probe method. This work will lead to the ultrafast optoelectronics, THz multiplexing, ultra-high bandwidth communications and wireless energy transfer technique.

Keywords: optical field enhancement, nanogap, interferometry, nonlinear optics, electron tunneling, terahertz rectification.
Student Number: 2011-20387

Table of Contents

Chapter 1. Introduction 1

Chapter 2. Fabrication of nanogap samples 3

Chapter 3. Measurement of optical field enhancement in nano gaps 5

3.1 Kirchhoff integral formalism 5
3.2 In case of negligible direct transmission 7
3.2.1 Transmission measurement for various gap sizes 9
3.2.2 Discussion on the resonance behavior 12
3.3 In case of non-negligible direct transmission 16
3.4 Resonantly enhanced photoluminescence of metal 21
3.5 Conclusion 25

Chapter 4. Tunneling phenomena in nanogaps 27

4.1 THz field and THz time domain spectroscopy 28
4.2 Light as a high-frequency current source 30
4.3 THz tunneling in triangular barriers 33
4.3.1 Theoretical method 36
4.3.2 Tunneling current measurement 38
4.3.3 Modeling triangle current 41
4.3.4 THz tunneling current estimation from THz-TDS 44
4.3.5 Effect of resonant THz field excitation 45
4.4 Optical probe of THz tunneling current transient 48
4.4.1 Modeling optical response 50
4.4.2 Optical field enhancement 52
4.4.3 Extracting tunneling duration time 54
4.4.4 Optical probing of spatiotemporal tunneling current 55
4.5 Ultrafast full-wave rectification of THz pulse 56
4.6 Conclusion 59

Chapter 5. Conclusion 61

Appendix. 63
A.1 Kirchhoff integral for wide-angle colleciton experiments 63
A.2 Theoretical calculation of electromagnetic fields near the metallic grating composed of 4-layers 68

Bibliography 73

Abstract in Korean 79

List of figures

Figure 2.1 Fabrication procedure of nanogap samples. (a) Metal patterning by photolithography. (b) Few nanometer Al2O3 deposition. (c) Metal deposition directly over the previous sample. (d) Removing additional metal blocks. 3

Figure 3.1 Diffraction geometry of slits punctured through a metallic screen. 6

Figure 3.2 Optical properties of gold and silver in visible – near infrared range. (a) Real part and (b) imaginary part of dielectric function of Au and Ag. Each data is adopted in ref [1]. Real part is related to the amount of induced charges by external fields, and imaginary part indicates the absorption. A good metal has large (negative) real part and small imaginary part. (c) Calculated direct transmission of Ag film for various metal thickness as a function of wavelength, indicated as black line. Dots denotes the measured direct transmission of Ag film used in this section. 8

Figure 3.3 (a) 1.5 nm gap sample, taken by a transmission optical microscope. Rectangular rings of 80 μm × 20 μm size are periodically arranged in a 200-nm-thick Ag film. (b) Cross-sectional SEM image of a gap region. (c) Magnified cross-section image of an Al2O3 layer, taken by TEM. 9

Figure 3.4 (a) Setup schematics of optical transmission measurement. Supercontinuum light source was used and transmission spectrum was analyzed by a monochromator equipped by PMT and InGaAs. (b) Spectrum of light source. (c) Detection range of PMT and (d) InGaAs, used in experiments. 10

Figure 3.5 (a) Measured transmission and (b) field enhancement for 1.5, 3 and 8 nm gap samples. 11

Figure 3.6 Schematics of surface plasmon polaritons (SPPs) propagating over a grating surface. (b) Revealed SPPs dispersion from measured nanogap transmission near SPPs wavelength as a function of incident angle. 12

Figure 3.7 (a) Schematics for a calculation of electromagnetic response of 1-dimensional nanogap array. (b) Calculated zeroth order transmission and field enhancement spectra for 2, 4, 6 and 8 nm gap sample. (c) Electric near field

distribution for 8 nm gap at resonant wavelength of 1653 nm (right) and 830 nm (left). 14

Figure 3.8 Evolution of (a) resonance wavelengths and (b) field enhancements as a function of gap size. Experiments are indicated as filled symbols with solid lines, while calculations are indicated as vacant symbols with dashed lines. The lines are categorized as waveguide mode numbers. 15

Figure 3.9 Near field distribution over (a) a nanogap and (b) a bare metal film under electromagnetic field incident. 16

Figure 3.10 (a) Optical microscope image of nanogaps. Pattern size of 25 × 25 μm in a 200-nm-thick Au film. (b) Measured transmission of nanogaps and bare Au film. (c) Measured CCD images of directly transmitted field through the bare Au film and nanogap samples of various gap sizes. All images are auto-contrasted. 17

Figure 3.11 Interferometry setup for optical phase measurement on metal film. PBS: polarizing beam splitter, BS: beam splitter. 18

Figure 3.12 (a) CCD image of 25 × 25 μm ring-patterned 1 nm gap sample under polarized laser field illumination. Note that only the side lines of the square ring of nanogaps are seen due to the laser polarization. (b) Optical phase map of the sample (a). Phase angle in color bar is expressed in degree. (c) Optical CCD image under laser illumination. Extracting phase information from the measured interferogram by dividing slit region and metal region, then I averaged out the diffraction pattern by areal averaging. (d) Interferogram signal as a function of delay for a nanogap and metal region. (e) Extracted phase information for various nanogap sizes. Error bars indicate standard deviation for the averaging process. (f) Estimated field enhancement factor of nanogaps.. 20

Figure 3.13 Calculated field enhancement factor as a function of gap sizes and metal thickness, compared with the experimentally estimated field enhancement. 21

Figure 3.14 CCD images of PL signals from nanogap, under (a) vertical and (b) parallel polarization exciatation with respect to the nanogap direction. Arrows indicate incident polarization of excitation beam and dashed line is a guide for the eye. (c) Measured spectra for each polarization. 22

Figure 3.15 (a) Measured PL signal under various conditions with the same excitation power of 10 mW. (b) PL signal of 5 nm gap before and after the etching of gap material. 23

Figure 3.16 Normalized PL signal for various gap positions on the same sample. All data are smoothed (nearest-neighbor averaging, without reducing the spectral resolution of the spectrometer) to clearly show the resonance positions. Colored arrows are guide for the eye, denoting the spectral peak positions.....24

Figure 3.17 Field enhancement factor of 1 nm gap with 200 nm thickness Au samples, in frequency range from THz to visible. Dotted line is 1/*f* fitting of field enhancement, indicating capacitive charging of a nanogap. Because of the resonant cavity mode of our nanogap samples at optical – near-infrared frequencies, the field enhancement factor is 10 times larger than that is anticipated from the 1/*f* line. THz data were imported from the reference [11].. 25

Figure 4.1 Various applications of electromagnetic waves on its frequency range. THz lies between microwaves and infrared.....28

Figure 4.2 (a) High power THz-TDS setup with current measurement units. (b) Time trace of incident electric field and (c) its FFT amplitude.. 29

Figure 4.3 Geometry dependent charging dynamics of metallic electrodes, driven by (a) a voltage source and (b) a current source.....31

Figure 4.4 Description of light driven surface current on a perfect conductor determined by the Maxwell boundary conditions. (b) A nanogap as a capacitor charged by incident electromagnetic waves and (c) resultant field enhancement as a function of frequency showing 1/f behavior [2].....32

Figure 4.5 (a) Schematic for tunneling current measurement under single-cycled THz pulse illumination (b) Optical scattering image and (c) SEM image of triangle nanogaps. Here the pattern size is 70 μm and period is 140 μm. Inset: cross-sectional TEM image of 2 nm gap.....33

Figure 4.6 (a) Surface current K charges the triangular nanogap. (b) Oscilloscope screen showing current pulse generated under THz pulse illumination. (c) Time trace of incident THz field and (d) expected induced voltage across gap trace under capacitive charging.....34

Figure 4.7 Potential distribution and subsequent total tunneling current through the ring barrier as a function of incident polarization in (a) an equilateral triangle and (b) a square.. 36

Figure 4.8 Schematic of 1-dimesional tunneling through Al2O3 barrier under applied time-dependent bias. 37

Figure 4.9 Measured tunneling current of a triangle barrier (side length of 70 μm, gap size of 2 nm) under (a) a DC bias and (b) THz field illumination.38

Figure 4.10 THz transmission of nanogaps (side length of 70 μm, each triangle pattern was separated by 140 μm) by changing incident field strength. (a) Time trace data and (b) its FFT amplitude as a function of incident field strength, normalized by incident field strength through quartz substrate. Here, maximum incident field was 400 kV/cm and the illuminated field strength is denoted as percentage. 39

Figure 4.11 Combined experimental data of static DC measurement and transient THz current data with fitting line based on the Simmons formula. 41

Figure 4.12 (a) Model diagram for total tunneling current through triangle barrier under surface current incident. (b) Calculated total current under polarization rotation and (c) its polar plot, showing three-fold rotational symmetry of a triangle. Black triangle line in (c) is a guide for eye. 42

Figure 4.13 (a) Polarizer angle dependent tunneling current measured for a 70-μm-sized triangle and a 25-μm-sized square. Fitting line is based on modeling presented previously. (b) Reconstructing fitting line acquired in (a) (dashed line) by assuming the incident field maintain its field strength under the polarization rotation (black line) based on the previous toy model. (c) Polar plot of reconstructed curve acquired in (b) for triangle and square. Black lines are guide for the eye. (d) Cross-sectional SEM image for each triangle side, showing the non-perfectness of the barrier, resulting minute signal for the square and asymmetric triangle shape in (c).....43

Figure 4.14 (a) Estimated time-dependent charge accumulation dynamics on the nanogap by THz-TDS. (b) Extracted tunneling current transient by differentiating the tunneled Q in (a). 45

Figure 4.15 Normalized transmission of 10-μm-sized triangle in (a) time

domain and (b) frequency domain, showing resonance near 1.3 THz. A subsidiary peak near 1.6 THz is coming from water absorption. (c) Tunneling current of (c) non-resonant (70-μm-sized), (d) resonant (10-um-sized) and (e) symmetric square barrier (25-μm-sized) under DC biasing. 46

Figure 4.16 Numerical simulation result of 0.6-μm-sized triangle of 50 nm gap in a 50 nm thick PEC film by changing incident polarization. (a) Transmission spectra calculated, showing resonance in ~ 1.7 μm. Polarization dependent field distribution in resonance wavelength for (b) x polarized, (c) xy polarized and (d) y polarized case at the resonant wavelength.. 47

Figure 4.17 (a) Experimental scheme for THz tunneling current measurement under optical beam excitation. (b) Measured tunneling current under THz and optical field excitation, showing the optically induced current follows the THz gap voltage transient. Green dashed line is a guide for the eye, denoting THz voltage time profile (figure 4.6 (d)). Here, the side length of the triangle was 500 μm and gap size was 2 nm. (c) Optical polarization dependent current. 0 degree is defined as vertical to slit direction and 90 degrees as parallel to the slit direction. Incident optical power was relatively low compared with (b), showing only the peak current. 49

Figure 4.18 (a) Pictorial description for optical tunneling in a nanogap. A picosecond THz pulse and a femtosecond optical pulse are added and applies transient voltage across the gap. (b) Graphical illustration for optical tunneling under the quasi-constant THz field. Due to the strong nonlinearity of tunneling process, sinusoidal optical field generate tunneling current only for preferred polarity determined by THz field strength. Current vs. voltage relation was calculated based on the Simmons formula with barrier potential of 2.2 eV and gap size of 2 nm. 51

Figure 4.19 THz and optical field induced time profile of gap voltage (upper row) and tunneling current (bottom row). (a) Only the THz field illuminated, (b) optical beam incident with time delay of -0.5 ps with THz field and (c) 0 delay case. Inset of (c) show the magnified view near the zero delay. 52

Figure 4.20 (a) Optical spot size and effective current spot size arising from the highly nonlinear tunneling current. (b) Calculated effective spot size as a function of applied optical voltage. 52

Figure 4.21 (a) Experimental and (b) theoretical time dependent optical

current as a function of time delays. Legends in (a) indicate incident optical power and (b) applied optical field across a gap. Dashed line is a guide for the eye, indicating the THz gap voltage. 53

Figure 4.22 (a) Optical power dependent tunneling current in 70-μm-sized triangle barrier (gap size of 2 nm). Black arrow indicates the incident optical power. (b) Gaussian-fitted half-width of central peak (0 ps) as a function of incident optical field strength. 55

Figure 4.23 (a) Schematics of optical probing of spatiotemporal THz tunneling dynamics under a DC bias. (b) Positional dependent optical tunneling current under the THz polarization as vanishing current. (c) Local THz current probed by optical pulse under a DC bias which is denoted by DC bias strength on each curve. Greed dashed line indicates the THz voltage..56

Figure 4.24 A pictorial description of full-wave rectification of THz pulse in a ring-barrier (see figure 4.6 (a) for arc length notation). Time column shows the incoming voltage profile and two example timings are denoted as black arrows. The applied DC bias is denoted as gray bars and black line in potential distribution. The resulting current pulse has a single polarity independent of the driving pulse direction. 57

Figure 4.25 (Experimental demonstration of ultrafast full-wave rectification of THz tunneling current from a triangular ring barrier (side length of 100 μm, gap size of 4 nm), visualized by circularly polarized optical pulse. By changing the THz polarization (at top of the figure), the output THz current shape can be modulated. Green dashed line indicates the incident THz voltage.. 58

Figure 4.26 (a) Theoretical demonstration of ultrafast full-wave rectification (first row) and its optical current (second row) of incoming 1 THz continuous wave in a triangular ring barrier under DC bias. THz peak voltage of 1 V and optical voltage of 3 V was used for the demonstration.... 59

Figure 4.27 Position-sensitive optical switching device in (a) a triangle barrier and (b) a pentagon barrier. 60

Figure 4.28 Ultrafast current-pulse generator. Multiple optical pulses and THz wave illuminate on a single barrier with predefined delays, generating an arbitrary-shaped current pulses. 60

Figure A.1 Schematic for transmission measurement with high numerical aperture (N.A.) objective lens. Incident optical beam is focused at (a) a bare substrate and (b) a nanogap. Magnified view of the focused spot on (c) a bare substrate and (d) nanogap. Here, the focused optical beam is assumed to have uniform intensity profile in the beam spot. (e) Detection scheme under plane wave incident. 64

Figure A.2 Calculated error factor as a function of (a) collection angle and (d) wavelength. Beam size is assumed to 5 um and the gap size is 10 nm. (c) Estimated field enhancement of 10 nm gap measured by high N.A. (0.89) lens in optical regime, compared with low N.A. measurement. Corrected data are ended at 900 nm due to the source spectrum limit (Halogen lamp). 66

Figure A.3 Schematic for the electromagnetic field calculation near a metallic grating. 68

Chapter 1. Introduction

Nano optics is the study of the behavior of electromagnetic waves on the nanometer scale. Manipulating single molecules, quantum dots, or electrons by the light fields is one of the ultimate goal of the nano optics. Subwavelength nanostructures can confine the lights deep below the diffraction limit which cannot be attained by conventional optics. Field enhancement in the metallic nano junction is generally order of magnitudes larger than the incident field [1], making possible to initiate strong light-matter interactions that cannot be achieved by free space electromagnetic waves [2, 3]. Light confinement at nanometer scale has attracted many researches using various metallic nanostructures such as nanoparticles [4-9], nanogaps [1, 10-17] and sharp metal tips [18-20].

There are other factors affecting to the light-matter interactions. For example, the enhancement of the Raman cross-section is well known as a consequence of electric near-field enhancement on a rough metal surface [21, 22]. Additionally, there are also evidences for chemical effects, such as the modulation of the surface charge density of the metal by the molecules adsorbed directly on the metal surface, thereby increases the Raman cross-section [23, 24]. Understanding such complex phenomena in nanoscale thus requires appropriate quantification of electric field enhancement of nanostructures separately from other effects. In most cases, the quantification is performed by theoretical means or obtained in arbitrary units [22, 25], which does not fully reflect the actual experimental situations.

Therefore, the direct experimental verification of field enhancement factor is much needed to understand and exploit the light-matter interaction in nanoscale. In this thesis, I studied on the estimation of the field enhancement of nanogaps fabricated on optically thick and thin metallic film and analyzed in broad frequency range, visible and near infrared. With the help of the strong field enhancement in nanogaps, I also demonstrated the manipulation of tunneling electrons in nanogaps driven by external light fields.

Chapter 2. Fabrication of nanogap samples

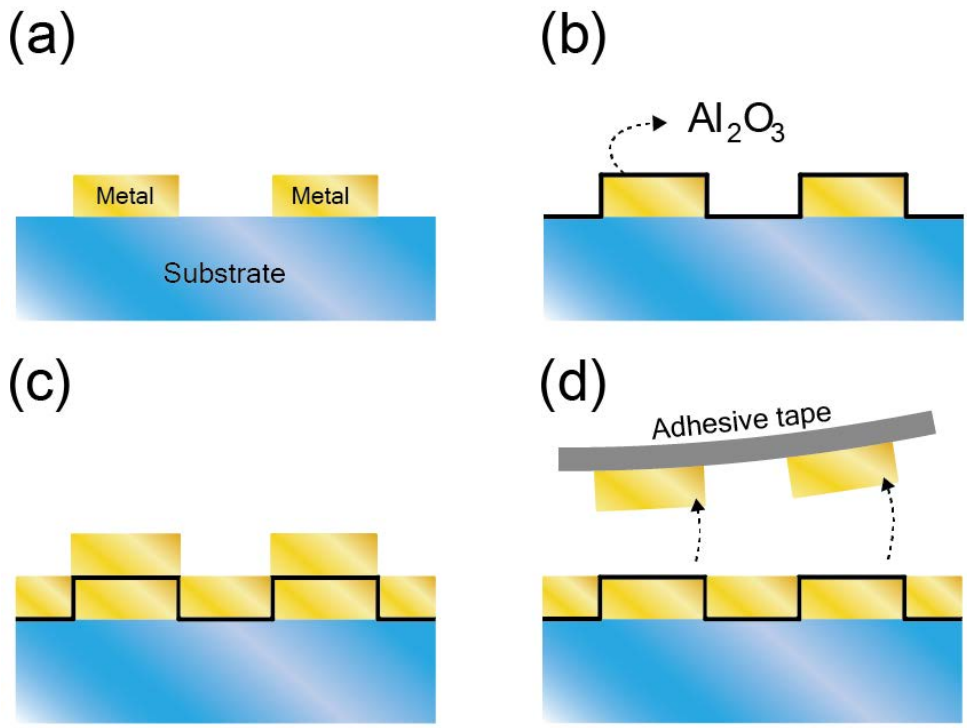

Figure 2.1 Fabrication procedure of nanogap samples. (a) Metal patterning by photolithography. (b) Few nanometer Al_2O_3 deposition. (c) Metal deposition directly over the previous sample. (d) Removing additional metal blocks.

In this work, the metallic nanogaps are prepared by the recently developed nanofabrication technique [10, 26, 27]. It is composed of conventional photolithography and subsequent metal deposition and atomic layer deposition (ALD). Detailed fabrication process is following (figure 2.1). On 500 μm-thick substrates (quartz, sapphire or silicon), AZ5214 image reversal photoresist was spin coated at 4000 rpm for 60 seconds then prebaked with 90 ℃ for 60 seconds. On the resist-coated substrates, I exposed UV lamp (wavelengths of 350 – 450 nm, beam intensity about 25 mW/cm^2) under prepared photomasks for 6 seconds. Then post baking was performed with 120 ℃ for 120 seconds. After 2nd exposure by the same UV light as the 1st exposure for 40 seconds, samples are developed by MIF500 solution for 30 –

60 seconds depending on the pattern sizes. After the deposition of metal sources (gold or silver) by an e-beam evaporator or by a thermal evaporator and the subsequent lift-off process using acetone with a 1 minute sonication (figure 2.1 (a)), an insulating Al_2O_3 layer was coated by the ALD, which determines the size of the gap (figure 2.1 (b)). After this, another metal layer was deposited directly onto the previous patterns (figure 2.1 (c)). Finally, an adhesive tape was applied to the sample to planarize the sample surface (figure 2.1 (d)).

Chapter 3. Measurement of optical field enhancement in nanogaps

Experimental quantification of field enhancement factors has been discussed in earlier studies, through the far-field transmission measurement of a metallic slit in terahertz frequency range [1, 10] and at a Ti:Sapphire laser wavelength of 800 nm [13]. The key method was applying the Kirchhoff integral formalism to the measured transmission [28, 29], which makes possible to directly estimate field enhancement factors of subwavelength gaps by the transmission measurement. However, the considered spectral ranges were confined in the terahertz, or limited in the narrow band near 800 nm, hindering further elucidation of the resonant features anticipated at near-infrared wavelengths [13]. In this chapter, I studied the field enhancement of nanogaps in visible – near-infrared wavelength range (0.6 – 2.3 μm) where diverse researches have been performed such as Raman spectroscopy [21, 23, 30-34] and nonlinear studies [35-39].

Performing optical characterization of the metallic nanogap, a main hurdle is its extremely low intensity transmitted through the gap, which hampers experimental detection of the transmitted light separately from the background field transmitted directly through the metallic film; increasing an intensity of incident fields simultaneously induces an increase of background signal, which interferes the field enhancement estimation. Therefore, care must be taken to measure the metallic nanogap in optical – near-infrared range.

3.1 Kirchhoff integral formalism

The Kirchhoff integral formalism is useful for the experimental measurement of electric field enhancement of subwavelength structure, since it relates the far-field amplitude to the near-field amplitude of the electric fields in that structures. For apertures punctured through a metallic screen, the diffracted electric field **E** at observation point **r** located far from the

apertures is given by the Kirchhoff integral [29] (figure 3.1),

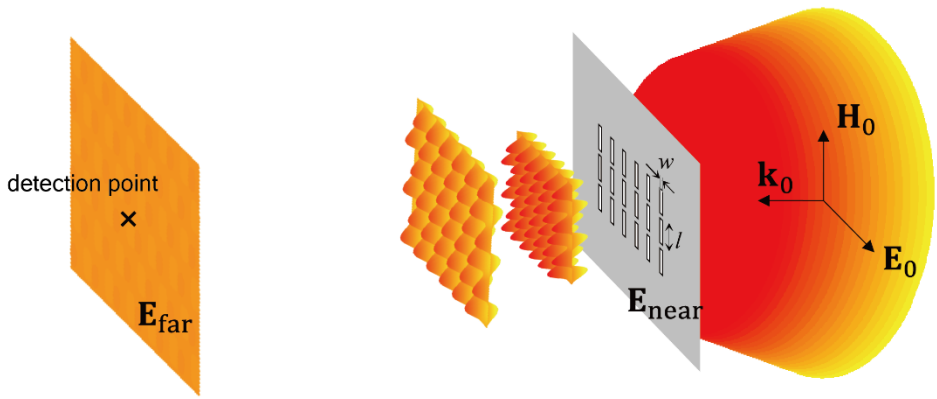

Figure 3.1 Diffraction geometry of slits punctured through a metallic screen.

$$\mathbf{E}(\mathbf{r}) = \frac{ie^{ikr}}{2\pi r}\mathbf{k} \times \int_{\text{screen}} \mathbf{n} \times \mathbf{E}(\mathbf{r}')e^{-i\mathbf{k}\cdot\mathbf{r}'}da' \tag{3.1}$$

where r is the distance from the center of the aperture to the observation point, **n** the normal vector to the metal screen directed toward observation point, and **k** is the wavevector of the electromagnetic wave directed to the observation point. Considering that the detection point is placed normal to the sample, equation 3.1 can be reduced to

$$\mathbf{E}_{\text{far}} = \frac{e^{ikr}}{i\lambda r}\int_{\text{screen}} \mathbf{E}_{\text{near}}(\mathbf{r}')\, da' \tag{3.2}$$

Thus, electric far-field at the detector is directly related to the summation of electric near-field on the sample plane. From the transmission measurement, detected signal of nanogap samples and bare substrate is,

$$\begin{aligned} E_{\text{sample}} &\propto \int_{\text{screen}} E_{\text{near}} da' \\ &= \int_{\text{gap}} E_{\text{gap}} da' + \int_{\text{metal}} E_{\text{direct}} da' \\ &\cong \langle E_{\text{gap}} \rangle \times (\text{gap area}) \end{aligned} \tag{3.3}$$

$$E_{\text{ref}} \propto \int_{\text{spot}} E_0 da' = E_0 \times (\text{spot size}) \tag{3.4}$$

where the bracket means the averaged near field component over the slit area. In equation 3.3, the integral term related to the direct transmission (transmitted field directly through the metal film) is ignored and the gap field is assumed to be a constant over the gap area. Then, the electric field enhancement factor can be written by

$$\left|\frac{E_{\text{gap}}}{E_0}\right| = \frac{t}{\beta} \tag{3.5}$$

where $t = |E_{\text{sample}}/E_{\text{ref}}|$ is a nanogap transmission amplitude and β is defined by the gap area divided by the spot size. In my measurements, the illuminated area, or the spot size, is relatively large compared to periodicity of the nanogaps in the sample. Then β becomes simply the coverage ratio of the sample (ratio between gap area and unit cell area).

3.2 In case of negligible direct transmission

In this section, I consider the specific case when the direct transmission is relatively small compared to a field through the gap, i.e., exploiting equation 3.5. To accomplish this, I adopted silver (Ag) for nanogap fabrication, which show good metallic property in visible range (figure 3.2 (a) and(b)) compared with other frequently used noble metals such as gold (Au) or aluminum (Al), with sufficient metal thickness to safely block the direct transmission up to the level which does not hinders the gap signals. I used 200-nm-thick Ag film for nanogap samples. The dotted line in figure 3.2 (c) shows the measured direct transmission of Ag film. For the considered wavelength range over 600 nm, the direct transmission was well below an order of 10^{-8}: safely ignorable signal compared with a gap signal. There is a discrepancy of 20 nm of metal thickness between measurement and calculation, possibly from the slight-mismatch of refractive indices between Ag sample I used and adopted data [40] for the calculation.

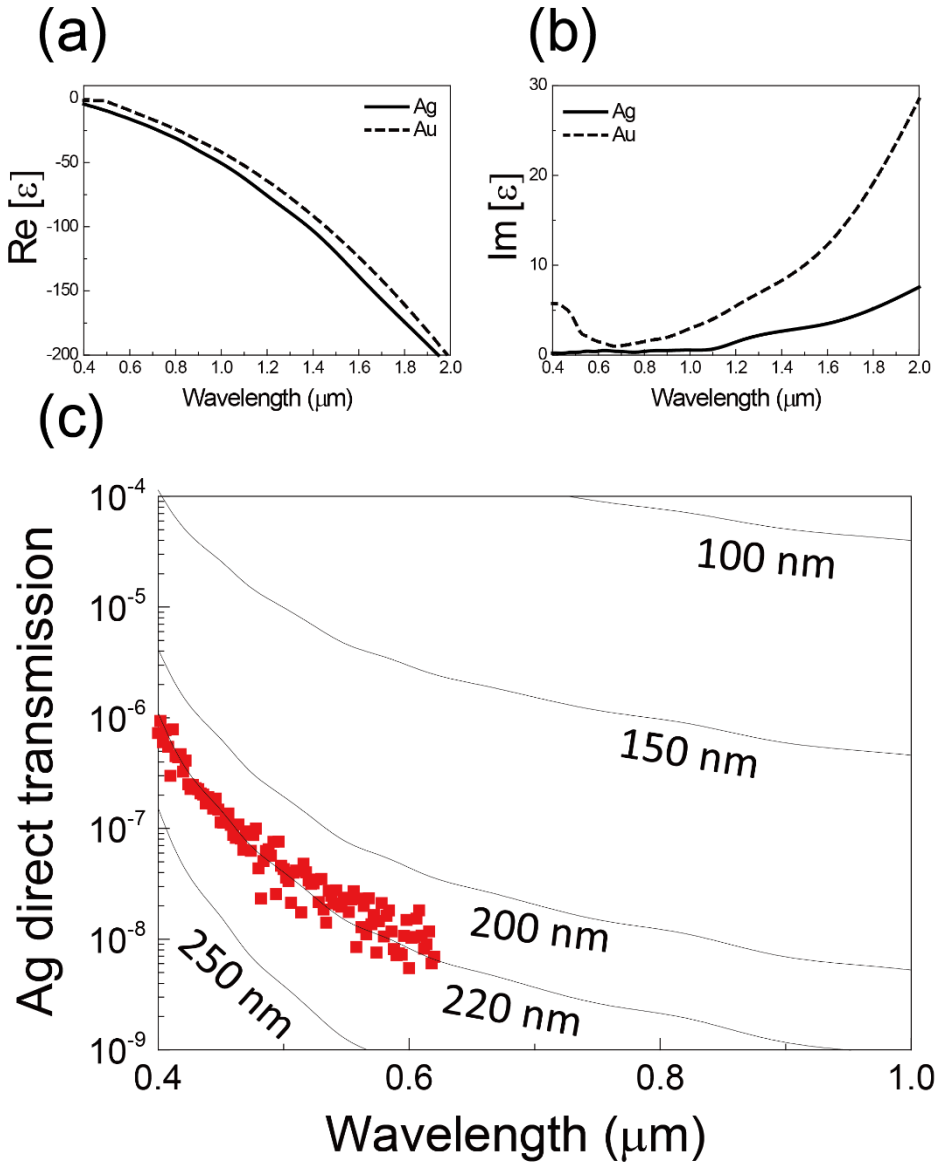

Figure 3.2 Optical properties of gold and silver in visible – near infrared range. (a) Real part and (b) imaginary part of dielectric function of Au and Ag. Each data is adopted in ref [40]. Real part is related to the amount of induced charges by external fields, and imaginary part indicates the absorption. A good metal has large (negative) real part and small imaginary part. (c) Calculated direct transmission of Ag film for various metal thickness as a function of wavelength, indicated as black line. Dots denotes the measured direct transmission of Ag film used in this section.

3.2.1 Transmission measurement for various gap sizes

I prepared nanogap samples whose gap size of 1.5, 3 and 8 nm. The gaps are composed of 80 μm × 20 μm-sized ring array, separated each other by 20 μm (figure 3.3 (a)).

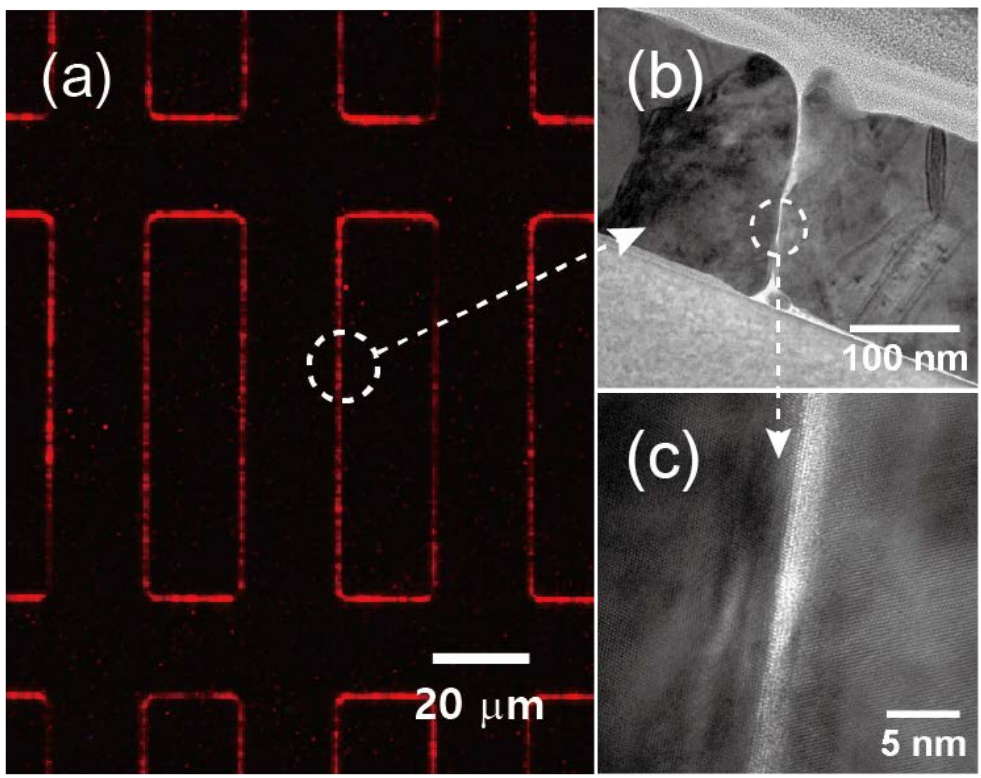

Figure 3.3 (a) 1.5 nm gap sample, taken by a transmission optical microscope. Rectangular rings of 80 μm × 20 μm size are periodically arranged in a 200-nm-thick Ag film. (b) Cross-sectional SEM image of a gap region. (c) Magnified cross-section image of an Al_2O_3 layer, taken by TEM.

For optical transmission measurements (figure 3.4), I used a white-light supercontinuum laser (SC400, Fianium) which covers wavelengths from 400 nm to 2200 nm range. I placed spectrally-calibrated neutral density filters to match the incident beam intensities between reference measurements and sample detections, since the sample transmission was an order of ~ 10^{-6}: out of range of the detector's dynamic range.

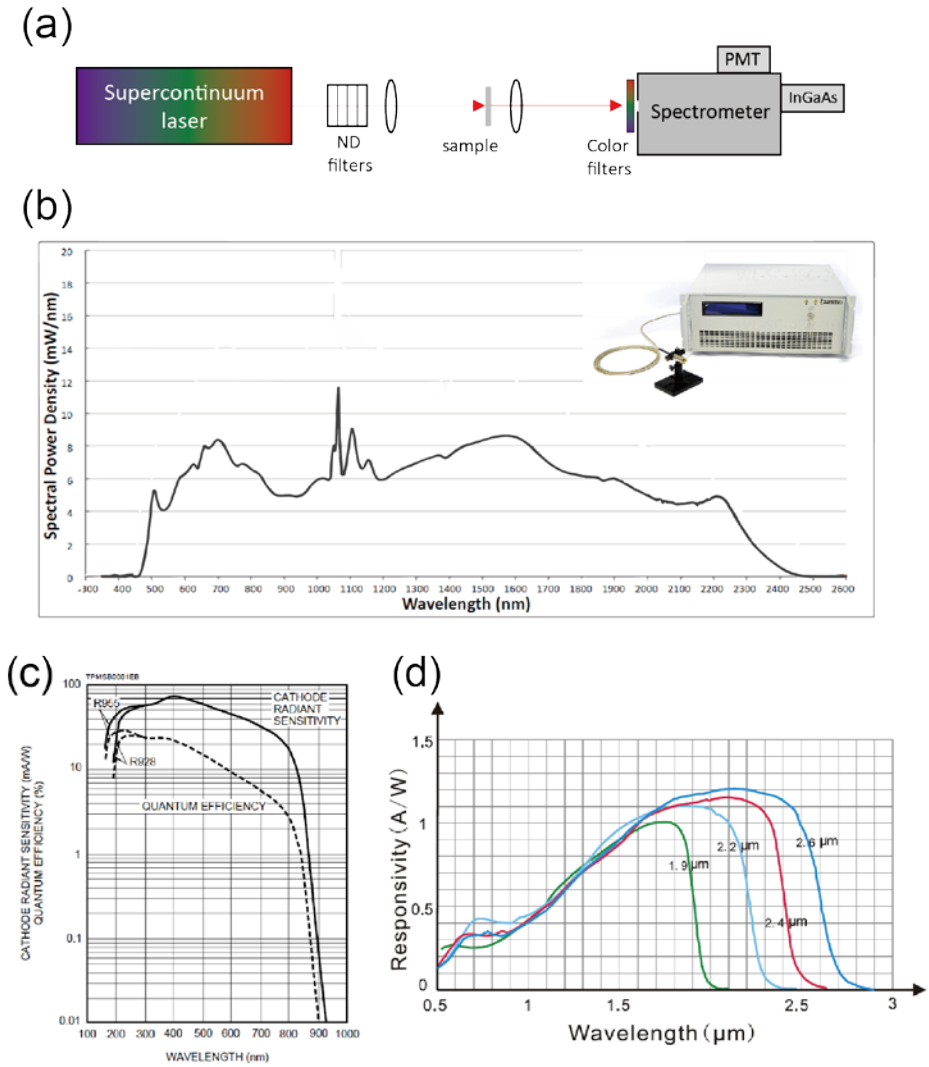

Figure 3.4 (a) Setup schematics of optical transmission measurement. Supercontinuum light source was used and transmission spectrum was analyzed by a monochromator equipped by PMT and InGaAs. (b) Spectrum of light source. (c) Detection range of PMT and (d) InGaAs, used in experiments**.**

Transmitted light through the sample is analyzed by a monochromator, equipped by a set of detectors, a photomultiplier tube (PMT) and an indium gallium arsenide (InGaAs) detector. The PMT detects in visible wavelength range, specifically from 600 nm to 820 nm, and the InGaAs covers the detection spectrum from 800 nm to 2200 nm. I used two different

monochromator gratings; one was 1200 grooves/mm (blazed at 750 nm) for visible range measurement and the other was 600 grooves/mm (blazed at 1600 nm) for near-infrared detection. To avoid the spectral overlapping in the grating dispersion, e.g. the 1st order diffraction of 800 nm and overlapped 2nd order diffraction of 400 nm at the same spectral position, I placed proper sets of long-pass filters in front of the monochromator. The laser beam impinges to the sample in normal direction, focused by a lens whose focal length of 300 mm, having a spot size of ~ 300 μm with a vertical polarization to the long axis of the rectangle (80 μm side), illuminating ~ 50 gaps at the same time. This linear polarization makes our samples function as one-dimensional diffraction gratings since the metallic nanoslit transmission efficiency for the vertical polarization to the slit axis (TM incidence) is much higher than that for the parallel polarization (TE incidence) [41].

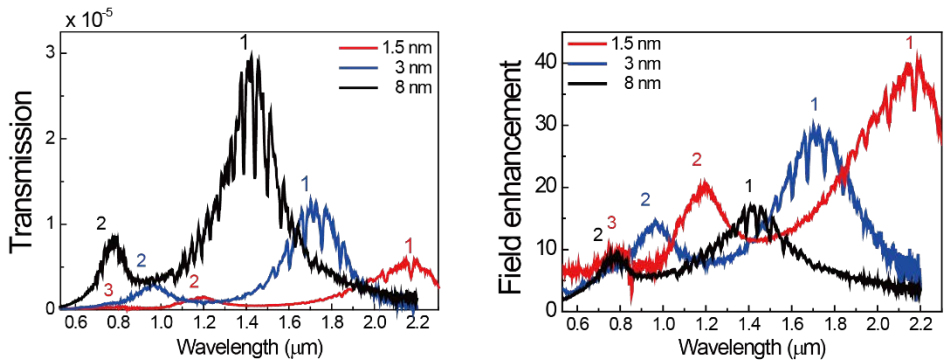

Figure 3.5 (a) Measured transmission and (b) field enhancement for 1.5, 3 and 8 nm gap samples.

On the measured transmission spectra (figure 3.5 (a)), I applied the Kirchhoff integral formalism to estimate the near-field enhancement of the nanogaps. With the measured transmission and coverage ratio of the nanogaps relative to the total illuminated area ($\beta = 6 \times 10^{-5}$, 1.2×10^{-4}, and 3.2×10^{-4} for 1.5, 3 and 8 nm gaps, respectively), I can obtain the field enhancement factor using equation 3.5 (figure 3.5 (b)).

In addition to the resonance peaks in transmission spectra, there exist subsequent dips with an asymmetric line shape, embedded in each curve. These dips are resonant Wood's anomalies [42], which originate from the

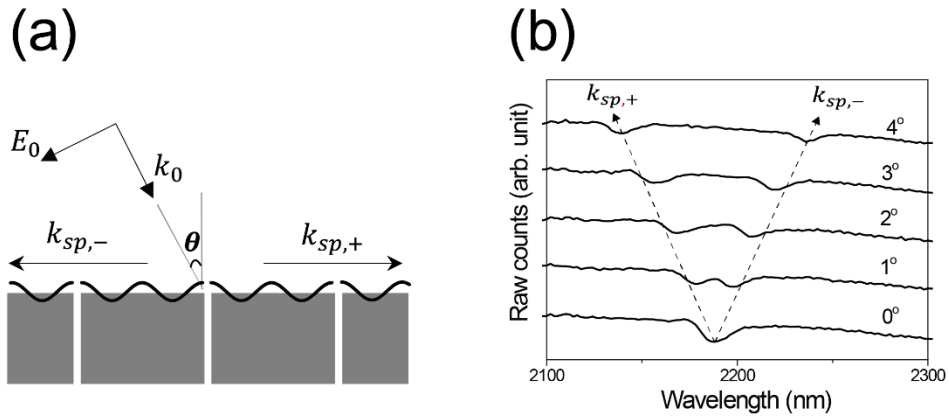

Figure 3.6 (a) Schematics of surface plasmon polaritons (SPPs) propagating over a grating surface. (b) Revealed SPPs dispersion from measured nanogap transmission near SPPs wavelength as a function of incident angle.

interference between the resonantly excited surface plasmon polaritons (SPPs) and the transmitted light through the gaps [43]. In my case, the grating period d = 20 μm gives a surface momentum $G = n(2\pi/d)$ to the incident waves (figure 3.6 (a)), where n is an integer. By matching this momentum to the SPP dispersion, i.e., $\Delta k_{spp}=\Delta G$, the spectral spacing of the dips for normal incidence can be calculated by,

$$|\Delta\lambda|_{dip} = \lambda \frac{2\pi}{k_{spp} d} \tag{3.6}$$

At λ = 1 μm, Δλ is given by ~ 40 nm, which is the similar spacing shown in figure 3.5. Wavevector of incident light k_0 with oblique angle θ_{inc} can give additional surface momentum $k_0 \sin\theta_{inc}$, thus affecting to the spectral dip positions. I confirmed that the dips are divided into two different direction as a function of incident angle, as shown in figure 3.6 (b), indicating that the spectral dips are originated from the Wood's anomalies.

3.2.2 Discussion on the resonance behavior

To check the validity of the measured field enhancmenet and behavior of resonance, I calculated an electromagnetic response of the nanogaps periodically arranged in a one dimension (figure 3.7 (a)). A monochromatic, transverse-magnetic (TM) polarized plane wave impinges

normal to the sample plane, in a direction from a substrate side (expeirmental situation). The magnetic fields near the sample placed at the *xz* plane, can be represented in terms of mode expansion [44] (detailed calculation process is presented in Appendix A.2),

$$H_{\mathrm{I}}(x,z) = e^{ik_{\mathrm{I}}z} + \sum_{n=-\infty}^{\infty} r_n e^{i\mathbf{k}_{\mathrm{I},n}\cdot\mathbf{r}} \tag{3.7}$$

$$H_{\mathrm{II}}(x,z) = \sum_{m=0}^{\infty} \left(e^{i(\mathbf{k}_{\mathrm{II}})_{x,m}x} + C_m e^{-i(\mathbf{k}_{\mathrm{II}})_{x,m}x}\right) \times \left(a_m e^{i(\mathbf{k}_{\mathrm{II}})_{z,m}z} + b_m e^{-i(\mathbf{k}_{\mathrm{II}})_{z,m}z}\right) \tag{3.8}$$

$$H_{\mathrm{III}}(x,z) = \sum_{n=-\infty}^{\infty} t_n e^{i\mathbf{k}_{\mathrm{III},n}\cdot\mathbf{r}} \tag{3.9}$$

where r_n, t_n, C_m, a_m, b_m are unknown mode coefficients and m, n are mode numbers. The x-component wavevectors are given by $(\mathbf{k}_{\mathrm{I}})_{x,n} = (\mathbf{k}_{\mathrm{III}})_{x,n} = n(2\pi/d)$, indicating the diffracted field by the grating. The grating period d and the thickness h were set to 20 μm and 160 nm, respectively. The refractive index of the metal (Ag) was adopted from a reference [45]. The refractive index of substrate (region I) and gap (region II) were set to be 1.76, which corresponds to the bulk index of sapphire and Al_2O_3 in the visible frequency range. The mode coefficients can be determined by using Maxwell boundary conditions. At metal boundaries, I imposed the surface impedance boundary condition $\mathbf{E}_{\parallel} = n_m^{-1}(\mathbf{n} \times \mathbf{H})_{\parallel}$, where n_m is the refractive index of metal and $\mathbf{n}$ is the normal vector to the metal surface, which gives reasonable results well below the plasma frequency of the metal [46, 47]. Figure 3.7(b) shows the calculated zeroth-order transmission coefficients (top) and field enhancement factors (bottom) as a function of incident wavelength for gap sizes of 2, 4, 6, and 8 nm. The field enhancement factors were extracted by averaging the electric field amplitudes at the boundary of regions II and III, where the transmitted waves emanated from the gap.

Since the gap size is in nanometer scale, which is far below the wavelength of incident field, the dominant propagating mode inside the gap (region II) is only the fundamental mode ($m = 0$) in equation 3.8 [41, 48]. In this single-mode approximation, the counter propagating modes, $\exp(i(\mathbf{k}_{\mathrm{II}})_{z,m}z)$

and exp(-i($\mathbf{k}_{II}$)$_{z,m}z$) in equation 3.8, can interfere constructively with each other when the cavity length is matched to the multiples of half wavelength of the mode. This leads to the Fabry-Pérot-like resonance at specific wavelengths. I plotted the electric field distribution |$\mathbf{E}_x$| near the 8-nm-sized gap under resonance condition in figure 3.7(c), describing the formation of standing waves inside region II in the cases of 1st (left) and 2nd (right) modes.

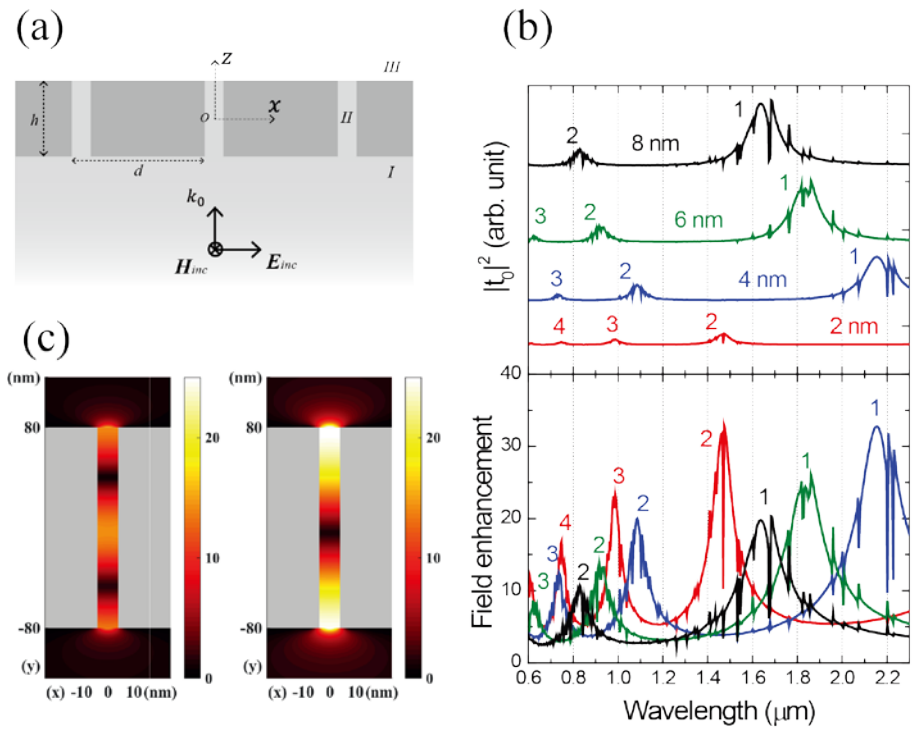

Figure 3.7 (a) Schematics for a calculation of electromagnetic response of 1-dimensional nanogap array. (b) Calculated zeroth order transmission and field enhancement spectra for 2, 4, 6 and 8 nm gap sample. (c) Electric near field distribution for 8 nm gap at resonant wavelength of 1653 nm (right) and 830 nm (left).

I compared the measured field enhancements with the calculation results in figure 3.8. The resonance peak wavelength increases for narrower gaps and the change becomes more abrupt as the gap approaches the nanometer scale. Such a red-shifting behavior of the resonance peak (i.e., the evolution of the mode wavelength as a function of a nanogap size) can be

understood from the plasmon dispersion in the metal–insulator–metal structure [49]. The resulting effective refractive index of a gap material increases by narrowing the gap size. For a fixed metal thickness, therefore, the narrow nanogap leads to a red shift of resonance wavelength.

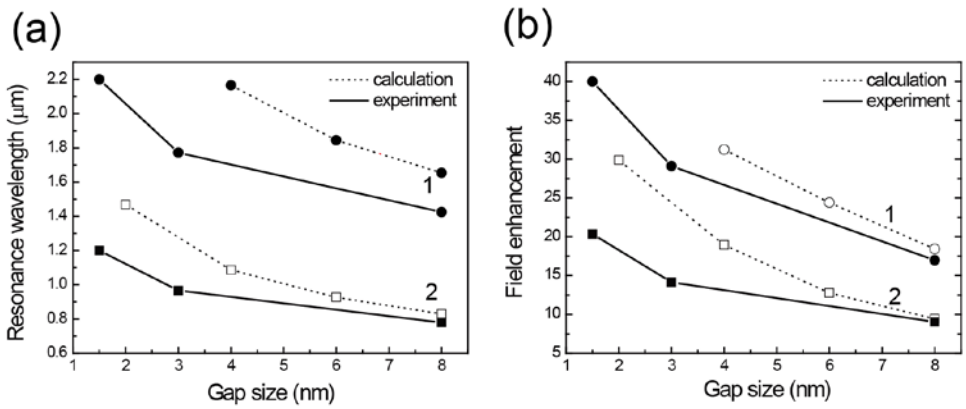

Figure 3.8 Evolution of (a) resonance wavelengths and (b) field enhancements as a function of gap size. Experiments are indicated as filled symbols with solid lines, while calculations are indicated as vacant symbols with dashed lines. The lines are categorized as waveguide mode numbers.

The discrepancy between experiment and calculation would be coming from the fact that the calculation model does not fully reflect the experimental sample structure. For example, the modification of the refractive index of the thin film [50] affects to the resonance wavelength position. Also, as one can see, the cross-sectional view of nanogap shape is not perfectly vertical to the substrate (making sub-90 degrees with substrate, shown in figure 3.3 (b)), introduced from the 1st metal deposition process. This tilt angle and tapered gap structure can be understood effectively by an elongated or shorten metal thickness (or cavity length), affecting resonance frequency of the optical transmission (I chose cavity length of 160 nm in the model for the best fit to the experiments). However the gap size, defined by the ALD process, is not much changed by the mentioned effects. Field enhancement factor also does not affected severely, taking only the slight change of the spectral properties since the accumulated charges across the gap induced by the optical surface currents keeps the same for a constant gap size [1, 51].

3.3 In case of non-negligible direct transmission

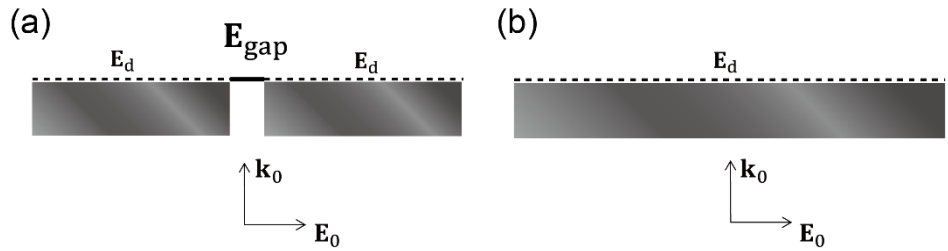

Figure 3.9 Near field distribution over (a) a nanogap and (b) a bare metal film under electromagnetic field incident.

In this section, I consider the case when the direct transmission is comparable to the gap signal; previous assumption of ignoring direct transmission term in equation 3.3 does not valid now. Transmission through the sample contains not only the gap field but also the non-negligible metal field (figure 3.9 (a)), thus equation 3.3 should take all terms,

$$E_{\mathrm{far,g}} \sim \int E_{\mathrm{gap}}\, dA_{\mathrm{gap}} + \int E_{\mathrm{d}}\, dA_{\mathrm{d}} \tag{3.10}$$

without discarding the direct transmission term. To avoid the unwanted direct signal, I separately measured the direct transmission (figure 3.9 (b)),

$$E_{\mathrm{far,d}} \sim \int E_{\mathrm{d}}\, dA_{\mathrm{d}} \tag{3.11}$$

Here, the areal mismatch between direct integral term in equation 3.10 and 3.11 (A_{d}) can be safely ignored since the coverage ratio of the nanogap is extremely small (order of 10^{-5}). Note that the measured quantity in optical frequency is the intensity, rather than the field amplitude. Therefore, I need another information to subtract the direct signal from the measured transmission: the phase difference between the gap field and direct field.

To estimate the field enhancement by subtracting the direct transmission, first I measured the sample transmission T_{sample},

$$T_{\mathrm{sample}} = \left| \frac{A_{\mathrm{d}} E_{\mathrm{d}} e^{i\theta} + A_{\mathrm{g}} E_{\mathrm{gap}}}{A\, E_0} \right|^2 = \left| \frac{E_{\mathrm{d}}}{E_0} e^{i\theta} + \beta \frac{E_{\mathrm{gap}}}{E_0} \right|^2 \tag{3.11}$$

where E_0 is the incident field amplitude, E_{gap} the gap field amplitude, E_{d} the

direct field amplitude, A the illuminated area and θ is the phase difference.

Next I measured direct transmission T_{d},

$$T_{\mathrm{d}} = \left|\frac{E_{\mathrm{d}}}{E_0}\right|^2 \tag{3.12}$$

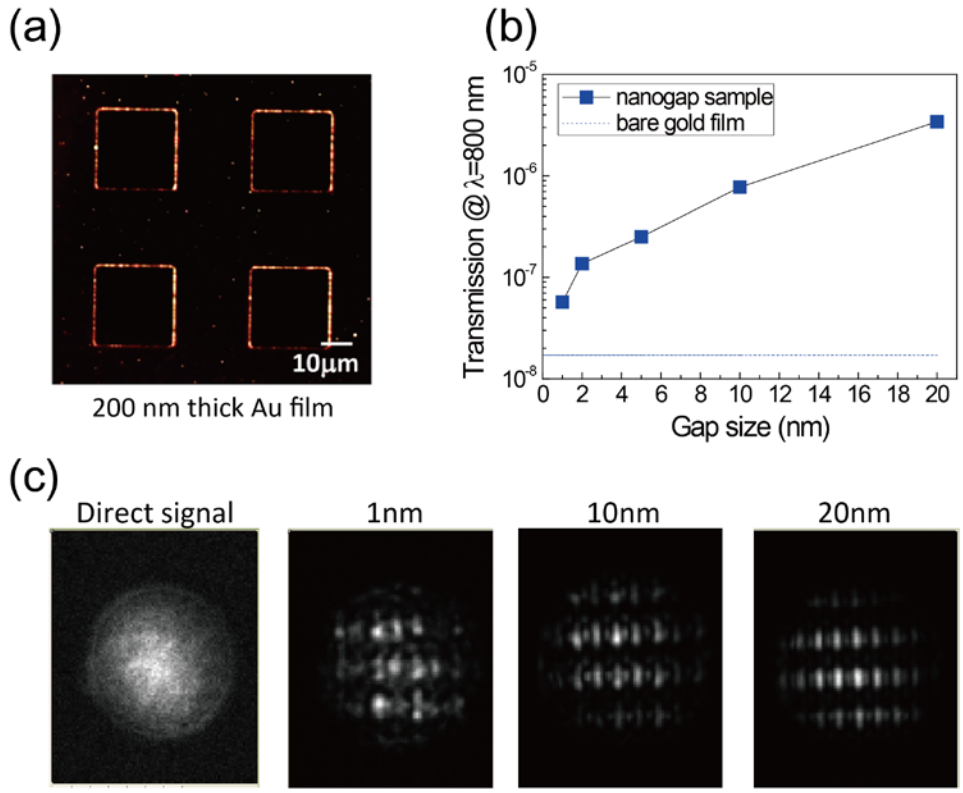

Figure 3.10 (a) Optical microscope image of nanogaps. Pattern size of 25 × 25 μm in a 200-nm-thick Au film. (b) Measured transmission of nanogaps and bare Au film. (c) Measured CCD images of directly transmitted field through the bare Au film and nanogap samples of various gap sizes. All images are auto-contrasted.

With all the information mentioned above, I can estimate the field enhancement as following

$$\left|\frac{E_{\mathrm{gap}}}{E_0}\right| = \frac{1}{\beta}\left[\sqrt{T_{\mathrm{sample}} - T_{\mathrm{d}}\sin^2\theta} - \sqrt{T_{\mathrm{d}}}\cos\theta\right] \tag{3.13}$$

Figure 3.10 (a) shows 25 μm × 25 μm ring-shaped nanogap sample

fabricated in a 200-nm-thick Au film. I prepared 1, 2, 5, 10 and 20 nm gap samples and a bare gold film of the same thickness. I used a Ti:Sapphire 800 nm wavelength laser. Charge coupled device (CCD), PMT and APD are exploited for detection; I repeated measurement several times for the same sample with different detectors to check the reliability of the detected signal level because the sample transmission of small nanogap is almost the same order as the direct transmission (figure 3.10 (b)). As the gap sizes decrease down to nanometer scale, direct signal and sample signal becomes comparable.

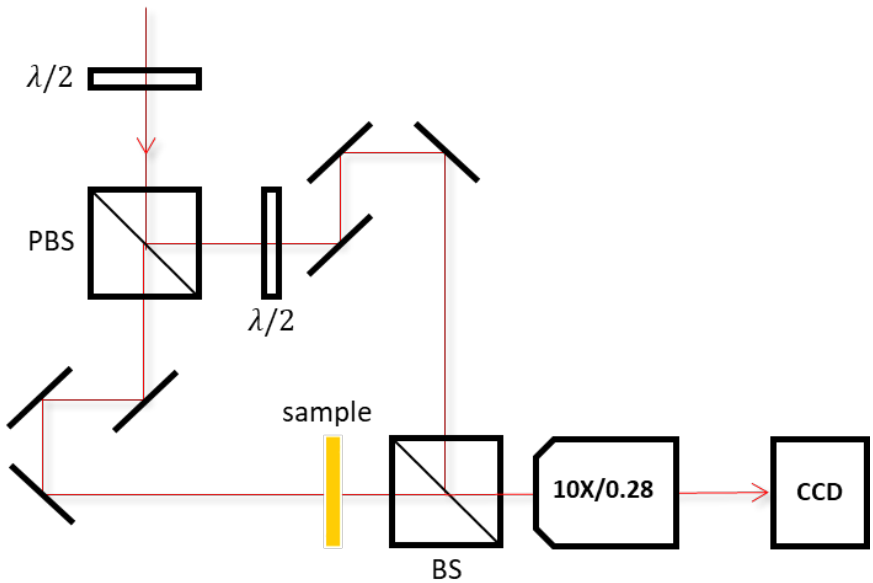

Figure 3.11 Interferometry setup for optical phase measurement on metal film. PBS: polarizing beam splitter, BS: beam splitter.

Next, I performed measurement using Mach-Zender type interferometry setup to extract phase difference between gap field and metal field (figure 3.11). I used a mode-locked Ti:Sapphire laser (800 nm wavelength, 200 fs pulse width) rather than a continuous wave which generate phase noise on the detector plane due to the multiple reflection generated from the optics (such as the beam splitter, BS). To balance and control the beam intensities of each delay arm, I used polarizing beam splitter and a set of half wave plates ($\lambda/2$). The sample is placed in the one of the delay path, imaged to a CCD plane by a long working objective lens. Another reference plane

wave is coherently overlapped on the CCD. By varying the optical delay, the CCD records image snapshots of the nanogap samples for each delay.

Applying sine function fitting for each pixels of the recorded CCD images, I assigned optical phase for each pixel and constructed optical phase map for the nanogap samples (figure 3.12). As one can see, distinct phase difference between gap and metal film exist on the measured phase map. Additional far-field diffraction pattern by the gap is mixed with the metal fields. I tried to exclude these unwanted speckles (i.e., diffraction pattern of gaps on the metal) to be averaged out, as shown in figure 3.12 (c). I divided the image along with each single gap element by setting region of interest in each delay snapshots, and acquired averaged phase of the gap and metal. Final phase of a sample was extracted by averaging the whole region of interest on the single snapshot. Figure 3.12 (d) demonstrates an example of averaged phase signal of the gap and metal, as a function of optical delay. From each sinusoidal oscillation signal, the phase difference is acquired, and I repeated this process for various gap sizes (figure 3.12 (e)). Lastly, I used equation 3.13 to estimate the field enhancement, as shown in figure 3.12 (f). The field enhancement reaches in order of 10 for 1 nm gap sample.

I compared the measured enhancement factor with calculated values, using numerical method presented in previous section. Here I fixed the wavelength as 800 nm, and varied the metal thickness and gap size. Figure 3.13 shows the calculated field enhancement, overlapped with the measured data of figure 3.12 (f). As one can see, the variation of field enhancement of nanogaps depending on a gap size and metal thickness is quite abrupt: a characteristic of the waveguide mode propagating through the metal-insulator-metal structure: so called gap plasmon [15]. The spectral property of the waveguide mode, extremely sensitive depending on the details of the gap structure. Structure details of a realistic sample directly affects to the optical measurement, which accompanies non-perfect profile of gap size or metal thickness as a function of illuminating positions, possibly caused by the nanometer scale grain formation during metal deposition [52] or any defects introduced during a fabrication process. Taking all information contained in the macroscopic beam size which is extremely large compared to the non-uniformity scale of the sample, the measured enhancement factors are therefore settled down to the gap size average of the calculated values.

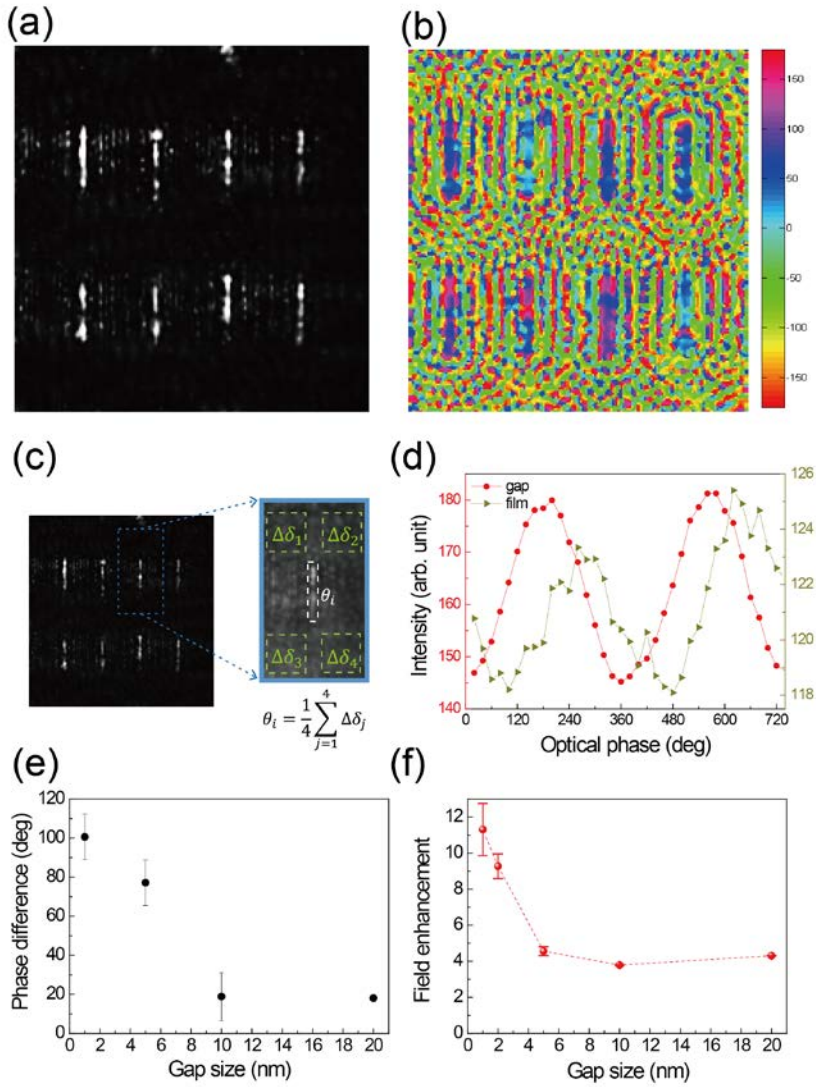

Figure 3.12 (a) CCD image of 25 × 25 μm ring-patterned 1 nm gap sample under polarized laser field illumination. Note that only the side lines of the square ring of nanogaps are seen due to the laser polarization. (b) Optical phase map of the sample (a). Phase angle in color bar is expressed in degree. (c) Optical CCD image under laser illumination. Extracting phase information from the measured interferogram by dividing slit region and metal region, then I averaged out the diffraction pattern by areal averaging. (d) Interferogram signal as a function of delay for a nanogap and metal region. (e) Extracted phase information for various nanogap sizes. Error bars indicate standard deviation for the averaging process. (f) Estimated field enhancement factor of nanogaps.

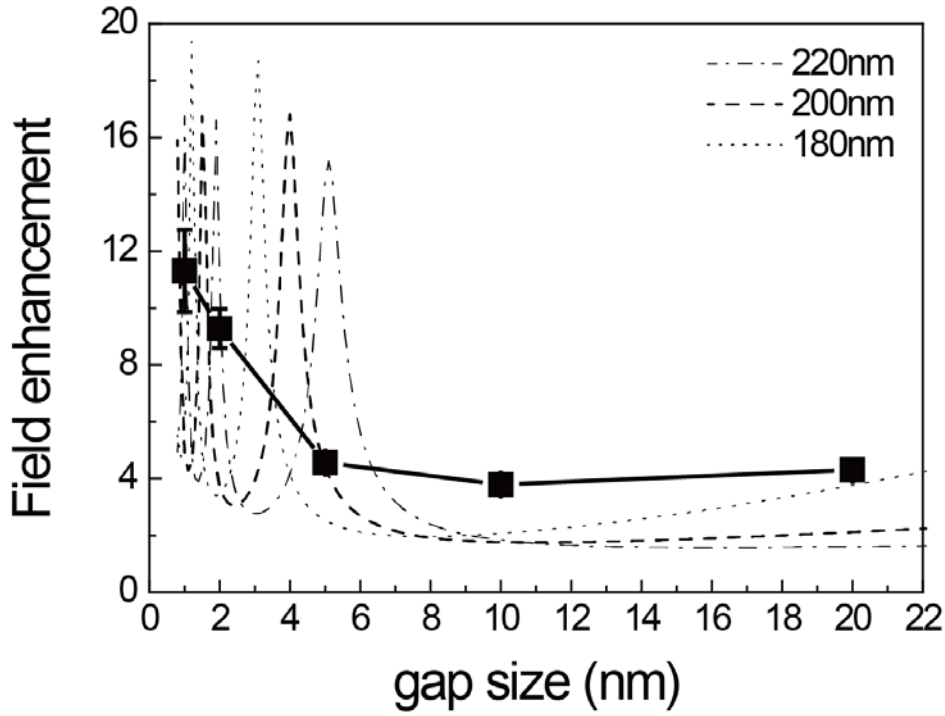

Figure 3.13 Calculated field enhancement factor as a function of gap sizes and metal thickness, compared with the experimentally estimated field enhancement.

3.4 Resonantly enhanced photoluminescence of metal

It is well known that the metal can support photoluminescence (PL) by the electron-hole recombination under strong optical field excitation [53], and it can be further enhanced by the optical field enhancement in plasmonic nanostructures [2, 3]. In this section, I demonstrated that the nanogap samples composed of metal also emit photoluminescence and it is enhanced by the gap waveguide mode (or gap plasmon enhanced).

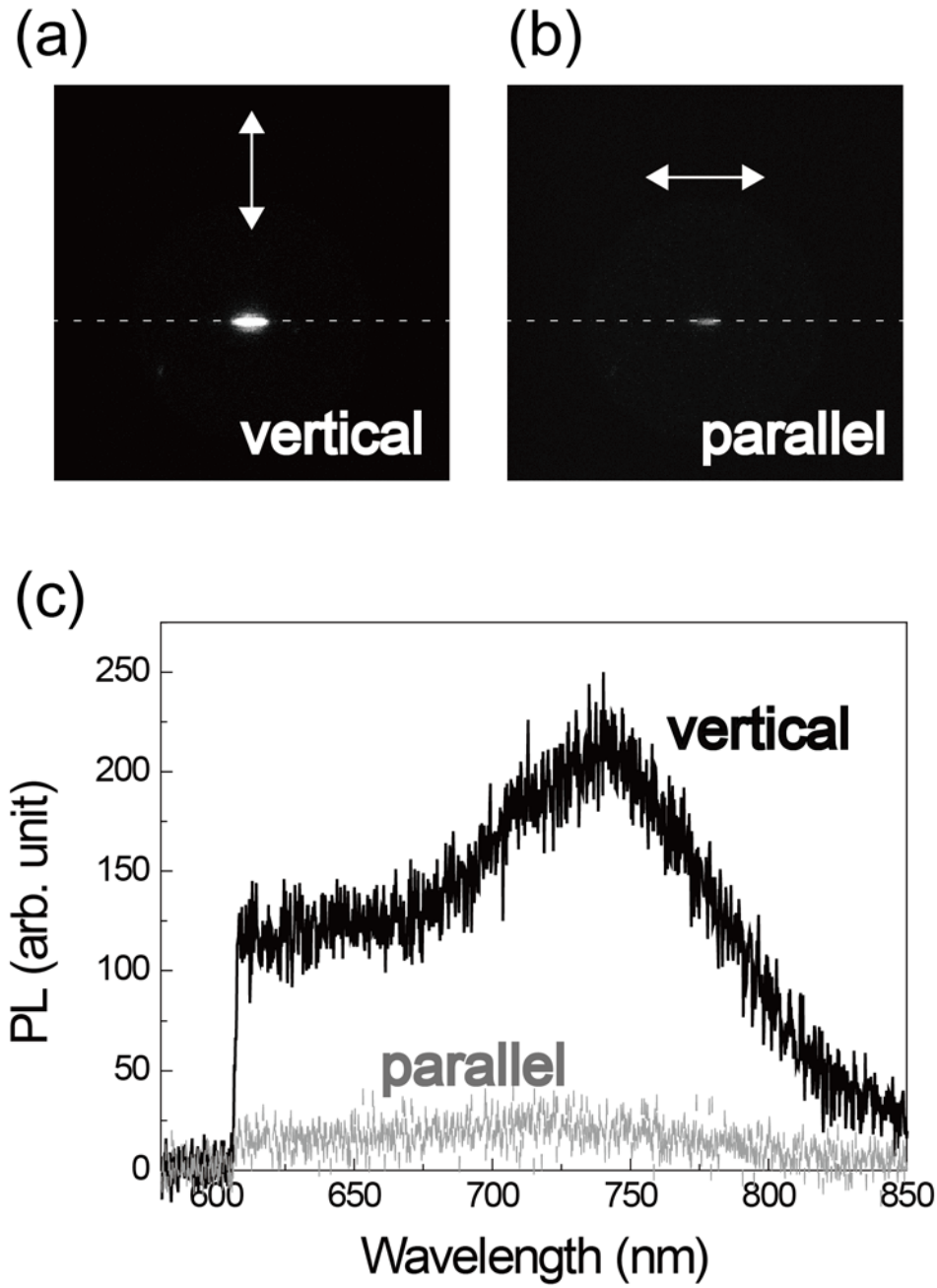

Figure 3.14 CCD images of PL signals from nanogap, under (a) vertical and (b) parallel polarization exciatation with respect to the nanogap direction. Arrows indicate incident polarization of excitation beam and dashed line is a guide for the eye. (c) Measured spectra for each polarization.

Nanogap samples are prepared in 200-nm-thick Ag film with gap size

of 5 nm. Continuous wave light source of 532 nm is focused on the nanogap with a diffraction limited spot, and the reflected (or transmitted) PL signal is measured by a spectrometer equipped with liquid-nitrogen cooled CCD and imaged by electron multiplying CCD (EMCCD, Andor), with suitable color filters to block the 532 nm light.

First I illuminated the laser to the nanogap with vertical polarization with respect to the nanogap (figure 3.14 (a)), and compared the PL intensity with parallel polarization (figure 3.14 (b)). Figure 3.14 (c) shows the results of polarization dependent spectra, showing that only for the vertical polarization emits strong light. The measured spectrum has peak near 750 nm, which is not related to any transition peaks of Ag [54].

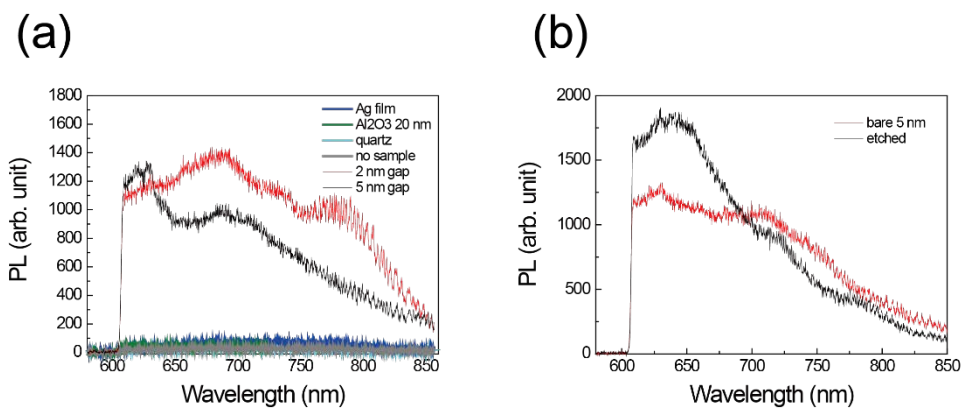

Figure 3.15 (a) Measured PL signal under various conditions with the same excitation power of 10 mW. (b) PL signal of 5 nm gap before and after the etching of gap material.

To check whether the signal is coming from the Ag or the other sources such as Al_2O_3 (gap material), I checked the PL signal from bare Ag film, bare quartz substrate and Al_2O_3 layer without metal structure with the measured nanogap signal. Also, to exclude the possibility of gap material where the field is enhanced, I etched out Al_2O_3 by immersing the nanogap sample in KOH solution for a few minutes and compared PL signals, before and after the treatment. By comparing all the PL signals mentioned above conditions without nanogap (figure 3.15 (a)), almost noisy signals are collected from quartz (same with the noise level) and minute signals from bare Ag film and Al_2O_3 were measured. Figure 3.15 (b) shows the PL

intensity of nanogap with gap material compared with absence of gap material, showing that almost similar signal level were collected, except the peak position is shifted.

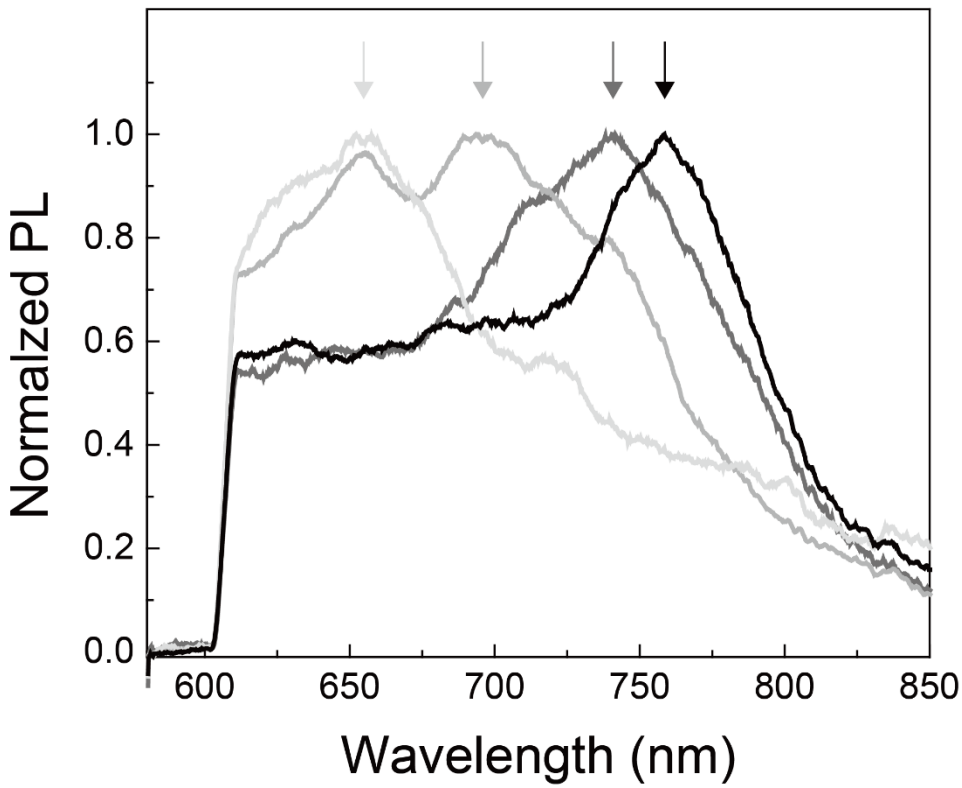

Figure 3.16 Normalized PL signal for various gap positions on the same sample. All data are smoothed (nearest-neighbor averaging, without reducing the spectral resolution of the spectrometer) to clearly show the resonance positions. Colored arrows are guide for the eye, denoting the spectral peak positions.

Next, I plotted the measured PLs by varying positions of the excitation beam spot along the nanogap (figure 3.16). Depending on the illuminating position, the peak position of PL changed with maintaining its overall intensity levels. Therefore, the PLs would be coming from the Ag nanogaps, enhanced by Fabry-Pérot resonance in a similar manner in optical transmission results of the previous section. Under the incoming 532 nm laser on metallic nanogaps, PL is generated from the Ag, then the generated PL is cavity-enhanced inside the nanogap, showing resonant behaviors. Since the

gap resonance is affected very sensitively by gap structure details such as gap size or cavity length, slight non-uniform profile along the nanogap makes considerable effect on single nanogap measurement, as shown in figure 3.16.

3.5 Conclusion

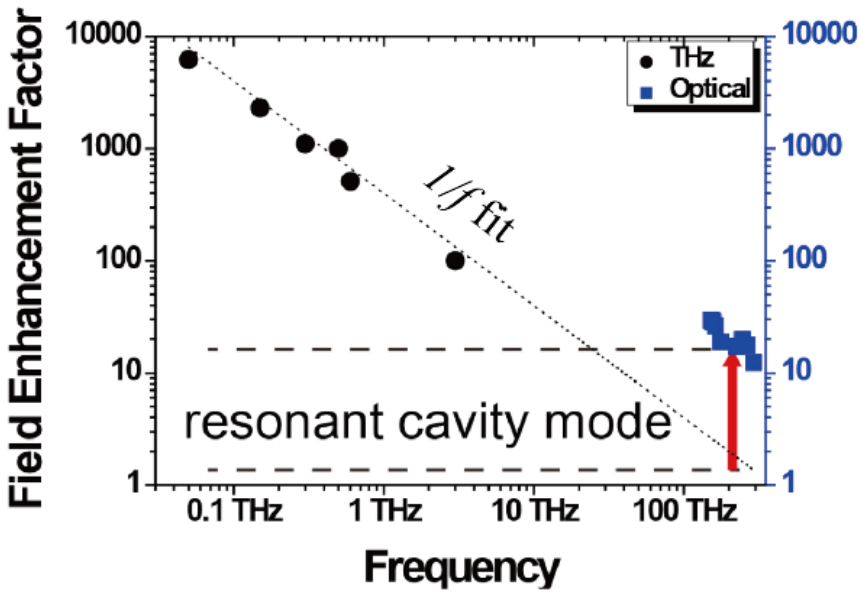

Figure 3.17 Field enhancement factor of 1 nm gap with 200 nm thickness Au samples, in frequency range from THz to visible. Dotted line is 1/*f* fitting of field enhancement, indicating capacitive charging of a nanogap. Because of the resonant cavity mode of our nanogap samples at optical – near-infrared frequencies, the field enhancement factor is 10 times larger than that is anticipated from the 1/*f* line. THz data were imported from the reference [13].

In conclusion, I measured and quantified field enhancement of nanogaps from visible to near-infrared wavelengths. For optically-thick nanogap samples, spectroscopic analysis based on the Kirchhoff integral formalism gives simple and accurate method for estimation of field

enhancement of nanogaps. The resulting field enhancement of Ag nanogap sample reaches ~ 40 for 1.5 nm gap at resonant wavelength of 2.2 μm. The frequency behavior of enhancement factors shows resonant property caused by the metal-insulater-metal waveguide mode, and this provides the tunability of field enhancement by controlling gap sizes and metal thicknesses. If the direct transmission through a metallic film is comparable to the nanogap sample transmission, such as Au film in a visible frequency, the background signal can be subtracted from the measured transmission with the phase information between metal field and gap field.

Overall field enhancement factor of 1 nm gap in optical – near-infrared frequency range was estimated by an order of ~ 10. To put the moderate optical field enhancement of nanogaps into perspective, I compared the optical enhancement factors of 1 nm gap with terahertz frequency regime (figure 3.17) [13]. Order of 10^3-10^4 enhancement factors in the terahertz frequencies are coming from the capacitive charging of the nanogap by a magnetic field induced eddy current, which inevitably lead to the $1/f$ dependence. However, at optical frequency regime, the field enhancement is larger, by one order of magnitude, than expected from the capacitive charging model. I believe that this strong enhancement mainly comes from the Fabry-Pérot resonance effect of nanogaps in optical frequencies, which increases field enhancement additional to the capacitive charging.

Chapter 4. Optical tunneling in nanogaps

Manipulating tunneling electrons by electromagnetic waves is a powerful tool for ultrafast science [19, 55, 56] and wireless energy conversion [57-59]. Temporal behavior of electronic wave function under the rapidly oscillating optical fields is extremely sensitive to the actual waveform of driving sources. Time-dependent optical bias strongly distorts the effective potential barrier, thereby subsequent ultrafast electronic transport occurs across the classically forbidden region. Under the high-frequency electromagnetic fields, harnessing tunneling electrons into experimentally accessible direct current (DC) is a critical step toward ultrafast optoelectronics in THz regime. Recent studies demonstrated precise control of rectified tunneling electrons in sharp nanotips or metallic nanostructures by illuminating terahertz (THz) [18, 19], near infrared [60] or visible waves [61, 62]. Subwavelength gap structures are used to confine incident waves for strong field enhancement across the one-dimensional barrier [11, 12, 16, 18], prerequisite for the efficient tunneling process which is highly nonlinear [63].

The motion of tunneling electrons through the barrier follows the potential gradient established by external controls such as light excitation or applying electronics [64]. In terms of rectification, this type of response is not very efficient since the oscillating source is generally sinusoidal in time, which results in vanishing current when integrated over harmonic cycles. Suitable asymmetry is thus required for the rectification of the oscillating waves, generally fulfilled by tailoring time traces of incident pulses [18, 55, 60, 61], adopting conducting electrodes as different work-functions/geometries [58, 59] or additional DC biasing across the barriers.

Here, I demonstrate direct manipulation of tunneling currents under external THz field and optical field, incorporating geometric shape on the tunneling barriers, adjoining them in a two dimension, forming a closed ring of vertically aligned metallic nanogaps [10]. The finite THz tunneling current emerges as a consequence of the contour integration. Ultrafast optical control of THz tunneling current is experimentally visualized by the additional optical pulse.

4.1 THz field and THz time domain spectroscopy

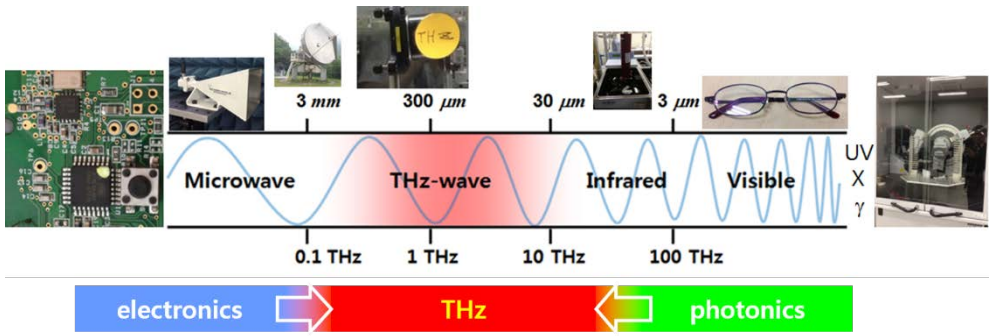

Figure 4.1 Various applications of electromagnetic waves on its frequency range. THz lies between microwaves and infrared.

THz wave is an electromagnetic radiation consists of 0.1 to 10 THz frequency range, 3 to 0.03 mm in wavelengths scale. It sometimes known as submillimeter waves, which lies between microwaves and infrared waves (figure 4.1). Many interesting physical phenomena are involved in this frequency regime, such as collective lattice vibrations, spin [65-70], electronic responses of semiconductor [71-74], superconducting gap [75] and intermolecular vibration/rotation [76-80]. However, technical difficulties related to the generation, detection and control of THz radiation still exist compared with the modern electronics and optics. THz range serves as a bridge connecting conventional electronics and photonics, and many efforts have been dedicated to bridge the gap.

Recently, high power THz generation technique have been developed, enabling new studies on strong light-matter interactions in the THz range. Since the proposal of tilted-pump-pulse-front scheme for efficient phase-matched THz pulse generation using lithium niobate ($LiNbO_3$) crystal [81], this technique has demonstrated the possibility of THz pulse with energies on the scale of 10 μJ [82, 83].

Meanwhile, noble metals such as Au and Ag behave as perfect conductor in this frequency regime. It has benefit to confine THz wave in a metallic nanogap, leading to a huge field enhancement [1]. As I showed in previous chapter, THz field enhancement of nanogaps is generally order of

10^3 – 10^4 (figure 3.13). Thus it provides a research platform for extreme phenomena such as quantum tunneling phenomena and nonlinear optics under the high power THz pulse.

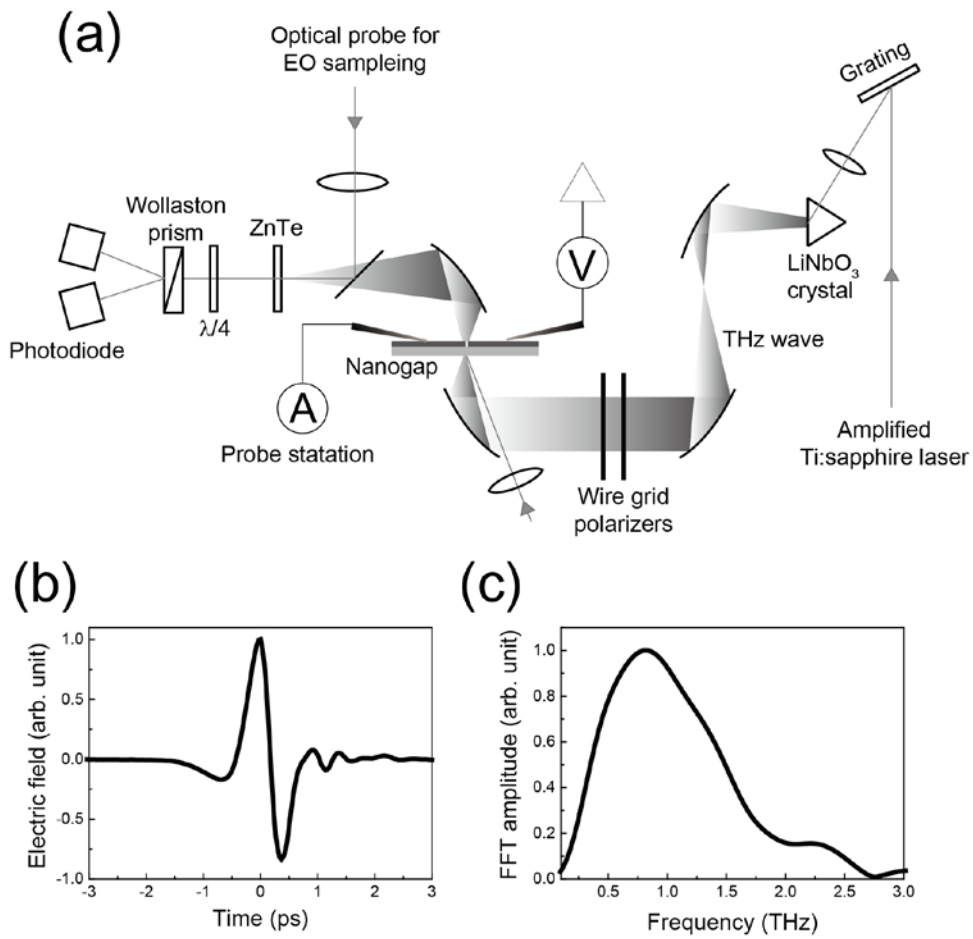

Figure 4.2 (a) High power THz-TDS setup with current measurement units. (b) Time trace of incident electric field and (c) its FFT amplitude.

In this work, transmission-type THz time domain spectroscopy (THz-TDS) was used to measure the transmission and THz tunneling current, which exploits high power THz radiation source generated from tilted-pump-pulse-front optical rectification in a $LiNbO_3$ crystal (figure 4.2) [84]. I used amplified Ti:Sapphire laser (800 nm) with low repetition rate (1 kHz) and 35 fs pulse-width for THz generation and optical probe. THz beam was guided by off-axis parabolic mirrors and focused to a 1 mm spot size, thereby peak field strength of 400 kV/cm was achieved. A pair of wire grid polarizers were

used to vary the incident field strength. For the polarization resolved measurements instead, I used a single polarizer to vary the incident polarization. To detect the THz field in time domain, 200-μm-thick ZeTe crystal was used for electro-optic sampling [85]. Subsequent quarter wave plate with a pair of photodiodes probe the temporal THz field.

4.2 Light as a high-frequency current source

Consider rectangular metallic electrodes separated by a gap of fixed size. Each electrode is connected to a voltage source or a current source (figure 4.3). One of the gap is placed parallel to the side of the rectangle, and the other is tilted, as described in figure. And I want to know final voltages applied to the gap for two different types of driving sources and gap geometries. For the voltage source case (figure 4.3 (a)), final voltage is independent of the gap geometry. Induced charges across the gap make the gap voltage determined by the applied voltage. However, for the current source case (figure 4.3 (b)), the current flux driven by the current source projected to the gap and charges the gaps depending on the gap geometries, as following

$$V_{\text{gap}}(t) \propto \int_{-\infty}^{t} dt' [\mathbf{n} \cdot \mathbf{K}_{\text{inc}}(t')] \tag{4.1}$$

Final voltage applied on the gap is now very sensitive to the geometry of the gap, determined by the vector relation $\mathbf{n} \cdot \mathbf{K}$.

When the electromagnetic waves impinge normal to the perfect conductor film (figure 4.4 (a)), the Maxwell boundary conditions determine the field strength on the surface: vanishing electric field and doubling magnetic field. The incident magnetic field $\mathbf{H}_{\text{inc}}$ induces an eddy current $\mathbf{K} = \mathbf{n} \times (2\mathbf{H}_{\text{inc}})$ on the film, which reflects back the incident light and blocks field smearing into the perfect conductor. Noble metals such as gold or silver are good metal in well below the plasma frequency of the metal [1, 86], thus the induced current near the metal surface still follows the above picture; the current density can be approximated by $\mathbf{K} \sim \mathbf{n} \times (2\mathbf{H}_{\text{inc}})$, now flowing through

deep inside the metal film. In the presence of a slit punctured through the metal film, or a slot whose resonance frequency is much smaller than the incident driving frequency, the time-dependent driving surface current will accumulate charges across the gap in a vectorial way (figure 4.3 (b)). Field enhancement in the gap would be proportional to the charging time, in similar to the capacitor (figure 4.4 (b) and (c)).

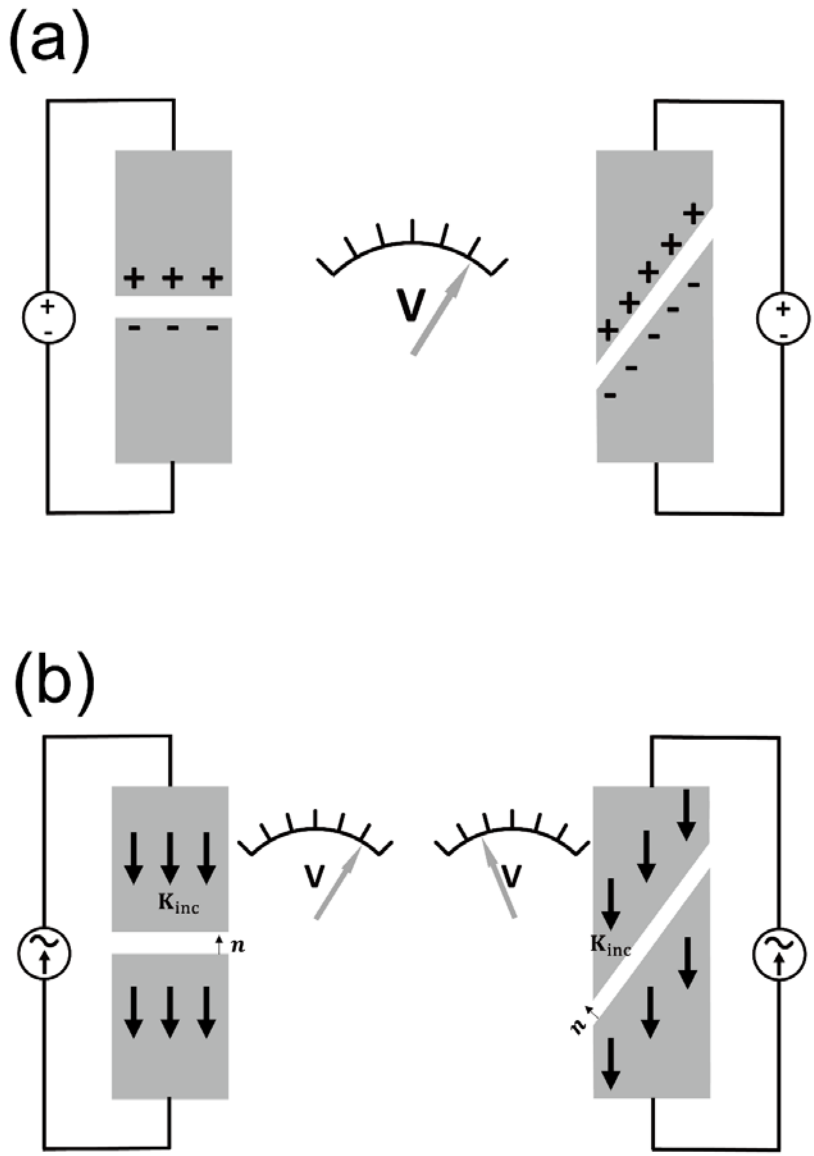

Figure 4.3 Geometry dependent charging dynamics of metallic electrodes, driven by (a) a voltage source and (b) a current source.

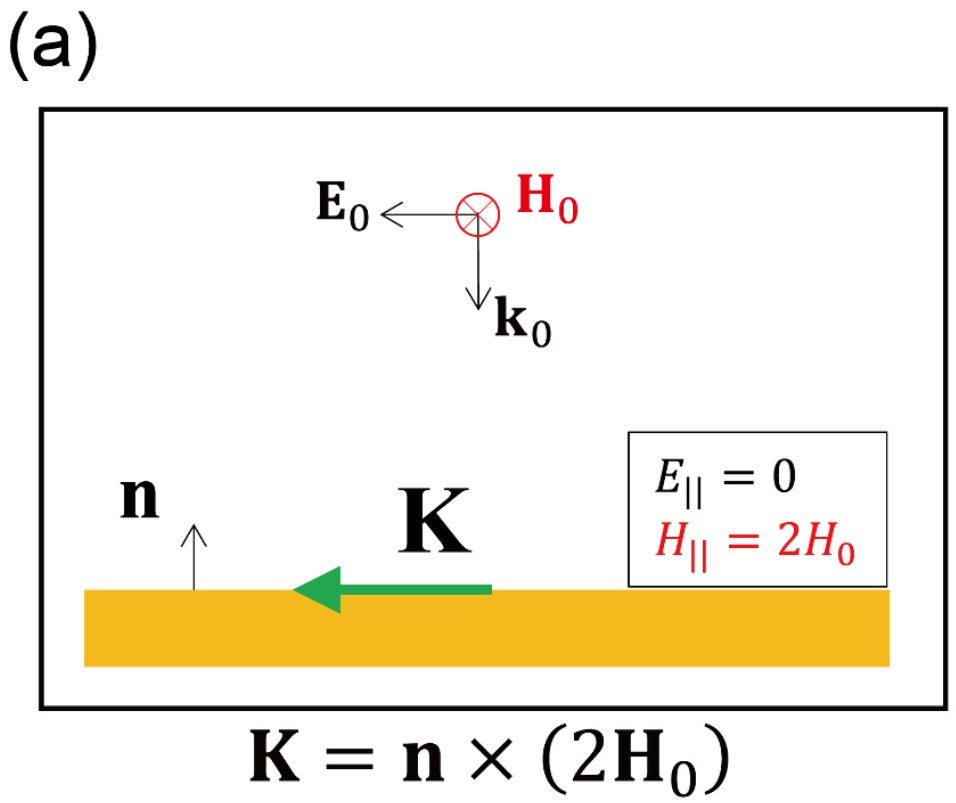

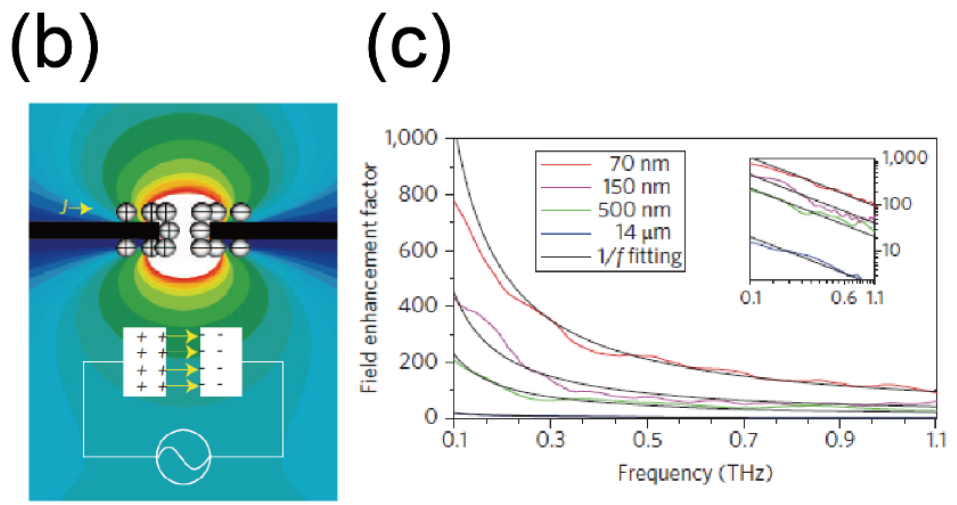

Figure 4.4 (a) Description of light driven surface current on a perfect conductor determined by the Maxwell boundary conditions. (b) A nanogap as a capacitor charged by incident electromagnetic waves and (c) resultant field enhancement as a function of frequency showing 1/*f* behavior [1].

4.3 THz tunneling in a triangular barrier

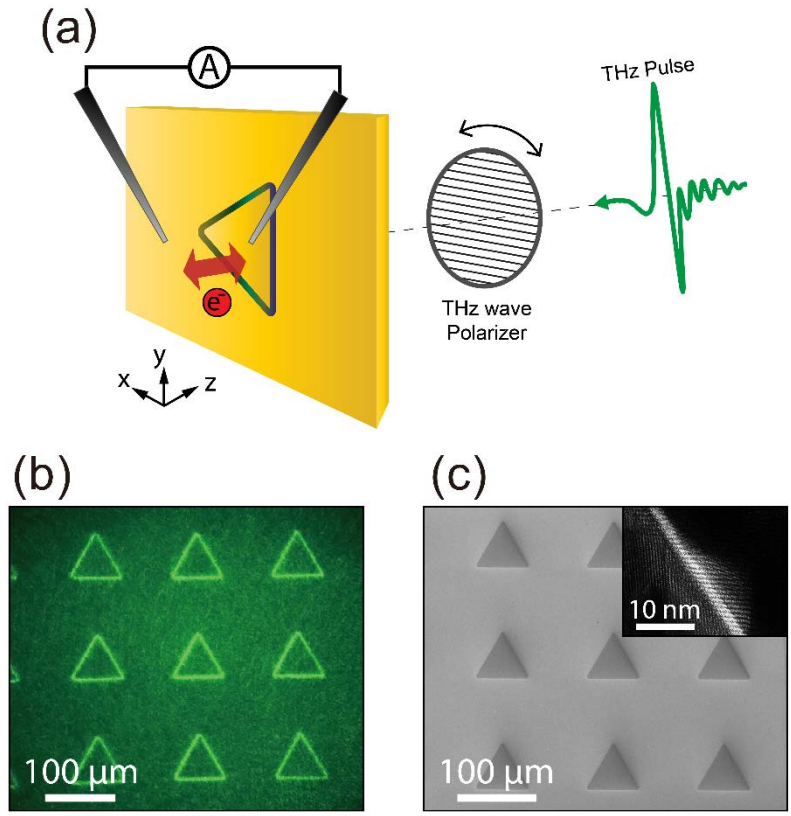

Figure 4.5 (a) Schematic for tunneling current measurement under single-cycled THz pulse illumination (b) Optical scattering image and (c) SEM image of triangle nanogaps. Here the pattern size is 70 μm and period is 140 μm. Inset: cross-sectional TEM image of 2 nm gap.

Experimental scheme of tunneling currents measurement under electromagnetic pulse excitation is described in figure 4.5 (a). Single-cycled THz pulse incident on the ring-shaped nanogaps fabricated in a 100-nm-thick Au film, on a 500-μm-thick quartz substrate (figure 4.5 (b) and (c)). The metallic island is completely isolated from the surrounding metal film by a vertically aligned insulating layer (Al_2O_3), forming a closed tunnel barriers in a two dimension. Tunneling currents through the barriers are directly probed by two metallic tips (MS TECH). To safely attach a metallic probe inside the

pattern without damaging the sample surface, one of the tip I used was an electrochemically etched tungsten wire, with the tip radius of ~ 1 μm. One probe is connected to a Keithley 2450 sourcemeter to apply a DC bias and the other probe is connected to a current preamplifier (SR570) and a lock-in amplifier (SR830) synchronized to the laser repetition rate (1 kHz). Both tips are positioned on the opposite side to the illuminating direction to avoid blocking the incident beam. All electrical apparatuses were on the same ground. Figure 4.6 (b) demonstrate the oscilloscope signal of the current preamplifier under THz pulse illumination of the nanogap, showing the burst of tunneling current along with the laser repetition rate (1 kHz). The broadness of each burst coming from the current amplifier bandwidth (details are explained later).

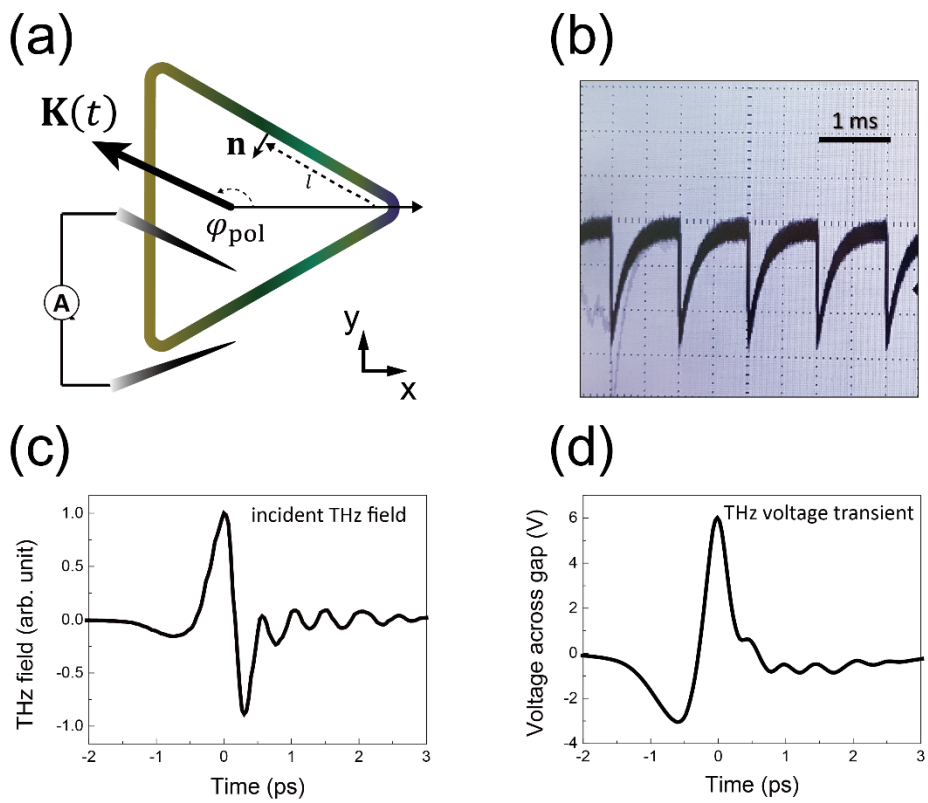

Figure 4.6 (a) Surface current **K** charges the triangular nanogap. (b) Oscilloscope screen showing current pulse generated under THz pulse illumination. (c) Time trace of incident THz field and (d) expected induced voltage across gap trace under capacitive charging.

A THz pulse incident on the metallic film induces Eddy currents described by surface current density $\mathbf{K} \sim \mathbf{n} \times (2\mathbf{H}_{\mathrm{inc}})$, thereby capacitive-charging the ring nanogap as a following way (figure 4.6 (a)),

$$V(l,t) \propto \int_{-\infty}^{t} dt' [\mathbf{n}(l) \cdot \mathbf{K}_{\mathrm{inc}}(l,t')] \tag{4.2}$$

where $V(l,t)$ is the time-dependent barrier potential at arc length l at time t and **n** denotes unit vector perpendicular to the ring, directed inward from the barrier. Figure 4.6 (c) and (d) show the time profile **K** and $V(t)$, respectively. The temporal shape of **K** is directly given by the incident THz field profile, and $V(t)$ is the time integration of **K**, which is given by equation 4.2.

As the gap size decreases down to nanometer scale, the induced electric field in the gap is further enhanced by the induced charges of the opposite sides of the gap pulling each other, making enough potential gradient to drive non-negligible tunneling current across the point junctions. Temporal response of the resulting current is straightforwardly determined by the time profile of the incoming electromagnetic field. However, if the tunnel junctions are adjoined together forming a closed-ring, the resulting total current flowing through the ring, $I(t)$, would be a sum over all the point junctions, expressed by the following contour integration,

$$I(t) = h \oint dl\, J(l,t) \tag{4.3}$$

where J is the tunneling current current density determined by the electric potential and h is the metal thickness. Depending on the incident polarization, the vector relation (integrand of equation 4.2) determines the electric potential which drives a local tunneling current. The contour integration is naturally affected by the symmetry of the ring. Therefore, the response of the integrated junctions under the rapidly oscillating field is fundamentally different from the response on each junction element, which introduces an entirely new degree of freedom for manipulating the tunneling current.

For detailed description of tunneling current depend on the geometrical symmetry as a function of incident polarization, figure 4.7 illustrates the potential and current distribution of the contours, an equilateral triangle and a square. The presence of inversion symmetry on the geometry, such as square, results in vanishing current since the potential at any point on

the contour are counterbalanced by its corresponding point across the center independent of the incident polarization. However, the strong nonlinearity of tunneling process and lack of inversion symmetry of the triangle together with the asymmetric THz pulse profile makes the nonzero total current under the THz field illumination.

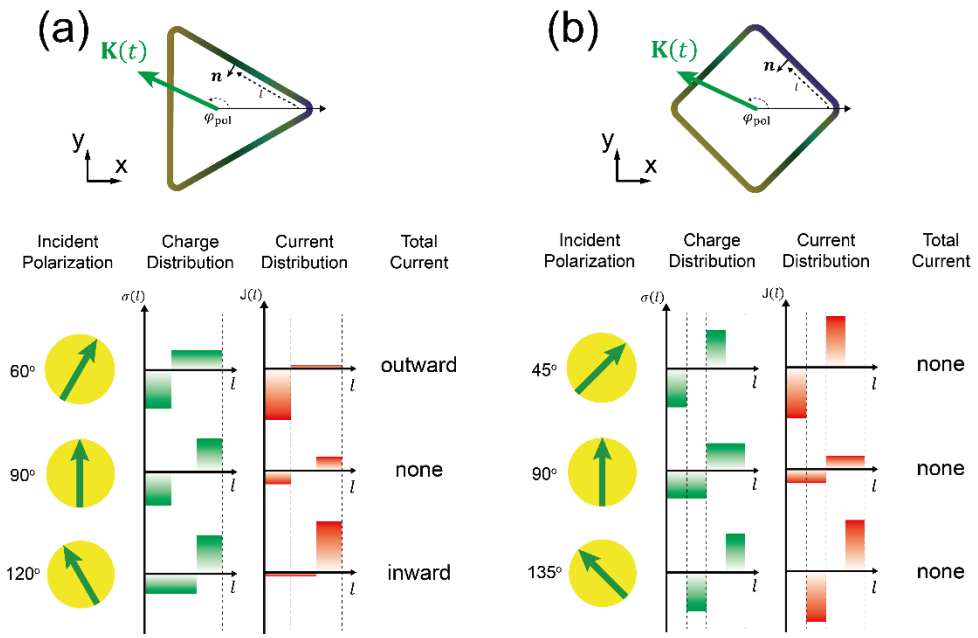

Figure 4.7 Potential distribution and subsequent total tunneling current through the ring barrier as a function of incident polarization in (a) an equilateral triangle and (b) a square.

4.3.1 Theoretical method

In this study, I exploited full integral expression of the Simmons formula [64, 87], derived from the 1-dimesnsional tunneling problem with WKB approximation. Tunneling current density J can be expressed by (figure 4.8),

$$J = \frac{4\pi me}{h^3}\left[\int_0^{\eta} D(E)(\eta - E)dE - \int_0^{\eta - eV} D(E)(\eta - V - E)dE\right] \quad (4.4)$$

where m is the electron mass, e the electron charge, h the Planck constant, η the Fermi energy of metal, V the applied voltage across the barrier, E the tunneling electron energy and D is the electron tunneling probability factor

based on the WKB approximation

$$D(E) = \exp\left(-\frac{4\pi\Delta s\sqrt{2m}}{h}\sqrt{\eta + \overline{\varphi} - E}\right) \tag{4.5}$$

and the mean barrier height

$$\bar{\varphi} = \frac{1}{\Delta s}\int_{s_1}^{s_2}\left(\varphi_0 - \frac{eVx}{s} - \frac{1.15\lambda s^2}{x(s-x)}\right) \tag{4.6}$$

where φ_0 is the rectangular barrier potential height, s the thickness of the insulating layer, $\lambda = e^2\ln 2/16\pi\epsilon s$, ϵ the dielectric function of insulating material, and $\Delta s = s_2 - s_1$ is the effective barrier width where the limits s_1 and s_2 are given by the real roots of the cubic equation,

$$\varphi(x) = \varphi_0 - \frac{eVx}{s} - \frac{1.15\lambda s}{x(s-x)} = 0 \tag{4.7}$$

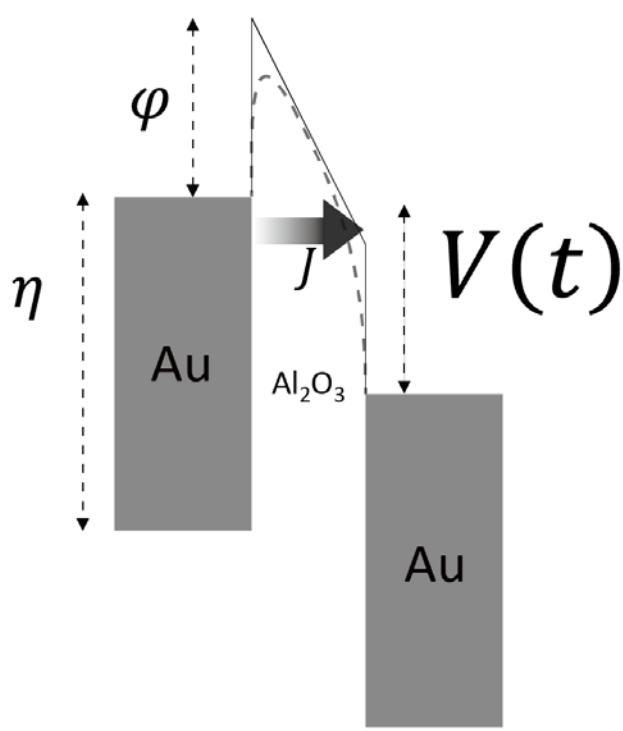

Figure 4.8 Schematic of 1-dimesional tunneling through Al_2O_3 barrier under applied time-dependent bias.

4.3.2 Tunneling current measurement

To check the validity of fabricated ring-shaped tunneling barrier, I performed current-voltage (IV) measurement under the steady-state (applying DC voltage) and instantaneous (applying THz pulses) cases. Figure 4.9 (a) shows a DC IV measurement of the triangle nanogap, showing general exponential tunneling behavior. From the curve fitting process based on the Simmons formula, I extract the barrier potential of Al_2O_3 layer used in our experiment (~2.2 eV) and layer thickness (~ 2 nm) which is also estimated in TEM analysis (inset of figure 4.5 (c)). To combine the measured DC IV data with the subsequent THz measurements tied to the same fitting curve, I considered a current flowing through only one side of the triangle. Thus I divided the DC current by a factor of 3; assuming equivalently distributed DC currents to the 3 sides of the triangle.

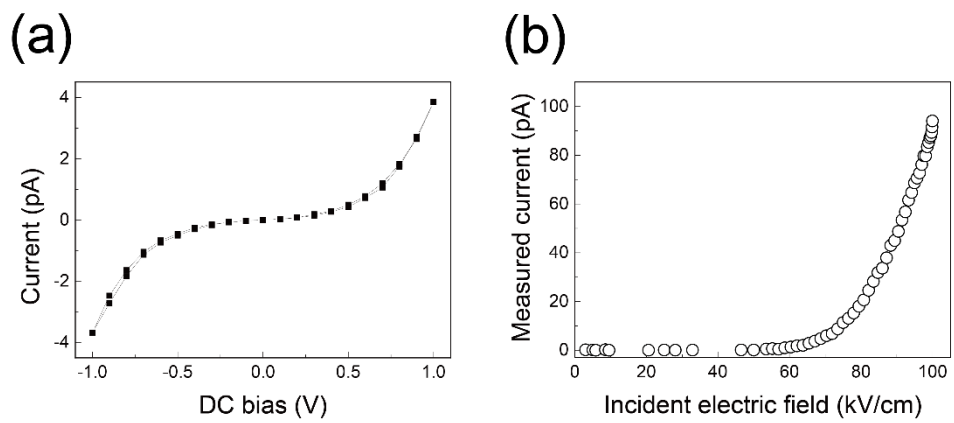

Figure 4.9 Measured tunneling current of a triangle barrier (side length of 70 μm, gap size of 2 nm) under (a) a DC bias and (b) THz field illumination.

Figure 4.9 (b) shows the measured current by illuminating THz pulse to triangle nanogaps as a function of incident field strength. A pair of wire-grid polarizers was used to vary the THz electric field. Onset of THz current under incident field strength of 50 kV/cm was shown.

The resultant voltage applied across the gap by THz field is estimated by using the Kirchhoff integral formalism [1, 29]. Power dependent THz TDS measurement (figure 4.10) shows triangle nanogap transmission about $t \sim 3\times10^{-3}$. For the transmission data, the Au direct transmission was subtracted

in time-domain, since the direct transmission signal was at a non-negligible level (~ 0.002) compared to the nanogap sample transmission. Coverage ratio of our sample (β~1.07×10^{-5}) together with the measured transmission gives field enhancement factor (t/β) of ~300. With the measured field enhancement factor, the resulting gap field was estimated by $E_{gap} = E_{inc}$·(field enhancement), where E_{inc} is the incident field strength. I finally estimated the E_{gap} to be ~ 3 V/nm.

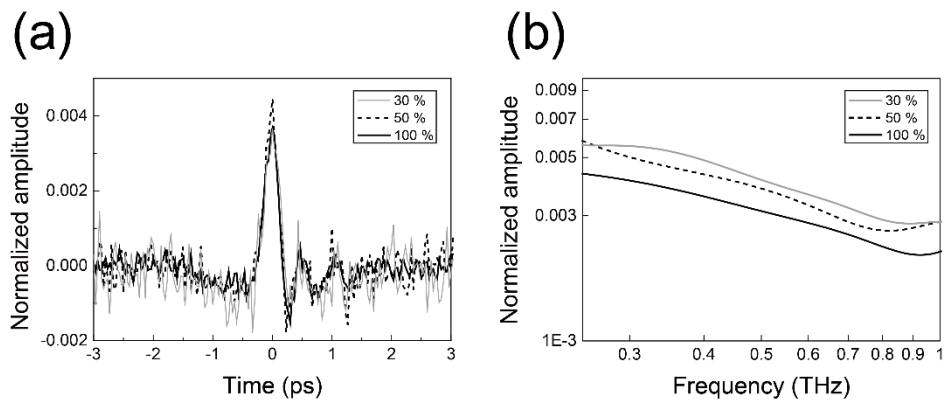

Figure 4.10 THz transmission of nanogaps (side length of 70 μm, each triangle pattern was separated by 140 μm) by changing incident field strength. (a) Time trace data and (b) its FFT amplitude as a function of incident field strength, normalized by incident field strength through quartz substrate. Here, maximum incident field was 400 kV/cm and the illuminated field strength is denoted as percentage.

Next, to convert the measured current amplitude to the instantaneous peak current amplitude, I considered the geometrical field distribution (figure 4.7 (a)). I multiplied a factor of $J(E)/(J(E) - J(E/2))$ to the THz current to extract the current component flowing only through a single side. And tunneling current pulse half width of ~ 0.2 ps was considered (measured by optical method, details are presented in later section). The bandwidth of our current preamplifier is 2 kHz (with sensitivity of 10 nA/V) which is much lower than tunneling current pulse bandwidth (expected to be higher than 1 THz from the tunneling nonlinearity). In this case, the measured signal in the lock-in amplifier is proportional to q_t/τ_{rep}, where q_t is total tunneled charges for the one pulse,

$$q_{\mathrm{t}} = \int_0^{\tau_{\mathrm{rep}}} I(t)\, dt \tag{4.7}$$

and τ_{rep} is the pulse to pulse separation time (1 ms). Therefore, the instantaneous peak tunneling current can be estimated via the total tunneled charges q_{t} divided by the tunneling current pulse width. To find a quantitative relation between the output of the lock-in amplifier and the total tunneled charges, I modeled the time trace of the current preamplifier response $I_{\mathrm{amp}}(t)$ (figure 4.6 (b)) by a Fourier expansion

$$I_{\mathrm{amp}}(t) = \sum_p C_p \cos\left(2\pi p \frac{t}{\tau_{\mathrm{rep}}}\right) \tag{4.8}$$

where C_p is the Fourier coefficients with integer p. Thus C_1 is directly related to the lock-in amplifier output which is synchronized to the pulse repetition rate. Here, my purpose is to find a relation between $q_{\mathrm{t}} = I_0 w$ (undercurve area of $I_{\mathrm{amp}}(t)$) and C_1, where I_0 is the maximum of $I_{\mathrm{amp}}(t)$ and w is the current pulse width of $I_{\mathrm{amp}}(t)$. I assume that the curve shape is similar to the square wave. While the real curve shape of exponentially decaying is far from the assumption, the FFT results between square wave and exponential decaying wave almost similar when $w << \tau_{\mathrm{rep}}$. By multiplying $\cos(2\pi t/\tau_{\mathrm{rep}})$ and integrating in $[-\tau_{\mathrm{rep}}/2,\ \tau_{\mathrm{rep}}/2]$ for both sides of equation 4.8, C_1 can be expressed by

$$C_1 = \frac{2I_0}{\pi} \sin\left(\frac{\pi w}{\tau_{\mathrm{rep}}}\right) \tag{4.9}$$

This can be further reduced to $C_1 = 2I_0 w/\tau_{\mathrm{rep}}$ by assuming $w << \tau_{\mathrm{rep}}$ (while this assumption is not rigorously valid under the current preamplifier bandwidth presented hear, 2 kHz, I confirmed the same signal level for a larger bandwidth by decreasing the sensitivity of the preamplifier, e.g. 20 kHz case under a strong signal condition, thus justified the assumption). Considering the root mean square output of the lock-in amplifier ($C_1/\sqrt{2}$ = measured current), the total tunneled charges for a single pulse cycle can be written by

$$q_{\mathrm{t}} = (\text{measured current}) \times \tau_{\mathrm{rep}}/\sqrt{2} \tag{4.10}$$

From the measured total charges divided by the tunneling current pulse width, finally I estimate the temporal current of ~ 0.2 A for the THz voltage of ~ 6

V across the gap (figure 4.11).

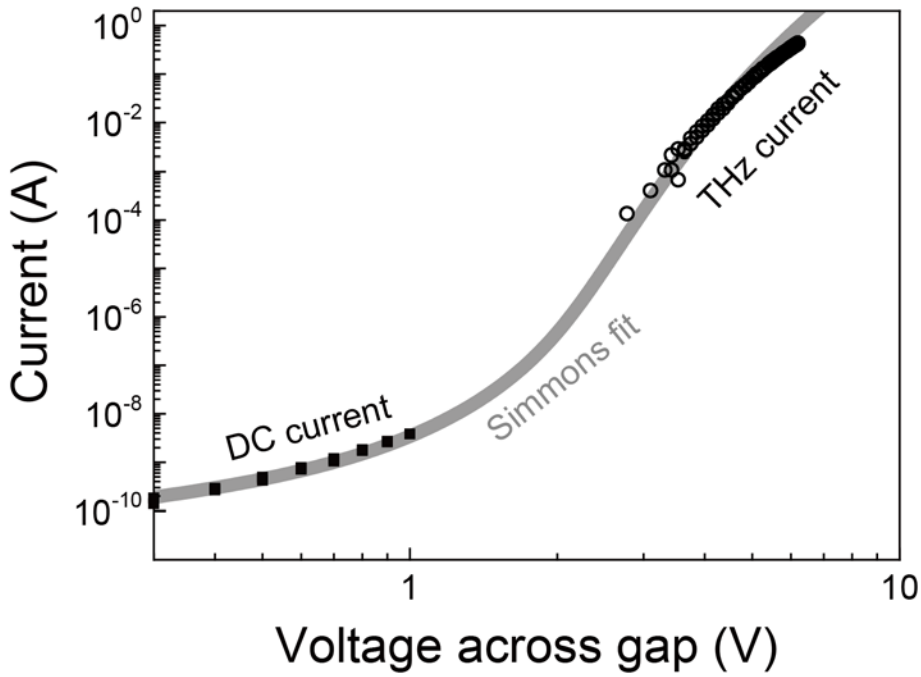

Figure 4.11 Combined experimental data of static DC measurement and transient THz current data with fitting line based on the Simmons formula.

4.3.3 Modeling triangle current

To analyze the total current of ring barriers as a function of THz polarization, a simple toy model was exploited (figure 4.12 (a)). Angle between an incident surface current and a side of the triangle determines the applied field strength on the barrier, and the total current I_{total}

$$I_{\text{total}} = \sum_i a_i \, J(E_{\text{inc}} \sin \theta_i) \tag{4.11}$$

where a_{i} is the asymmetry factor of each side of the geometry, $J(E)$ the tunneling current density as a function of the field strength E, E_{inc} the incident field strength and i runs through a number of the geometry's sides. Here, the asymmetry factor reflects the non-uniformity of realistic barriers in the sample. Figure 4.12 (b) shows the example of total current from an equilateral triangle under a rotation of incoming polarization and figure 4.12 (c) is a polar

plot of the current. Under an ideal equilateral triangle, the current shows three-fold rotational symmetry.

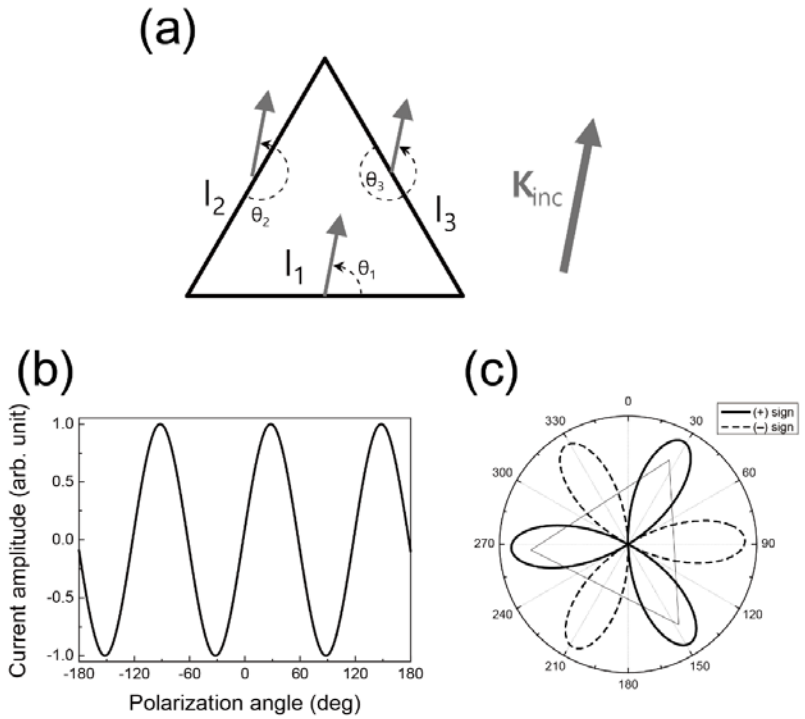

Figure 4.12 (a) Model diagram for total tunneling current through triangle barrier under surface current incident. (b) Calculated total current under polarization rotation and (c) its polar plot, showing three-fold rotational symmetry of a triangle. Black triangle line in (c) is a guide for eye.

Figure 4.13 (a) shows the measured tunneling currents by sweeping the THz polarizer for two different types of geometry, triangle (asymmetric) and square (symmetric) nanogap. As one can see, the measured current of triangle shows much higher current compared to the current from the square, showing the large impact on a current generation depend on the symmetry of the geometry. Next I applied equation 4.11 on this measured curve including the polarizer effect (Malus' law); field strength E_{inc} is also a function of polarizer angle $E_{\mathrm{inc}} = E_0\sin(\varphi_{\mathrm{pol}})$. Due to the slight non-uniformity for each side (figure 4.13 (d)), a_{i} ratio of 1, 0,75 and 0.67 were used for the fitting process. Using these parameters except for a constant value of E_{inc}, I described the polarization response of full 360 degrees, shown as black line

in figure 4.13 (b). Also, I used similar process for the square sample data in figure 4.13 (a), thus finally reconstructed the current, demonstrating polar plots of figure 4.13 (c). Presence of minute signals for the square is due to the non-perfect profile of Al_2O_3 layer along the contour (figure (4.13 (d)). Nevertheless, the large impact of geometrical property on the current measurement is clearly seen.

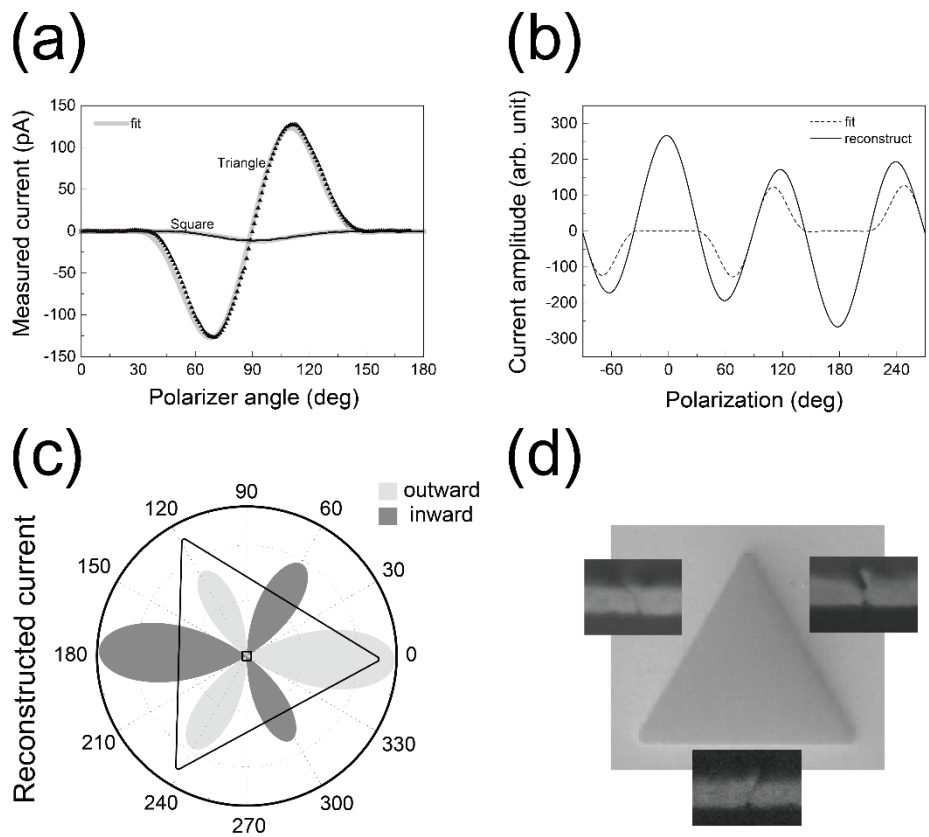

Figure 4.13 (a) Polarizer angle dependent tunneling current measured for a 70-μm-sized triangle and a 25-μm-sized square. Fitting line is based on modeling presented previously. (b) Reconstructing fitting line acquired in (a) (dashed line) by assuming the incident field maintain its field strength under the polarization rotation (black line) based on the previous toy model. (c) Polar plot of reconstructed curve acquired in (b) for triangle and square. Black lines are guide for the eye. (d) Cross-sectional SEM image for each triangle side, showing the non-perfectness of the barrier, resulting minute signal for the square and asymmetric triangle shape in (c).

4.3.4 THz tunneling current estimation from THz-TDS

Recently, J. Y. Kim *et. al*. reported on the estimation method of THz tunneling current from the analysis of the THz nonlinear transmission measured by THz-TDS [88]. Since the THz-TDS directly measures the time profile of the voltage applied on the gaps, it is possible to estimate the time-dependent tunneling current. Here, I tried the same method to extract the real-time tunneling current through the nanogaps from the THz-TDS.

In the absence of tunneling currents (not enough THz voltage applied on the gap), the transmitted signal measured by TDS is described directly by equation 4.1 (capacitive charging of the gap by the incident surface current, $\mathbf{K} = \mathbf{n} \times (2\mathbf{H}_{\mathrm{inc}})$) since the voltage applied on the gap (V_{gap}) is directly proportional to the measured signal (i.e, $V_{\mathrm{gap}}=E_{\mathrm{gap}}w$ and measured field profile is directly proportional to the E_{gap}, where E_{gap} is electric field across the gap and w is the gap size). However, if there exist tunneling currents across the gap, the transmitted field profile would be different from the estimated curve shape by equation 4.1. Therefore, the time-dependent tunneling current information can be inferred from the charge difference between accumulated by incident field and measured field as following

$$\int_{-\infty}^{t} \left(2H_{\mathrm{inc}}(t')\right) l \, dt' - CV_{\mathrm{TDS}}(t) = \int_{-\infty}^{t} I(t') \, dt' \qquad (4.12)$$

where l is the triangle side length, I is tunneling current across a gap, C is capacitance of a nanogap (which can be calculated as $C = \epsilon lh/w$, where w is the gap size, h the metal thickness and ϵ is the dielectric constant of gap materials) and V_{TDS} denotes the measured gap voltage profile. The 1st term of left hand side of equation 4.12 indicates the total charges accumulated by the incident field $\mathbf{K}$ (= $\mathbf{n} \times (2\mathbf{H}_{\mathrm{inc}})$) (incident Q of figure 4.14 (a)). The 2nd term denotes accumulated charges charged by the actual gap field which is measured by TDS (measured Q of figure 4.14 (b)), and the right hand side is the net tunneled charges (tunneled Q of figure 4.14 (c)). I used the peak field strength as E_{gap} ~ 3 V/nm (estimated from the transmission measurement), thus V_{TDS} profile can be determined by using this factor and measured transmission signal. Also, when the THz polarization is vertical to one of the side, $\varphi_{\mathrm{pol}} = 0^{\mathrm{o}}$, the total tunneling current through the triangle mostly flow through the left side (i.e., $J(E/2)/J(E)$ ~ 0, check figure 4.18 (b) in next

section), thus I can consider only the current flow through the left side of the triangle.

The TDS noise level overwhelms the current level (expected as an order of 0.1 A from my previous measurement) due to the extremely now signal transmitted through the nanogaps, thus it makes hard to analyze the tunneling current. Note that the above analysis is based on the pure slit structure; resonant property is not considered in this analysis, which would may introduce an additional inductive term in equation 4.12. Thus, the sinusoidal shape shown in figure 4.14 (b) seems to be an artifact which may come from the resonant component of my triangle (i.e., incident **K** is not described by $\mathbf{n} \times (2\mathbf{H}_{inc})$, details are presented in next section)

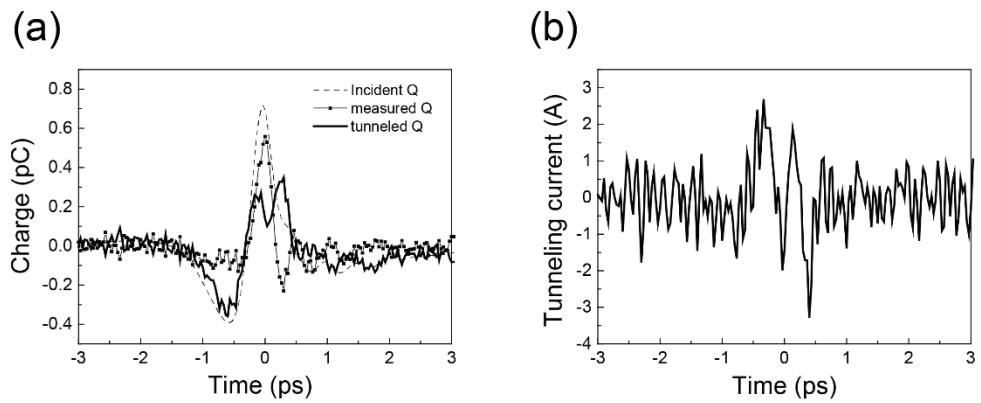

Figure 4.14 (a) Estimated time-dependent charge accumulation dynamics on the nanogap by THz-TDS. (b) Extracted tunneling current transient by differentiating the tunneled Q in (a).

4.3.5 Effect of resonant THz field excitation

Previously, I described the profile of surface current **K** as the same profile as the incoming THz pulse. This was possible because the resonance frequencies of the previous structures (< 0.2 THz) lie in far below the THz source frequency (peaked at ~ 0.9 THz, figure 4.2 (c)). The incident field polarization generate the surface current density which is successfully described by the $\mathbf{K} = \mathbf{n} \times (2\mathbf{H}_{inc})$ without any distortion at the metal surface; the triangle can be considered of three independent slits with infinite length compared to the incident wavelength. However, when the resonance

condition is fulfilled, the current relation between **K** and $\mathbf{H}_{inc}$ does not valid, since the field profile over the resonant antenna is affected by the antenna itself (by an induction current of the antenna).

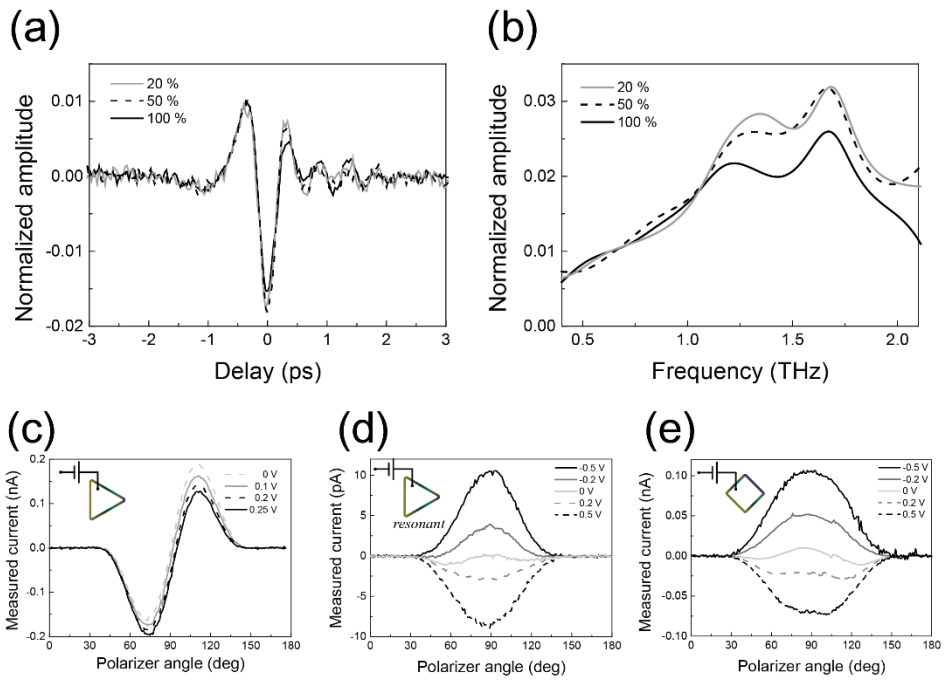

Figure 4.15 Normalized transmission of 10-μm-sized triangle in (a) time domain and (b) frequency domain, showing resonance near 1.3 THz. A subsidiary peak near 1.6 THz is coming from water absorption. (c) Tunneling current of (c) non-resonant (70-μm-sized), (d) resonant (10-um-sized) and (e) symmetric square barrier (25-μm-sized) under DC biasing.

Figure 4.15 (c), (d) and (e) demonstrate THz current responses as a function of polarizer angle and DC bias. For a 70-μm-sized triangle (figure 4.15 (c)), the measured current shows the sinusoidal shape which is expected by the previous modeling. Applying DC bias imposes potential gradient to the whole barrier, thus the current direction is biased in a particular direction. The 25-μm-sized square also shows the expected behavior by the counterbalanced potential distribution, and the DC bias breaks the symmetry; a finite current was generated. However, for the 10-μm-sized triangle (figure 4.15 (e)), which has a resonance around 1.3 THz (figure 4.15 (a) and (b)), shows totally different response compared with the previous triangle current;

rather it shows similar behavior with the symmetric square.

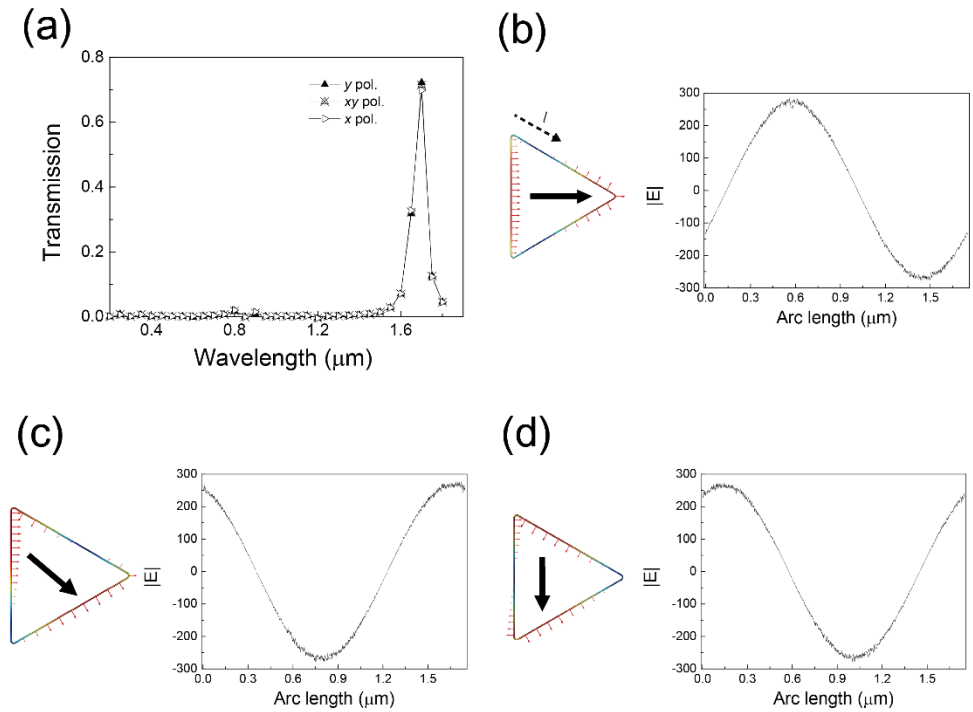

Figure 4.16 Numerical simulation result of 0.6-μm-sized triangle of 50 nm gap in a 50 nm thick PEC film by changing incident polarization. (a) Transmission spectra calculated, showing resonance in ~ 1.7 μm. Polarization dependent field distribution in resonance wavelength for (b) *x* polarized, (c) *xy* polarized and (d) *y* polarized case at the resonant wavelength.

To check the field distribution of resonant triangles, I performed numerical simulation of electric field profile using commercial software (COMSOL). Figure 4.16 demonstrate the simulation results of electric field distribution and transmission for a resonant triangle as a function of polarization. Here, I used 0.6-μm-sized triangle and gap size of 50 nm in 50-nm-thick perfect conductor film, to mimic the resonant property and minimize calculation time. At resonance wavelength (around 1.7 μm, figure 4.16 (a)), results show a polarization independent transmission and sinusoidal field distribution along the contour, with changes its relative node position, demonstrated in figure 4.16 (b), (c) and (d). Therefore, total tunneling current across a barrier is suppressed by its corresponding current in opposite

direction while the local field strength is much larger than the non-resonant case.

4.4 Optical probe of THz tunneling current transient

In recent studies on a nonlinear transmission response of nanogaps by a strong THz field, they showed the incident power dependent nonlinear transmission by the electron tunneling effect which effectively blocks the transmitting THz field through the gap [11, 12, 89]. However, it was not easy to observe nonlinear response of nanogaps by the optical field. Since the optical field has much higher photon energy (~2 eV) compared with THz wave (~ 4 meV), it was not easy to simply increase the incident optical field strength due to the possible damage induced by the optical field. Another problem is the frequency of the optical field itself, which can be seen by observing the frequency-dependent dielectric property of the gap material. From the Maxwell-Ampère equation with including tunneling effect,

$$\nabla \times \mathbf{H} = \mathbf{J}_t + \frac{\partial \mathbf{D}}{\partial t} = (\sigma_t(\mathbf{E}) + \sigma_d)\mathbf{E} \qquad (4.12)$$

where $\mathbf{J}_t = \sigma_t(\mathbf{E})\mathbf{E}$ is the power dependent tunneling current driven by the incident optical field, $\sigma_t(\mathbf{E})$ is the effective tunneling conductivity, $\sigma_d = -i\omega\epsilon_0\epsilon_d$ denote the displacement conductivity and ϵ_d is the dielectric constant of gap material. The displacement current has negligible effect to the total conductivity under the THz field. Due to the rapid oscillation of optical field compared with the THz frequency, however, $\sigma_d/\sigma_t >> 1$ is fulfilled in the optical frequency [89]. Without the sufficiently small gap thickness (sub-5 Å regime) [90], the optical response such as nonlinear transmission by tunneling current is mostly negligible. In this section, I demonstrated the quantum tunneling driven by an optical field, which is expected to generate finite current with similar amplitude compared with the THz driven tunneling current.

Figure 4.17 (a) illustrate the experimental scheme. Optical pulse is divided from THz generation beam line (as 1% intensity), and focused at the

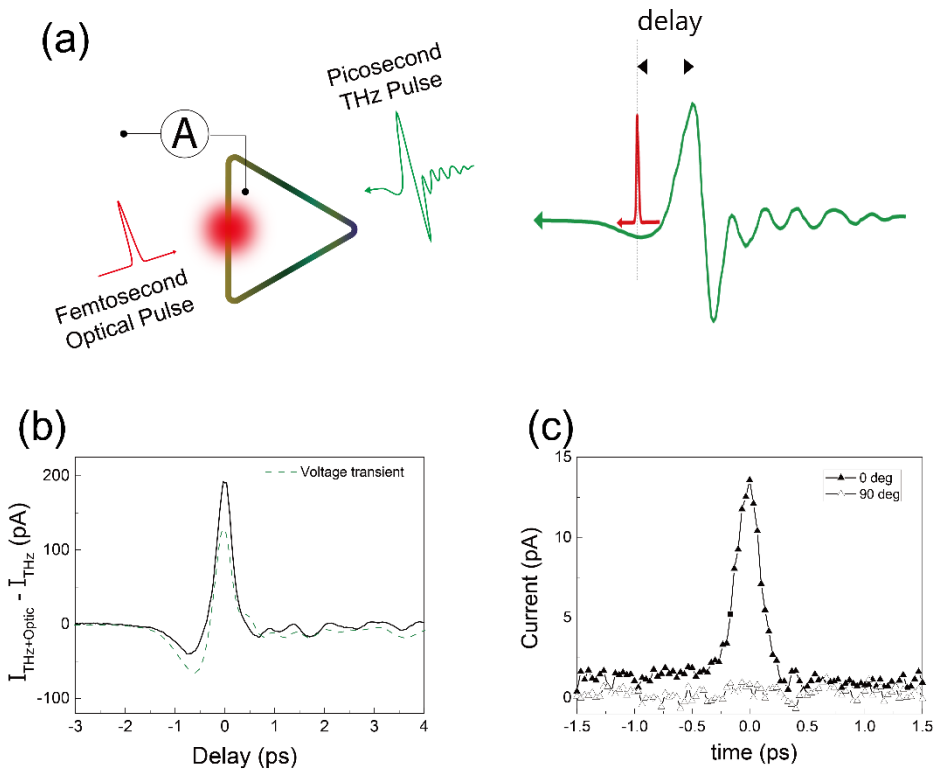

Figure 4.17 (a) Experimental scheme for THz tunneling current measurement under optical beam excitation. (b) Measured tunneling current under THz and optical field excitation, showing the optically induced current follows the THz gap voltage transient. Green dashed line is a guide for the eye, denoting THz voltage time profile (figure 4.6 (d)). Here, the side length of the triangle was 500 μm and gap size was 2 nm. (c) Optical polarization dependent current. 0 degree is defined as vertical to slit direction and 90 degrees as parallel to the slit direction. Incident optical power was relatively low compared with (b), showing only the peak current.

sample surface with ~ 50 μm spot size with the same illumination direction as THz pulse (figure 4.2 (a)). Incident THz beam is polarized vertical to the one of the sides of triangle, and the optical beam is focused at the nanogap where the THz field is applied in maximum. Figure 4.17 (b) shows the measured current as a function of the optical delay. Here, I used a 500-μm-sized triangle barrier to check the optical currents of a single junction (THz and optical fields are excited upon a single side of a triangle). Current-time profile follows the THz voltage profile with a slight distortion due to the

nonlinearity of tunneling process. Nevertheless, the optical measurement does not severely distort or change the order of the strength of currents; hence, it can be used to demonstrate time-resolved ultrafast current dynamics through the quantum barriers. I confirmed that the optical signal is coming from the additional optical voltage effect, from the measurement as a function of the optical polarization direction (figure 4.17 (c)), indicating that the signal was generated only when the gap field is maximally charged under the optical field by letting the optical polarization vertical to the gap direction.

4.4.1 Modeling optical response

Under the THz and optical field illumination, the barrier potential is affected by both fields simultaneously. Tunneling current through the barrier is driven by the sum of the light fields, sensitively affected by their temporal field profiles. Figure 4.18 (a) describes the situation when the optical field and THz field are illuminated at the gap together with a specific time delay, charges the gap and subsequently applies potential across the barrier. Compared the measured current under the optical and THz excitation together with the case of THz-only excitation, the femtosecond optical field additionally applies potential at a specific time under the quasi-constant voltage applied by the picosecond THz field. Due to the tunneling nonlinearity, the mostly sinusoidal oscillation of the optical field drives a non-zero current (figure 4.18 (b)).

I described the detailed effects of the optical field under THz voltage across the gap in figure 4.19. First, when the THz field is illuminated at the nanogap, temporal THz surface current is generated on the metal, following the THz field time profile (figure 4.2 (b)), thereby applies voltages across the gap as capacitive charging which is described by equation 4.2. The resulting time profile of the gap voltage is shown in top of figure 4.19 (a). Then the time-dependent potential subsequently drives tunneling current (bottom of figure 4.19 (a)) and the measured current would be the integral of the current profile for a one pulse cycle (average current, equation 4.7 divided by τ_{rep}). Next, I considered the optical field illuminated under the previous quasi-constant THz voltage profile with - 0.5 ps delay (figure 4.19 (b)) and zero delay (figure 4.19 (c)). In these cases, the optical fields additionally apply gap voltages at a specific delay, driving tunneling currents in the direction of the

applied background THz voltage (bottoms of figure 4.19 (b) and (c)).

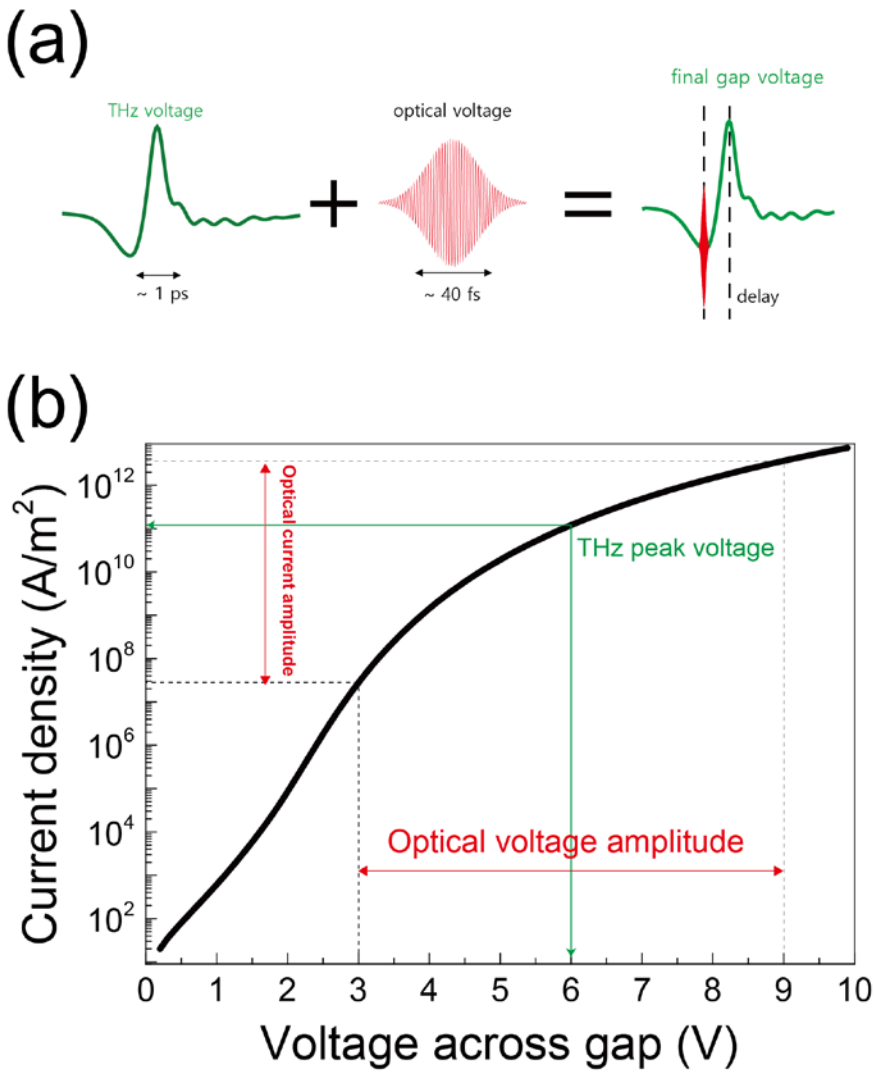

Figure 4.18 (a) Pictorial description for optical tunneling in a nanogap. A picosecond THz pulse and a femtosecond optical pulse are added and applies transient voltage across the gap. (b) Graphical illustration for optical tunneling under the quasi-constant THz field. Due to the strong nonlinearity of tunneling process, sinusoidal optical field generate tunneling current only for preferred polarity determined by THz field strength. Current vs. voltage relation was calculated based on the Simmons formula with barrier potential of 2.2 eV and gap size of 2 nm.

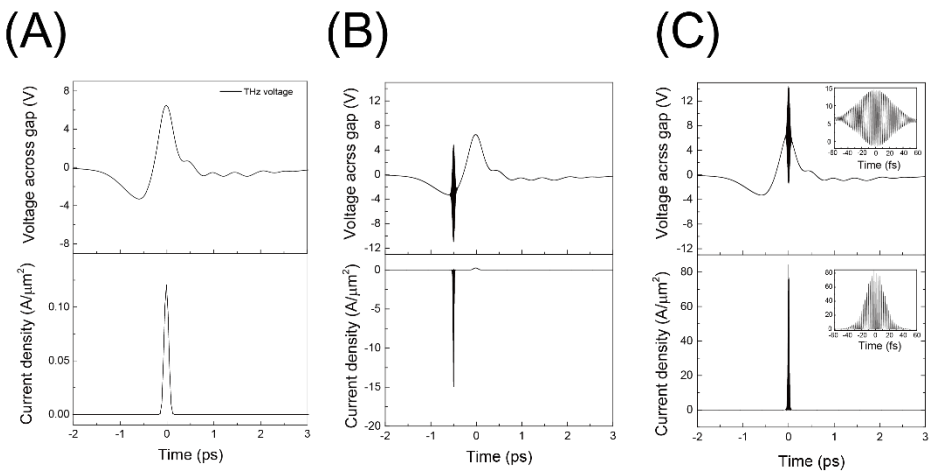

Figure 4.19 THz and optical field induced time profile of gap voltage (upper row) and tunneling current (bottom row). (a) Only the THz field illuminated, (b) optical beam incident with time delay of -0.5 ps with THz field and (c) 0 delay case. Inset of (c) show the magnified view near the zero delay.

4.4.2 Optical field enhancement

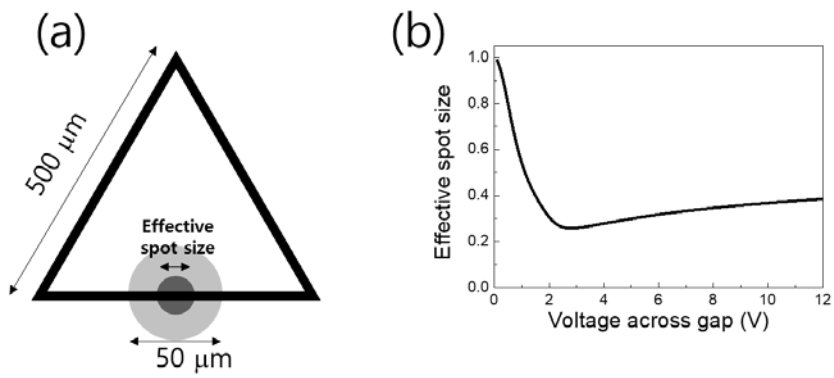

Figure 4.20 (a) Optical spot size and effective current spot size arising from the highly nonlinear tunneling current. (b) Calculated effective spot size as a function of applied optical voltage.

To analyze the optical tunneling current quantitatively, I considered a realistic situation illustrated in figure 4.20 (a). A relatively large triangle (side length of 500 μm) is used to simplify the problem, same as in previous measurement. Since the THz beam spot is larger than the side length (~ 1 mm),

I assumed an equally distributed THz field strength along the side and ignored the other adjacent sides. However, the optical spot size is around 50 μm, much smaller than the side length, thus care must be taken for the estimation of the length of the barrier contributing to the total current. I defined an effective spot size as the half width of the barrier normalized to the Gaussian-shaped original spot size, which affects the optical tunneling predominantly. Figure 4.20 (b) shows the calculated effective spot size as a function of the applied optical voltage across the gap. Due to the tunneling nonlinearity, the effective spot size is smaller than the original spot size. A minimum value occurring near 2.2 V reflects the barrier potential of Al_2O_3 layer used in this work, where the nonlinear tunneling curve (figure 4.18 (b)) shows maximum derivative.

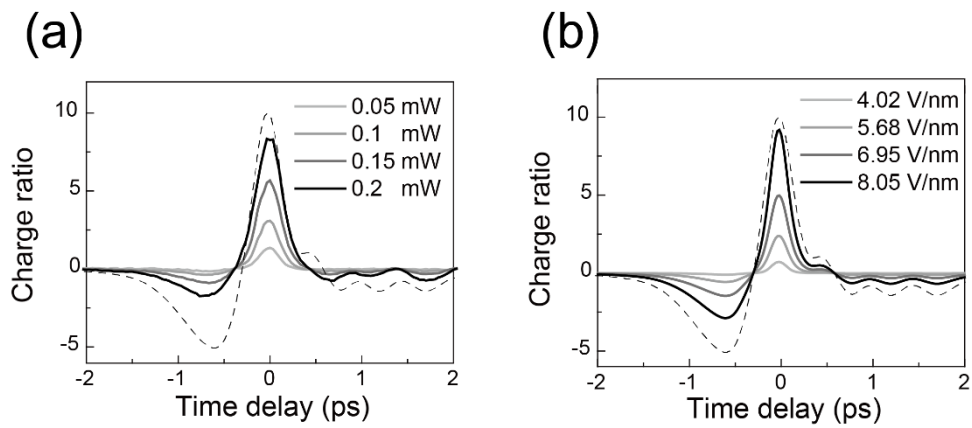

Figure 4.21 (a) Experimental and (b) theoretical time dependent optical current as a function of time delays. Legends in (a) indicate incident optical power and (b) applied optical field across a gap. Dashed line is a guide for the eye, indicating the THz gap voltage.

With this modeling method, I calculated the optical tunneling currents and compared with the experimental results. First, I measured optical tunneling currents by varying the incident optical power, as shown in figure 4.21 (a). Here, the charge ratio is defined by the normalized ratio between the tunneled charges under both optical field and THz field, and under only the THz field. More specifically, I measured tunneling currents only with the THz field, and denote this value as q_{THz}. Next, I repeated the measurement with optical and THz field both as a function of time delay t, and denote these values as $q_{THz+opt}(t)$. Then the charge ratio can be expressed by,

$$\text{charge ratio}(t) = \frac{q_{\text{THz+opt}}(t) - q_{\text{THz}}}{q_{\text{THz}}} \tag{4.13}$$

To theoretically calculate the charge ratio using previous modeling of optical tunneling, I used experimental incident powers (legends of figure 4.21 (a)) and multiplying suitable field enhancement factor of 800 nm beam at the 2 nm gap [13, 91] under the THz peak field of 6.5 V. Figure 4.21 (b) is the calculated results using fixed optical field enhancement factor of 5.8 and above parameters, showing similar behavior compared to the experimental results of figure 4.21 (a).

4.4.3 Extracting tunneling duration time

Using a power-dependent optical current data, I tried to extract a half-width of THz tunneling current pulse for a single THz pulse (temporal half width, shown in bottom of figure 4.19 (a)) to estimate the tunneling duration time. To accomplish this, I Gaussian-fitted the zero-delay peaks of experimentally measured optical current (figure 4.22 (a)) and extracted half width as a function of optical powers. First, I illuminated THz polarization as vanishing total current ($\varphi_{\text{pol}} = 90^{\text{o}}$, see figure 4.6 (a) for polarization notation), and measured half width of optical current as a function of optical field (now illuminates one of the right arms). And I changed input optical power from 25 uW to 250 uW on 70-μm-sized triangle. As shown in figure 4.22 (b), I extrapolated the measured half width at zero optical power and settled on ~ 0.2 ps.

The calculated half width in figure 4.19 (a) shows around half of the measured one (~ 0.1 ps). Note that the discrepancy between experiment and calculation (factor 2) may come from the experimentally unidentified exact optical pulse profile (assumed to be of a Gaussian profile in this work) or additional space charge potential inside the insulator under extremely high gap voltage (large current density condition), which may affect the tunneling currents [92]. Despite the mentioned uncertainties, the estimation of THz transient tunneling current – voltage relation using the measured tunneling current pulse width (~ 0.2 ps) shows reasonably good agreement with the calculated tunneling current (figure 4.11).

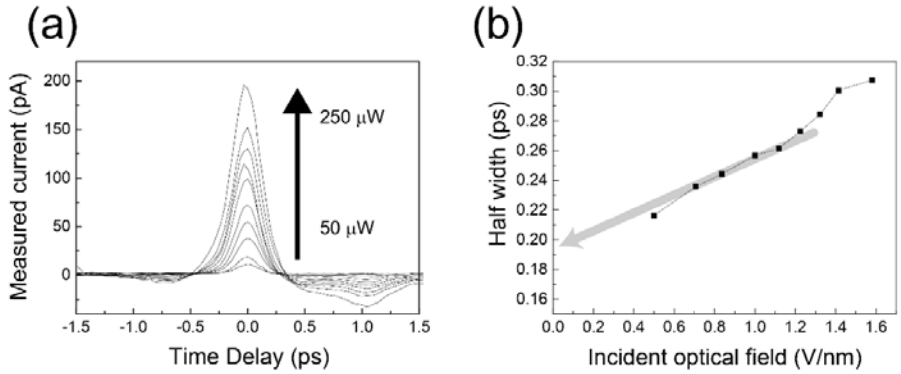

Figure 4.22 (a) Optical power dependent tunneling current in 70-μm-sized triangle barrier (gap size of 2 nm). Black arrow indicates the incident optical power. (b) Gaussian-fitted half-width of central peak (0 ps) as a function of incident optical field strength.

4.4.4 Optical probing of spatiotemporal tunneling current

The added optical pulse rapidly distorts the local potential barrier under the quasi-constant THz field, generating an additional, local tunneling current. The resulting current amplitude and direction, driven by the sinusoidal optical field, are critically dependent on the background THz voltage across the gap. The optical current is sensitively affected by the THz field strength at the specific position on the barrier and by the time delay between the THz and optical pulses, thus providing a way to visualize the spatiotemporal dynamics of the THz gap voltage. An interesting aspect of the optically modulated quantum barriers is the position-dependent ultrafast optical gating, as illustrated in figure 4.23 (b). After the polarization of the THz pulse is intentionally set to generate zero current (φ_{pol} = 45º), local modulation of the barrier by an optical pulse breaks the potential balance of the contour and generates ultrafast switching signals of opposite polarities depending on the side of the triangle shone by the optical pulse.

A DC bias is another control parameter for manipulating the tunneling current of the integrated barriers (figure 4.23 (a)). Figure 4.23 (c) shows the total current as a function of the time delay between the two pulses under a DC bias. Here, I generated a quasi-monochromatic, multi-cycled THz pulses using spectral filtering (~ 0.8 THz), and the polarization is set to φ_{pol} =

0º to maximize the response from the left side of the triangle. By sending an optical pulse to the side, I observed the DC-bias-modulated potential barrier reflected in a local THz current.

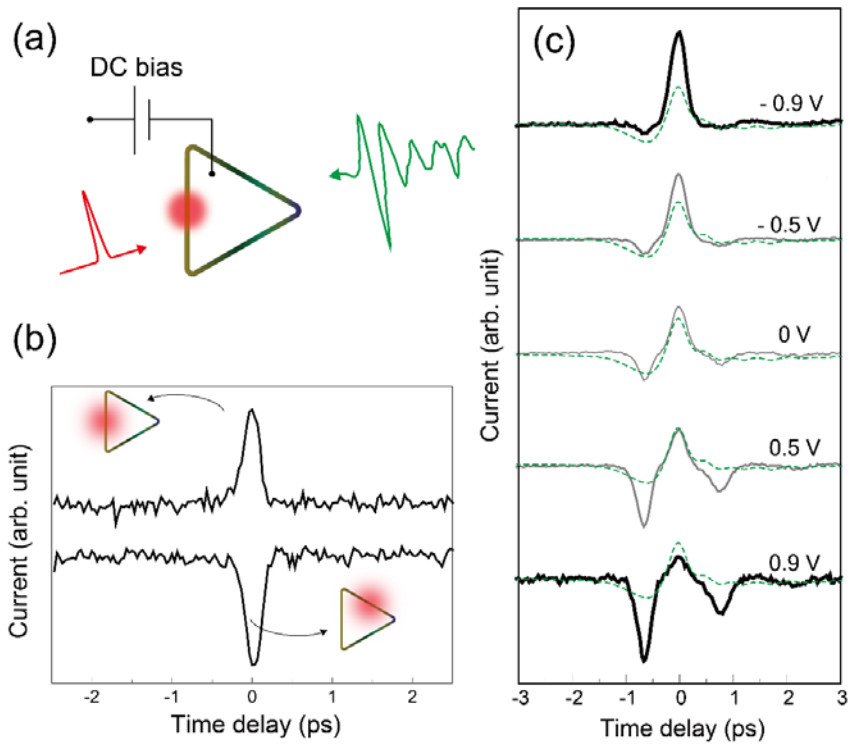

Figure 4.23 (a) Schematics of optical probing of spatiotemporal THz tunneling dynamics under a DC bias. (b) Positional dependent optical tunneling current under the THz polarization as vanishing current. (c) Local THz current probed by optical pulse under a DC bias which is denoted by DC bias strength on each curve. Greed dashed line indicates the THz voltage.

4.5 Ultrafast full-wave rectification of THz pulse

For the future application of the presented triangle tunneling barrier in ultrafast optoelectronics, I demonstrated the ultrafast full rectification of THz tunneling current using this ring barrier, shown in figure 4.24. The total

current along the whole contour can generate full-wave rectification of incident THz pulse in the ring barrier with a DC bias. The DC bias provides a unidirectional (i.e. into or out of the ring) current for each barrier of the triangle, resulting in a single polarity of total current independent of the incident pulse oscillation.

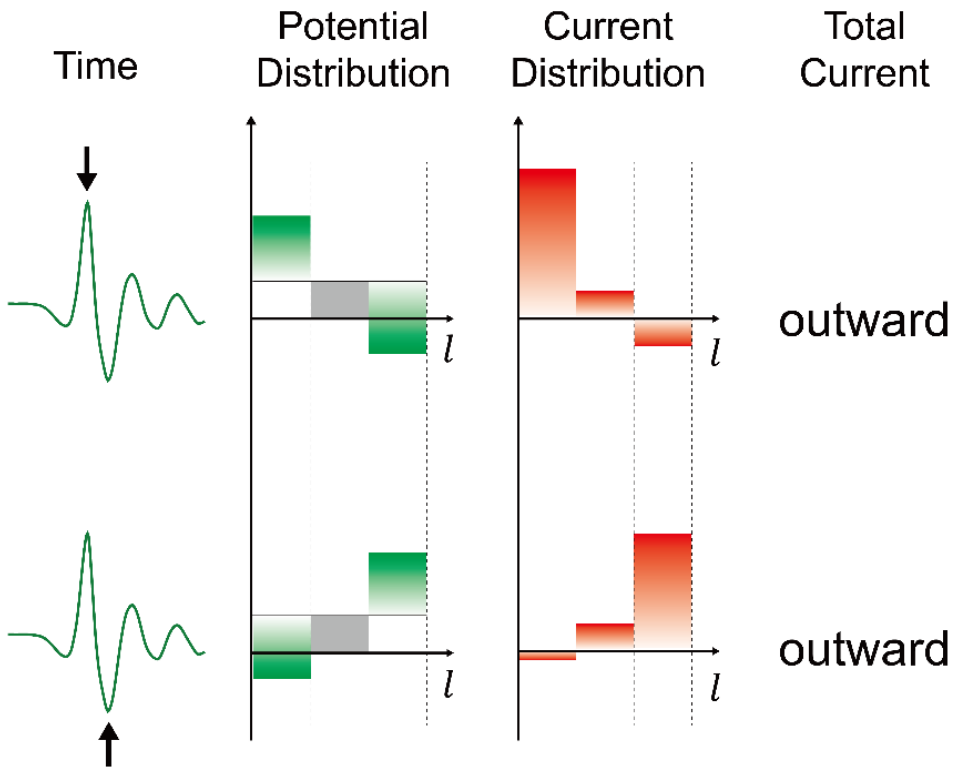

Figure 4.24 A pictorial description of full-wave rectification of THz pulse in a ring-barrier (see figure 4.6 (a) for arc length notation). Time column shows the incoming voltage profile and two example timings are denoted as black arrows. The applied DC bias is denoted as gray bars and black line in potential distribution. The resulting current pulse has a single polarity independent of the driving pulse direction.

The instantaneous total THz current can be visualized experimentally by the optical pulse. To probe the total current of the geometry, I increased the optical spot size to cover the entire loop with equal intensities, as shown at the top of figure 4.25. And the optical polarization is now set to a circularly polarized. Therefore, the optically modulated current directly shows the THz

total current through the entire barrier. By changing the THz polarization, I demonstrated the ultrafast full-wave rectification of THz current pulse and its modulation in figure 4.25. Note that other contour shapes (e.g. square or pentagon...) also can show the tunneling current shaping property, but the triangle provides high contrast between the manipulated current profiles as a function of polarization.

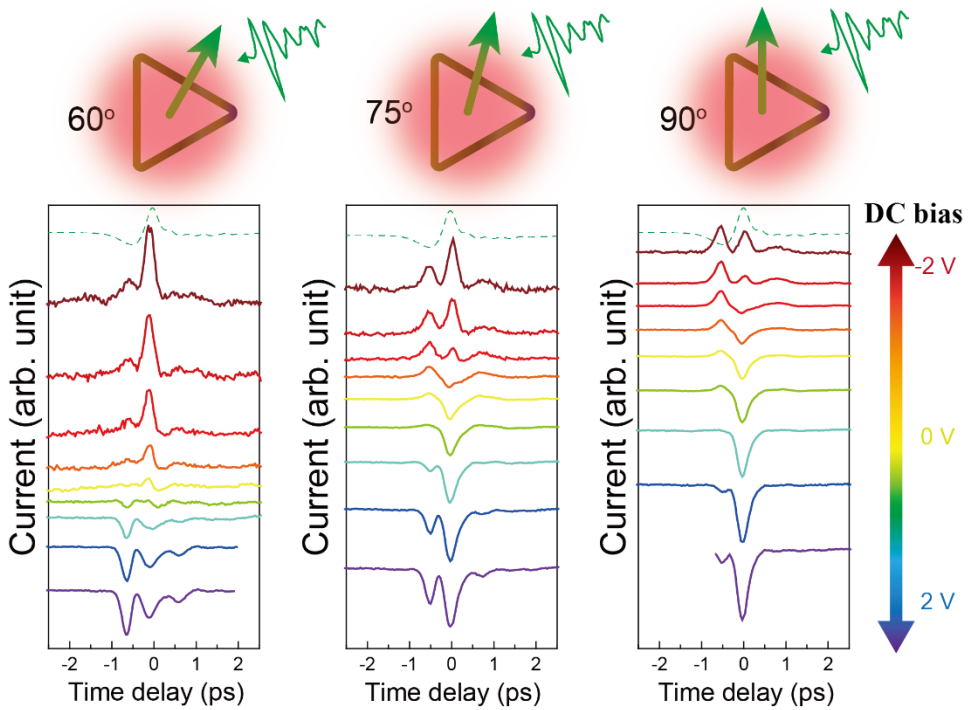

Figure 4.25 Experimental demonstration of ultrafast full-wave rectification of THz tunneling current from a triangular ring barrier (side length of 100 μm, gap size of 4 nm), visualized by circularly polarized optical pulse. By changing the THz polarization (at top of the figure), the output THz current shape can be modulated. Green dashed line indicates the incident THz voltage.

Figure 4.26 shows the calculation results of generated rectification current pulses by a 1 THz continuous wave illumination. The results clearly show the variation of pulse shape (half-wave or full-wave rectification) depending on the incoming THz polarization and DC bias. Also, one can notice that the total current generated by the THz wave (total THz current, first row) alone is very similar in shape compared with the total current

generated by the THz wave together with an optical pulse (total current, second row). Hence, the optical pulse performs the role of a probe well when visualizing the rectification current in time.

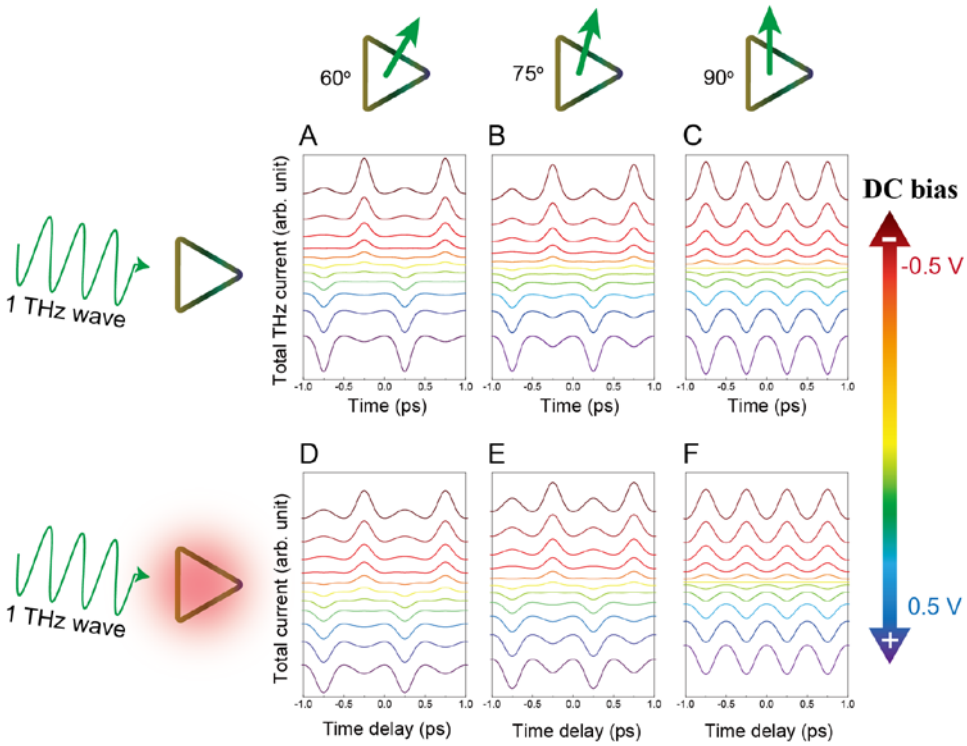

Figure 4.26 Theoretical demonstration of ultrafast full-wave rectification (first row) and its optical current (second row) of incoming 1 THz continuous wave in a triangular ring barrier under DC bias. THz peak voltage of 1 V and optical voltage of 3 V was used for the demonstration.

4.6 Conclusion

In conclusion, I demonstrated a highly nonlinear light-matter interaction, taking advantage of the two-dimensional, lateral geometry of closed-ring quantum barriers, whose lack of macroscopic inversion symmetry plays a vital role in the ultrafast optoelectronics. The ring-shaped nanogaps

vectorially charged by electromagnetically induced surface currents introduces geometry-dependent tunneling, further enriched by the femtosecond optical excitation at designated areas and time delays. By implementing the contour-integral concept and spatiotemporal control into the conventional one-dimensional tunneling, a multifunctional quantum device was realized, providing a platform for optical logic gate (figure 4.27), THz multiplexing (figure 4.28), ultra-high bandwidth communications and wireless energy conversion.

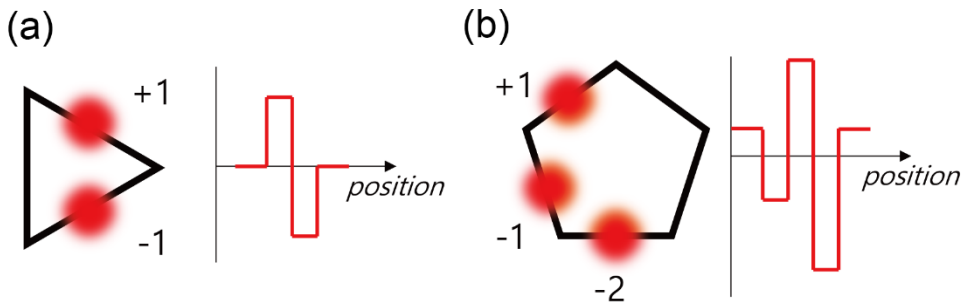

Figure 4.27 Position-sensitive optical switching device in (a) a triangle barrier and (b) a pentagon barrier.

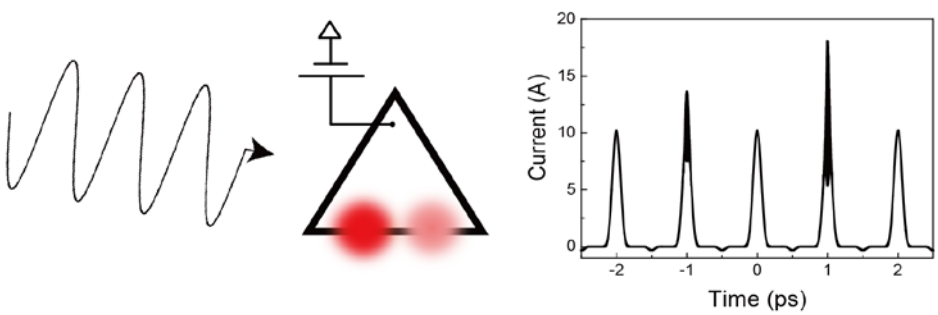

Figure 4.28 Ultrafast current-pulse generator. Multiple optical pulses and THz wave illuminate on a single barrier with predefined delays, generating an arbitrary-shaped current pulses.

Chapter 5. Conclusion

In this thesis, I studied strong light-matter interaction by optical field enhancement in nanogaps. In first part of this thesis, I estimated optical field enhancement of nanogaps by far-field transmission measurements. Direct transmission through a metallic film affected to the measurement, and suitable solutions are provided for each cases, comprising of preparing optically-opaque metal films and exploiting interferometric method. Kirchhoff integral formalism based analysis were successfully estimated optical field enhancement in nanogaps, and theoretical calculation confirmed the Fabry-Pérot resonance of the field enhancement. The resonantly enhanced optical and near infrared field can be tuned by changing the gap size, and greatly enhanced the photoluminescence of metal. Extremely strong field enhancement and applying high power THz field lead to electromagnetically driven tunneling phenomena in the nanogaps. To access to the tunneling current in nanogaps experimentally, I introduced geometrical shape in the tunneling barriers whose lack of inversion symmetry resulted in a tunneling rectification. The contour integration concept of tunneling current along the perimeter of nanogap results non-vanishing rectified charges. Optical field also plays key role in electromagnetic tunneling together with the THz field. Time-dependent tunneling dynamics can be measured experimentally by the pump-probe technique, which provides THz gap voltages spatiotemporally. Together with the theoretical analysis, optical field enhancement factor was extracted by optical tunneling current quantifications, similar results compared with the Kirchhoff integral formalism method. This work opens up a new type of research platform toward ultrafast optoelectronics, light driven circuitry and macroscopic quantum phenomena.

Appendix

A.1 Kirchhoff integral for wide-angle collection experiments

For optical transmission experiments in this thesis, I used lens whose focal length are longer than 25 mm to guide and collect optical beams. For example, broadband spectroscopy presented in chapter 3, it is much benefit using a long focal length lens (~ 300 mm) to avoid chromatic aberration and calculate coverage ratio which is simply derived from the sample periodicity and gap sizes. In some cases, such as narrow band experiment or local measurement of samples, high numerical aperture (N.A.) objective lens would be a better choice, which provides large magnification and numerical aperture specialized for small signal collection from a sample.

When exploiting objective lens for estimating field enhancement of single nanogap, care must be taken about the collection angle and spot size since the Kirchhoff integral I used before was based on the assumption that the detector was placed in normal direction with small collecting angle (such as large beam spot illumination and grating-type sample whose radiation pattern is forwardly directed compared to the single slit), or the diffracted light from the reference beam and sample have quite uniform angular distribution, thereby I can safely ignore the factor $\exp(-i\mathbf{k}\cdot\mathbf{r}')$ in the integrand. For wide angle collection experiment, however, estimation error is naturally involved if someone uses the equation 3.5 directly. Especially, the error comes mainly from the mismatch of radiation patterns between reference beam and light emanating from samples.

Figure A.1 demonstrate for the reference and nanogap transmission measurement. First, let's consider the reference measurement. The far-field diffracted from circular aperture placed in the *xy* plane under normal incidence with uniform intensity distribution can be calculated by Kirchhoff integral [28],

$$\mathbf{E}_{\mathrm{ref}}(\mathbf{r}) = \frac{ie^{ikr}}{2\pi r}\pi a^2 E_0(\mathbf{k}\times\boldsymbol{\epsilon}_2)\frac{2J_1(kw\sin\theta)}{kw\sin\theta} \qquad (A1.1)$$

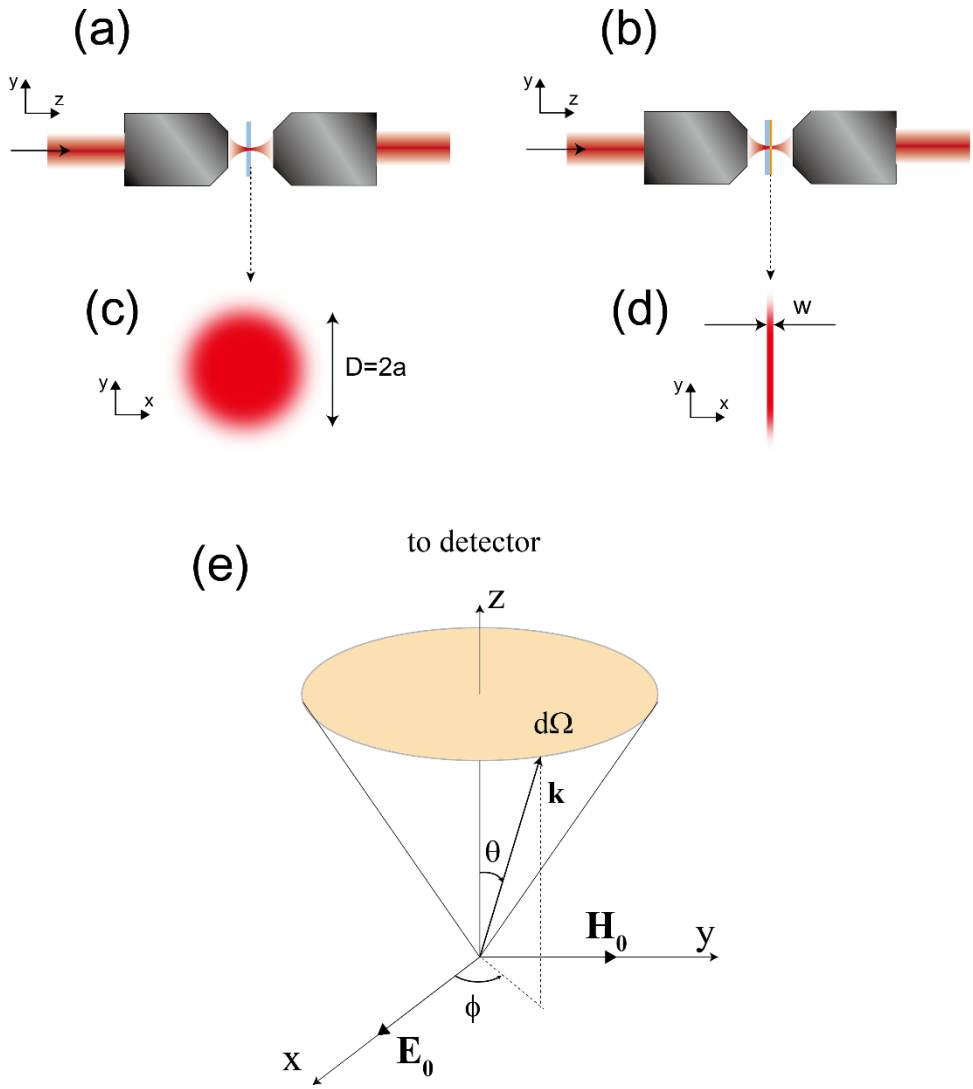

Figure A.1 Schematic for transmission measurement with high numerical aperture (N.A.) objective lens. Incident optical beam is focused at (a) a bare substrate and (b) a nanogap. Magnified view of the focused spot on (c) a bare substrate and (d) nanogap. Here, the focused optical beam is assumed to have uniform intensity profile in the beam spot. (e) Detection scheme under plane wave incident.

where **r** denotes observation point, *a* (=*D*/2) is the beam radius, **k** is the

wavevector directed toward observation point, $\boldsymbol{\epsilon}_2$ is unit vector directing y-axis and J_1 is Bessel function of the first kind of order 1. The total photons collected into a solid angle Ω with collection angle θ_{col} is proportional to

$$\int_{\Omega} |\boldsymbol{E}_{\text{ref}}|^2 r^2 d\Omega \tag{A1.2}$$

This can be reduced to

$$\left(E_0(\pi a^2)\right)^2 A_{\text{ref}}(\theta_{\text{col}}) \tag{A1.3}$$

where $A_{\text{ref}}(\theta_{\text{col}})$ is an integral

$$\frac{1}{\pi}\int_{\cos(\theta_{\text{col}})}^{1} \left[\frac{J_1\left(ka\sqrt{1-t^2}\right)}{a\sqrt{1-t^2}}\right]^2 (1+t^2)\, dt \tag{A1.4}$$

Next, the far-field diffracted from a nanogap can be written by

$$\mathbf{E}_{\text{gap}}(\mathbf{r}) = \frac{ie^{ikr}}{2\pi r} E_g(\mathbf{k}\times\boldsymbol{\epsilon}_2) \int_{-g}^{g} dx' e^{-ikx'\sin\theta\cos\phi} \int_{-a}^{a} dy' e^{-iky'\sin\theta\sin\phi} \tag{A1.5}$$

where $g = w/2$ is half of the gap size and assumed the small aspect ratio $w/D << 1$ such that the integration can be separated in x and y. Similarly, the photons collected through the collection angle Ω is

$$\int_{\Omega} \left|\boldsymbol{E}_{\text{gap}}\right|^2 r^2 d\Omega = \left(E_{\text{gap}}(4ag)\right)^2 A_{\text{gap}}(\theta_{\text{col}}) \tag{A1.6}$$

$$A_{\text{gap}}(\theta_{\text{col}}) = \int_{\Omega} (\cos^2\theta + \sin^2\theta\cos^2\phi) \left[\frac{1}{2\pi}\frac{\sin(kg\sin\theta\cos\phi)}{kg\sin\theta\cos\phi}\frac{\sin(ka\sin\theta\sin\phi)}{ka\sin\theta\sin\phi}\right]^2 d\Omega \tag{A1.7}$$

Measured transmission (T) is simply the equation A1.6 divided by A1.3. Expressing T/β using above parameters,

$$\frac{\sqrt{T}}{\beta} = \frac{E_{\text{gap}}}{E_0}\sqrt{\frac{A_{\text{gap}}(\theta_{col})}{A_{\text{ref}}(\theta_{col})}} \tag{A1.8}$$

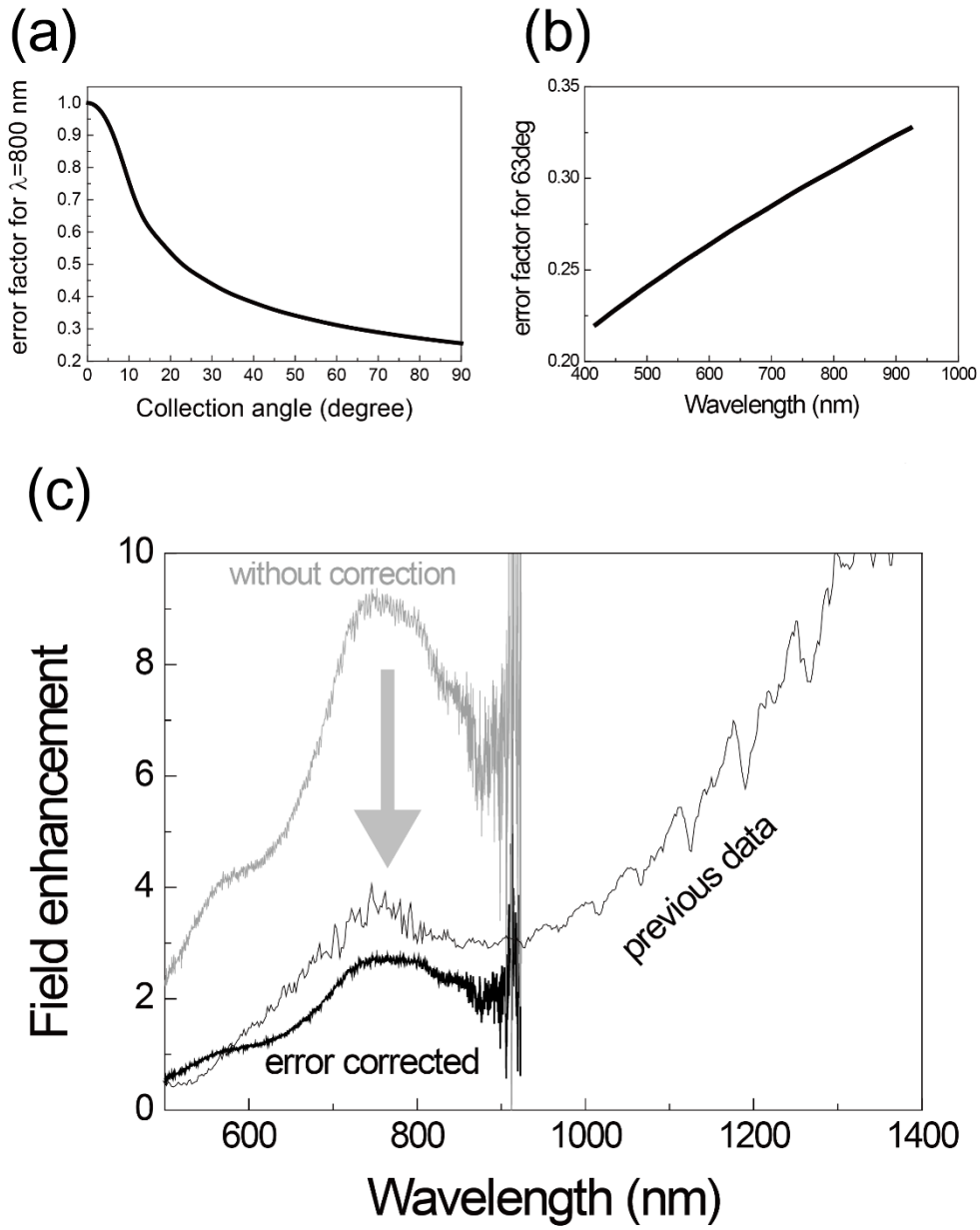

Figure A.2 Calculated error factor as a function of (a) collection angle and (d) wavelength. Beam size is assumed to 5 um and the gap size is 10 nm. (c) Estimated field enhancement of 10 nm gap measured by high N.A. (0.89) lens in optical regime, compared with low N.A. measurement. Corrected data are ended at 900 nm due to the source spectrum limit (Halogen lamp).

where $\beta = 4ag/\pi a^2$ is the coverage ratio. Comparing equation A1.8 with equation 3.5, additional angular factor is included, which is reduced to 1 for

$\theta_{col} \approx 0$ case. Therefore, field enhancement factor is now expressed by

$$\frac{E_{gap}}{E_0} = \frac{\sqrt{T}}{\beta}\gamma \qquad (A1.9)$$

with an error factor $\gamma = \sqrt{A_{\mathrm{ref}}(\theta_{col})/A_{\mathrm{gap}}(\theta_{col})}$.

Figure A.2 shows the calculated error factor γ for a 10 nm gap under a beam size of 5 μm as a function of (a) collection angle θ_{col} and (b) incident wavelength. By including the error factor for the transmission measurement using objective lens (N.A. 0.89, corresponding $\theta_{col} \sim 63^{o}$) in optical region, it successfully reproduced field enhancement of 10 nm gap of the previous results (figure A.2 (c)).

As expected, increasing θ_{col} takes larger errors. And for larger the wavelength, the error becomes smaller. This is due to the radiation pattern mismatch between nanogap field and reference field. The angular pattern, $e^{-i\mathbf{k}\cdot\mathbf{r}}$ is close to unity when the gap size is very small ($\mathbf{k} >> \mathbf{r}'$) or the wavelength is very large ($\mathbf{k} << 1$) for a fixed beam size. This explains why the THz measurement is free from the collection error compared with the optical measurement, since the aperture size for reference measurement (~ 1 mm) is smaller or comparable to the wavelength (λ = 3 mm for 0.1 THz), thus similar radiation pattern is generated from reference measurement and nanogap measurement. For example, detection angle for a parabolic mirror ($\theta_{col} \sim 25^{o}$) makes error below than 1 % at 1 THz.

A.2 Theoretical calculation of electromagnetic fields near the metallic grating composed of 4-layers

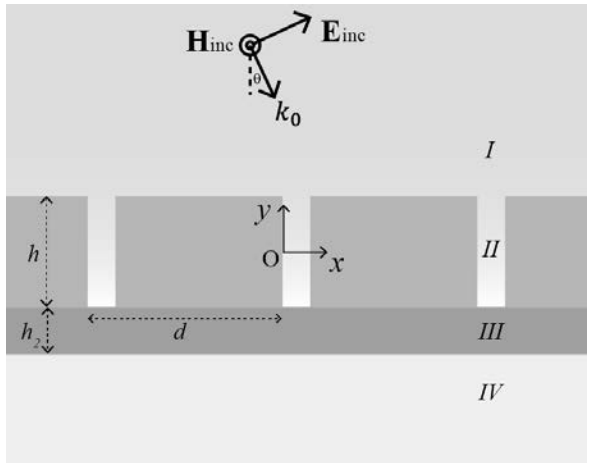

Figure A.3 Schematic for the electromagnetic field calculation near a metallic grating.

Plane wave expansion on each region [47] is expressed by

$$H_{1z} = \sum_{p=-\infty}^{\infty} \left(R_{1,p} e^{ik_{1y,p}\left(y-\frac{h}{2}\right)} + \delta_{p,0} e^{-ik_{1y,0}\left(y-\frac{h}{2}\right)} \right) e^{ik_{x,p}x} \quad \text{(A2.1a)}$$

$$H_{3z} = \sum_{p=-\infty}^{\infty} \left(R_{3,p} e^{ik_{3y,p}\left(y+\frac{h}{2}\right)} + T_{3,p} e^{-ik_{3y,p}\left(y+\frac{h}{2}\right)} \right) e^{ik_{x,p}x} \quad \text{(A2.1b)}$$

$$H_{4z} = \sum_{p=-\infty}^{\infty} T_{4,p} e^{-ik_{4y,p}\left(y+\frac{h}{2}+h_2\right)} e^{ik_{x,p}x} \quad \text{(A2.1c)}$$

where R and T are reflection and transmission coefficients, respectively, and $k_{x,p}$ is given by the scattered light from the grating, $k_{x,p} = \sqrt{\epsilon_1} k_0 \sin\theta + 2\pi p/d$ and satisfying the Helmholtz equation $\epsilon_i k_0^2 = k_{x,p}^2 + k_{iy,p}^2$ and i runs 1,2 4. Waveguide field inside the gap is expanded by trigonometric functions①,

$$H_{2z} = \sum_{m=0}^{\infty} u_m(x) v_m(y) \quad \text{(A2.1d)}$$

① It can be considered as a linear combination of planewave components; thus it is fundamentally the same expression as equation 3.8 in chapter 3.

where $u_m(x) = A_m\sin(k_{2x,m}x) + \cos(k_{2x,m}x)$ and $v_m(y) = a_m\sin(k_m y) + b_m\cos(k_m y)$.

By imposing surface impedance boundary condition [46] $\mathbf{E}_{\|} = Z_{\text{metal}}(\hat{n} \times \mathbf{H})_{\|}$ on each gap boundary [44, 47], where $Z_{\text{metal}} = \sqrt{\frac{\mu\mu_0}{\epsilon\epsilon_0}} = \frac{Z_0}{\sqrt{\epsilon}}$

(1) $E_{2y}|_{x=0} = -\frac{Z_0}{\sqrt{\epsilon}} H_{2z}|_{x=0}$

$A_m = \frac{\eta_2}{k_m}$, where $\eta_2 = \frac{\epsilon_2 k_0}{i\sqrt{\epsilon_M}}$

(2) $E_{2y}|_{x=w} = \frac{Z_0}{\sqrt{\epsilon}} H_{2z}|_{x=w}$

$$\tan(k_m w) = \frac{2\eta_2 k_m}{k_m^2 - \eta_2^2} \tag{A2.2}$$

indicates the eigenvalues k_m (waveguide mode) with a mode number m.

Boundary matching

1. $y = h/2$

(1) H_z continuous

$$\sum_{p=-\infty}^{\infty} \left(R_{1,p} + \delta_{p,0}\right) e^{ik_{x,p}x} = \sum_{m=0}^{\infty} u_m(x)(a_m + b_m)$$

Multiplying $u_{m'}(x)$ and integrate $[0, w]$ on both sides,

$$\sum_{p=-\infty}^{\infty} \left(R_{1,p} + \delta_{p,0}\right) K_{m,p} = a_m + b_m \tag{A2.3a}$$

where $K_{m,p} = \frac{1}{I_m}\int_0^w u_m(x) e^{ik_{x,p}x} dx = \frac{e^{ik_{x,p}w}}{I_m\left(k_{2x,m}^2 - k_{x,p}^2\right)}\left[\left(-ik_{x,p} + \eta_2\right)e^{-ik_{x,p}w} + \frac{k_{2x,m}^2 + \eta_2^2}{k_{2x,m}^2 - \eta_2^2}\left(ik_{x,p} + \eta_2\right)\cos\left(k_{2x,m}w\right)\right]$

and normalization factor $I_m = \int_0^w \left(u_m(x)\right)^2 dx = \left[1 + \left(\frac{\eta_2}{k_{2x,m}}\right)^2\right]\frac{w}{2} + \frac{\eta_2}{k_{2x,m}^2}$

(2) E_x continuous

$$i\frac{Z_0}{k_0\epsilon_1}\sum_{p=-\infty}^{\infty} ik_{1y,p}\left(R_{1,p} - \delta_{p,0}\right)e^{ik_{x,p}x}$$

$$= i\frac{Z_0}{k_0\epsilon_2}\sum_{m=0}^{\infty} u_m(x)k_{2y,m}\left(a_m\cot\left(k_{2y,m}h/2\right) - b_m\tan\left(k_{2y,m}h/2\right)\right)$$

for $0 < x < w$

$$= \frac{Z_0}{\sqrt{\epsilon}} \sum_{p=-\infty}^{\infty} \left(R_{1,p} + \delta_{p,0}\right) e^{ik_{x,p}x}$$

for $w < x < d$.

Multiplying $\exp(-ik_{x,p}x)/d$ integrate $[0, d]$ on both sides,

$$ik_{1y,q}\left(R_{1,q} - \delta_{q,0}\right) = \frac{\epsilon_1}{\epsilon_2} \sum_{m=0}^{\infty} J_{q,m} k_{2y,m} \left(a_m \cot\left(\frac{k_{2y,m}h}{2}\right) - b_m \tan\left(\frac{k_{2y,m}h}{2}\right)\right) + \eta_1 \sum_{p=-\infty}^{\infty} \left(R_{1,p} + \delta_{p,0}\right) Q_{q,p} \quad \text{(A2.3b)}$$

where $J_{q,m} = \frac{1}{d}\int_0^w u_m(x) e^{-ik_{x,q}x} dx = \frac{e^{-ik_{x,p}w}}{d\left(k_{2x,m}^2 - k_{x,n}\right)} \left[\left(ik_{x,p} + \eta_2\right) e^{ik_{x,p}w} + \frac{k_{2x,m}^2 + \eta_2^2}{k_{2x,m}^2 - \eta_2^2}\left(-ik_{x,p} + \eta_2\right)\cos\left(k_{2x,m}w\right)\right]$

and $Q_{q,p} = \frac{1}{d}\int_w^d e^{-i\left(k_{x,q}x - k_{x,p}x\right)} dx$

2. $y = -h/2$

(1) H_z continuous

$$\sum_{p=-\infty}^{\infty} \left(R_{3,p} + T_{3,p}\right) K_{m,p} = -a_m + b_m \quad \text{(A2.4a)}$$

(2) E_x continuous

$$ik_{3y,q}\left(R_{3,q} - T_{3,q}\right) = \frac{\epsilon_3}{\epsilon_2} \sum_{m=0}^{\infty} J_{q,m} k_{2y,m} \left(a_m \cot\left(\frac{k_{2y,m}h}{2}\right) - b_m \tan\left(\frac{k_{2y,m}h}{2}\right)\right) - \eta_3 \sum_{p=-\infty}^{\infty} \left(R_{3,p} + T_{3,p}\right) Q_{q,p} \quad \text{(A2.4b)}$$

3. $y = -h/2 - h_2$

(1) H_z continuous

$$R_{3,p} e^{-ik_{3y,p}h_2} + T_{3,p} e^{ik_{3y,p}h_2} = T_{4,p} \quad \text{(A2.5a)}$$

(2) E_x continuous

$$\frac{k_{3y,p}}{\epsilon_3}\left(R_{3,p} e^{-ik_{3y,p}h_2} - T_{3,p} e^{ik_{3y,p}h_2}\right) = -\frac{k_{4y,p}}{\epsilon_4} T_{4,p} \quad \text{(A2.5}b\text{)}$$

Let $\frac{k_{iy}}{\epsilon_i} = \overline{k}_{iy}$, and $\frac{\eta_i}{\epsilon_i} = \eta_0$. Then equation A2.5a and A2.5b can be simplified by,

$$R_{3,p} = \xi_p T_{4,p} \qquad \text{(A2.5a}'\text{)}$$

$$T_{3,p} = \zeta_p T_{4,p} \qquad \text{(A2.5b}'\text{)}$$

where $\xi_p = \frac{e^{ik_{3y,p}h_2}}{2\overline{k}_{3y,p}}\left[\overline{k}_{3y,p} - \overline{k}_{4y,p}\right]$ and $\zeta_p = \frac{e^{-ik_{3y,p}h_2}}{2\overline{k}_{3y,p}}\left[\overline{k}_{3y,p} + \overline{k}_{4y,p}\right]$

Using equation A2.5a′ and A2.5b′ to eliminate $R_{3,p}$ and $T_{3,p}$ in equation A2.4a and A2.4b and expressing equations A2.3a, A2.3b, A2.4a and A2.4b into a matrix notation, above equations are now written by,

$$a_m + b_m = K_{m,p}\left(R_{1,p} + \delta_{p,0}\right) \qquad \text{(A2.6a)}$$

$$-a_m + b_m = \widetilde{K}_{m,p} T_{4,p} \qquad \text{(A2.6b)}$$

$$i\overline{k}_{1y,q}\left(R_{1,q} - \delta_{q,0}\right) = J_{q,m}\overline{k}_{2y,m}(a'_m - b'_m) + \eta_0 Q_{q,p}\left(R_{1,p} + \delta_{p,0}\right) \qquad \text{(A2.6c)}$$

$$i\overline{k}_{3y,q}\left(\xi_q - \zeta_q\right)T_{4,q} = J_{q,m}\overline{k}_{2y,m}(a'_m + b'_m) - \eta_0 Q_{q,p}\left(\xi_p + \zeta_p\right)T_{4,p} \qquad \text{(A2.6d)}$$

where $\widetilde{K}_{m,p} = K_{m,p}\left(\xi_p + \zeta_p\right)$, $a'_m = a_m \cot(k_{2y,m}h/2)$ and $b'_m = b_m \tan(k_{2y,m}h/2)$.

Let $Q^{1\pm}_{q,p} = i\overline{k}_{1y,q}\delta_{q,p} \pm \eta_0 Q_{q,p}$ and $Q^{3\pm}_{q,p} = i\overline{k}_{3y,q}\left(\xi_p - \zeta_p\right)\delta_{q,p} \pm \eta_0 Q_{q,p}\left(\xi_p - \zeta_p\right)$.

Rewriting $R_{1,p}$ and $T_{4,p}$ in equation A2.6c and A2.6d using these definitions,

$R_{1,p} = [Q^{1-}]^{-1}_{p,q} Q^{1+}_{q,0} + U^1_{p,m}(-a'_m + b'_m)$

where $U^1_{p,m} = [Q^{1-}]^{-1}_{p,q} J_{q,m}\overline{k}_{2y,m}$.

$T_{4,p} = U^3_{p,m}(a'_m + b'_m)$

where $U^3_{p,m} = [Q^{3+}]^{-1}_{p,q} J_{q,m}\overline{k}_{2y,m}$

Expressing a_m and b_m as a function of $R_{1,p}$ and by $T_{4,p}$ by rearranging equation A2.6a and A2.6b, and inserting above $R_{1,p}$ and $T_{4,p}$,

$$a_m = \frac{1}{2}W^-_{m,n}a'_n - \frac{1}{2}W^+_{m,n}b'_n + F_m \qquad \text{(A2.7a)}$$

$$b_m = \frac{1}{2}W^+_{m,n}a'_n - \frac{1}{2}W^-_{m,n}b'_n + F_m \qquad \text{(A2.7b)}$$

where $W^\pm_{m,n} = K_{m,p}U^1_{p,n} \pm \widetilde{K}_{m,p}U^3_{p,n}$ and $F_m = \frac{1}{2}K_{m,p}\left(\delta_{p,0} + [Q^{1-}]^{-1}_{p,q}Q^{1+}_{q,0}\right)$.

Expressing equation A2.7a and A2.7b as a function of a_n and b_n, and rearranging terms as following,

$$\left[\delta_{mn} - W_{m,n}^{-}\cot\left(\frac{k_{2y,n}h}{2}\right)\right]a_n + W_{m,n}^{+}\tan\left(\frac{k_{2y,n}h}{2}\right)b_n = F_m \quad \text{(A2.8a)}$$

$$-W_{m,n}^{-}\cot\left(\frac{k_{2y,n}h}{2}\right)a_n + \left[\delta_{mn} - W_{m,n}^{-}\tan\left(\frac{k_{2y,n}h}{2}\right)\right]b_n = F_m \quad \text{(A2.8b)}$$

Finally, the coefficients a_n and b_n can be calculated numerically by inverse matrix operation. Subsequently, the remaining planewave coefficients, R and T, can be calculated.

Bibliography

1. M. A. Seo, H. R. Park, S. M. Koo, D. J. Park, J. H. Kang, O. K. Suwal, S. S. Choi, P. C. M. Planken, G. S. Park, N. K. Park, Q. H. Park, and D. S. Kim, Nat Photon **3**, 152-156 (2009).
2. C. Lumdee, B. Yun, and P. G. Kik, ACS Photonics **1**, 1224-1230 (2014).
3. G. Boyd, Z. Yu, and Y. Shen, Physical Review B **33**, 7923-7936 (1986).
4. S. F. Tan, L. Wu, J. K. W. Yang, P. Bai, M. Bosman, and C. A. Nijhuis, Science **343**, 1496-1499 (2014).
5. J. A. Scholl, A. L. Koh, and J. A. Dionne, Nature **483**, 421 (2012).
6. W. Zhu, R. Esteban, A. G. Borisov, J. J. Baumberg, P. Nordlander, H. J. Lezec, J. Aizpurua, and K. B. Crozier, Nature Communications **7**, 11495 (2016).
7. Y. Tanaka, A. Sanada, and K. Sasaki, Scientific Reports **2**, 764 (2012).
8. C. Ciracì, R. T. Hill, J. J. Mock, Y. Urzhumov, A. I. Fernández-Domínguez, S. A. Maier, J. B. Pendry, A. Chilkoti, and D. R. Smith, Science **337**, 1072-1074 (2012).
9. J. A. Scholl, A. García-Etxarri, A. L. Koh, and J. A. Dionne, Nano Letters **13**, 564-569 (2013).
10. X. Chen, H.-R. Park, M. Pelton, X. Piao, N. C. Lindquist, H. Im, Y. J. Kim, J. S. Ahn, K. J. Ahn, N. Park, D.-S. Kim, and S.-H. Oh, Nature Communications **4**, 2361 (2013).
11. Y.-M. Bahk, B. J. Kang, Y. S. Kim, J.-Y. Kim, W. T. Kim, T. Y. Kim, T. Kang, J. Rhie, S. Han, C.-H. Park, F. Rotermund, and D.-S. Kim, Physical Review Letters **115**, 125501 (2015).
12. J.-Y. Kim, B. J. Kang, J. Park, Y.-M. Bahk, W. T. Kim, J. Rhie, H. Jeon, F. Rotermund, and D.-S. Kim, Nano Letters **15**, 6683-6688 (2015).
13. J. S. Ahn, T. Kang, D. K. Singh, Y.-M. Bahk, H. Lee, S. B. Choi, and D.-S. Kim, Opt. Express **23**, 4897-4907 (2015).
14. K. Lee, J. Jeong, Y.-M. Bahk, J. Rhie, I.-K. Baek, B. J. Lee, Y. H. Kang,

S. Hong, G.-S. Park, and D.-S. Kim, ACS Photonics **3**, 537-542 (2016).

15. H. T. Miyazaki, and Y. Kurokawa, Physical Review Letters **96**, 097401 (2006).
16. D. R. Ward, F. Huser, F. Pauly, J. C. Cuevas, and D. Natelson, Nat Nano **5**, 732-736 (2010).
17. F. J. Garcia-Vidal, L. Martin-Moreno, T. W. Ebbesen, and L. Kuipers, Reviews of Modern Physics **82**, 729-787 (2010).
18. K. Yoshioka, I. Katayama, Y. Minami, M. Kitajima, S. Yoshida, H. Shigekawa, and J. Takeda, Nat Photon **10**, 762-765 (2016).
19. T. L. Cocker, D. Peller, P. Yu, J. Repp, and R. Huber, Nature **539**, 263-267 (2016).
20. A. Bouhelier, M. Beversluis, A. Hartschuh, and L. Novotny, Physical Review Letters **90**, 013903 (2003).
21. F. J. García-Vidal, and J. B. Pendry, Physical Review Letters **77**, 1163-1166 (1996).
22. Y. Fang, N.-H. Seong, and D. D. Dlott, Science **321**, 388-392 (2008).
23. P. N. Sanda, J. M. Warlaumont, J. E. Demuth, J. C. Tsang, K. Christmann, and J. A. Bradley, Physical Review Letters **45**, 1519-1523 (1980).
24. J. R. Lombardi, and R. L. Birke, The Journal of Physical Chemistry C **112**, 5605-5617 (2008).
25. S. Mubeen, S. Zhang, N. Kim, S. Lee, S. Krämer, H. Xu, and M. Moskovits, Nano Letters **12**, 2088-2094 (2012).
26. J. Jeong, J. Rhie, W. Jeon, C. S. Hwang, and D.-S. Kim, Journal of Infrared, Millimeter, and Terahertz Waves **36**, 262-268 (2015).
27. W. Park, J. Rhie, N. Y. Kim, S. Hong, and D.-S. Kim, Scientific Reports **6**, 23823 (2016).
28. J. D. Jackson, *Classical electrodynamics* (Wiley, 1998).
29. J. S. Kyoung, M. A. Seo, H. R. Park, K. J. Ahn, and D. S. Kim, Optics Communications **283**, 4907-4910 (2010).
30. E. Burstein, Y. J. Chen, C. Y. Chen, S. Lundquist, and E. Tosatti, Solid

State Communications **29**, 567-570 (1979).

31. B. N. J. Persson, Chemical Physics Letters **82**, 561-565 (1981).
32. S. Nie, and S. R. Emory, Science **275**, 1102-1106 (1997).
33. H. Xu, E. J. Bjerneld, M. Käll, and L. Börjesson, Physical Review Letters **83**, 4357-4360 (1999).
34. S. A. Maier, Opt. Express **14**, 1957-1964 (2006).
35. D. Bar-Lev, and J. Scheuer, Opt. Express **21**, 29165-29178 (2013).
36. G. F. Walsh, and L. Dal Negro, Nano Letters **13**, 3111-3117 (2013).
37. C. K. Chen, T. F. Heinz, D. Ricard, and Y. R. Shen, Physical Review B **27**, 1965-1979 (1983).
38. P. Stefano, D. Matthias, and N. Lukas, Journal of Optics A: Pure and Applied Optics **11**, 114030 (2009).
39. R. S. Mahi, Nanotechnology **24**, 125701 (2013).
40. P. Johnson, and R. Christy, Physical Review B **6**, 4370-4379 (1972).
41. B. Prade, J. Y. Vinet, and A. Mysyrowicz, Physical Review B **44**, 13556-13572 (1991).
42. R. W. Wood, Proc. R. Soc. London, Ser. A **18**, 269–275 (1902).
43. M. Sarrazin, J.-P. Vigneron, and J.-M. Vigoureux, Physical Review B **67**, 085415 (2003).
44. H. Lochbihler, and R. A. Depine, Appl. Opt. **51**, 1729-1741 (2012).
45. A. D. Rakić, A. B. Djurišić, J. M. Elazar, and M. L. Majewski, Appl. Opt. **37**, 5271-5283 (1998).
46. T. B. A. Senior, Appl. sci. Res. **8**, 418-436 (1960).
47. H. Lochbihler, and R. Depine, Appl. Opt. **32**, 3459-3465 (1993).
48. F. García-Vidal, and L. Martín-Moreno, Physical Review B **66**, 155412 (2002).
49. S. A. Maier, *Plasmonics: Fundamentals and applications* (Springer, 2007).
50. M. D. Groner, J. W. Elam, F. H. Fabreguette, and S. M. George, Thin

Solid Films **413**, 186-197 (2002).

51. S. Han, Y.-M. Bahk, N. Park, and D.-S. Kim, Opt. Express **24**, 2065-2071 (2016).
52. K. Yoshioka, Y. Minami, K.-i. Shudo, T. D. Dao, T. Nagao, M. Kitajima, J. Takeda, and I. Katayama, Nano Letters **15**, 1036-1040 (2015).
53. A. Mooradian, Physical Review Letters **22**, 185-187 (1969).
54. A. Zhang, J. Zhang, and Y. Fang, Journal of Luminescence **128**, 1635-1640 (2008).
55. A. Baltuska, T. Udem, M. Uiberacker, M. Hentschel, E. Goulielmakis, C. Gohle, R. Holzwarth, V. S. Yakovlev, A. Scrinzi, T. W. Hansch, and F. Krausz, Nature **421**, 611-615 (2003).
56. P. Eckle, A. N. Pfeiffer, C. Cirelli, A. Staudte, R. Dörner, H. G. Muller, M. Büttiker, and U. Keller, Science **322**, 1525-1529 (2008).
57. P. S. Davids, R. L. Jarecki, A. Starbuck, D. B. Burckel, E. A. Kadlec, T. Ribaudo, E. A. Shaner, and D. W. Peters, Nat Nano **10**, 1033-1038 (2015).
58. Z. Zixu, J. Saumil, G. Sachit, and M. Garret, Journal of Physics D: Applied Physics **46**, 185101 (2013).
59. E. W. Cowell, N. Alimardani, C. C. Knutson, J. F. Conley, D. A. Keszler, B. J. Gibbons, and J. F. Wager, Advanced Materials **23**, 74-78 (2011).
60. T. Rybka, M. Ludwig, M. F. Schmalz, V. Knittel, D. Brida, and A. Leitenstorfer, Nat Photon **10**, 667-670 (2016).
61. A. Schiffrin, T. Paasch-Colberg, N. Karpowicz, V. Apalkov, D. Gerster, S. Muhlbrandt, M. Korbman, J. Reichert, M. Schultze, S. Holzner, J. V. Barth, R. Kienberger, R. Ernstorfer, V. S. Yakovlev, M. I. Stockman, and F. Krausz, Nature **493**, 70-74 (2013).
62. W. P. Putnam, R. G. Hobbs, P. D. Keathley, K. K. Berggren, and F. X. Kärtner, Nat Phys **13**, 335 (2016).
63. R. H. Fowler, and L. Nordheim, Proceedings of the Royal Society of London. Series A **119**, 173-181 (1928).
64. J. G. Simmons, Journal of Applied Physics **34**, 2581-2590 (1963).

65. H. Sigg, P. Wyder, and J. A. A. J. Perenboom, Physical Review B **31**, 5253-5261 (1985).

66. C. Faugeras, G. Martinez, A. Riedel, R. Hey, K. J. Friedland, and Y. Bychkov, Physical Review Letters **92**, 107403 (2004).

67. E. Hendry, F. Wang, J. Shan, T. F. Heinz, and M. Bonn, Physical Review B **69**, 081101 (2004).

68. A. J. Sievers, and M. Tinkham, Physical Review **129**, 1566-1571 (1963).

69. J. Nishitani, K. Kozuki, T. Nagashima, and M. Hangyo, Applied Physics Letters **96**, 221906 (2010).

70. J. B. Baxter, and G. W. Guglietta, Analytical Chemistry **83**, 4342-4368 (2011).

71. H. Y. Fan, Reports on Progress in Physics **19**, 107 (1956).

72. B. Donovan, and N. H. March, Proceedings of the Physical Society. Section B **70**, 883 (1957).

73. R. A. Lewis, I. V. Bradley, and M. Henini, Solid State Communications **122**, 223-228 (2002).

74. R. Kostic, and D. Stojanovic, "Nonlinear absorption spectra for intersubband transitions of cdse/zns spherical quantum dots," (SPIE2011), p. 10.

75. S. L. Norman, Physical Review **167**, 393-407 (1968).

76. M. van Exter, C. Fattinger, and D. Grischkowsky, Opt. Lett. **14**, 1128-1130 (1989).

77. H. Harde, and D. Grischkowsky, J. Opt. Soc. Am. B **8**, 1642-1651 (1991).

78. H. Harde, S. Keiding, and D. Grischkowsky, Physical Review Letters **66**, 1834-1837 (1991).

79. M. Hangyo, M. Tani, and T. Nagashima, International Journal of Infrared and Millimeter Waves **26**, 1661-1690 (2005).

80. P. U. Jepsen, D. G. Cooke, and M. Koch, Laser & Photonics Reviews **5**, 124-166 (2011).

81. J. Hebling, G. Almási, I. Z. Kozma, and J. Kuhl, Opt. Express **10**, 1161-

1166 (2002).

82. K.-L. Yeh, M. C. Hoffmann, J. Hebling, and K. A. Nelson, Applied Physics Letters **90**, 171121 (2007).

83. A. G. Stepanov, L. Bonacina, S. V. Chekalin, and J.-P. Wolf, Opt. Lett. **33**, 2497-2499 (2008).

84. H. Hirori, A. Doi, F. Blanchard, and K. Tanaka, Applied Physics Letters **98**, 091106 (2011).

85. P. C. M. Planken, H.-K. Nienhuys, H. J. Bakker, and T. Wenckebach, J. Opt. Soc. Am. B **18**, 313-317 (2001).

86. D. Lee, and D.-S. Kim, Scientific Reports **6**, 18935 (2016).

87. J. G. Simmons, Journal of Applied Physics **35**, 2472-2481 (1964).

88. J.-Y. Kim, B. J. Kang, Y.-M. Bahk, Y. S. Kim, J. Park, W. T. Kim, J. Rhie, S. Han, H. Jeon, C.-H. Park, F. Rotermund, and D.-S. Kim, Scientific Reports **6**, 29103 (2016).

89. S. Han, J.-Y. Kim, T. Kang, Y.-M. Bahk, J. Rhie, B. J. Kang, Y. S. Kim, J. Park, W. T. Kim, H. Jeon, F. Rotermund, and D.-S. Kim, ACS Photonics **3**, 1440-1445 (2016).

90. K. J. Savage, M. M. Hawkeye, R. Esteban, A. G. Borisov, J. Aizpurua, and J. J. Baumberg, Nature **491**, 574 (2012).

91. T. Kang, J. Rhie, J. Park, Y.-M. Bahk, J. Sung Ahn, H. Jeon, and D.-S. Kim, Applied Physics Express **8**, 092003 (2015).

92. P. Zhang, Scientific Reports **5**, 9826 (2015).

요약

본 논문에서는 나노미터 크기로 이루어진 금속-절연체-금속 구조에서의 빛과 물질간의 강한 상호작용에 관해 탐구하였다. 제작된 나노갭은 키르히호프 적분정리 및 간섭계를 바탕으로 한 광학적 투과실험을 통해 평가되었다. 가시광 및 근적외선 영역의 전기장 성분이 나노갭에서 내부에서 약 열 배 정도 증폭됨을 관측하였고, 나노갭에서의 도파로 모드에 의한 패브리-페로 공명특성을 보이는 것을 확인하였다. 빛의 전기장과 금속 나노갭 간의 강한 상호작용은 갭을 투과하는 빛 또는 금속자체의 형광 신호를 매우 크게 증폭시킴을 확인하였다. 갭에 걸리는 전기장의 크기가 1 V/nm 영역까지 커질 경우 양자 터널링 현상이 나타났고, 그에 따른 나노갭에서의 광학적 응답특성을 매우 크게 변화시켰다. 나는 닫힌 양자터널장벽 구조에서 기인하는 거시적 대칭특성을 이용하여 전자기적으로 유도된 초고속 터널링 전류를 일반적인 전자기기를 통해 정량적으로 측정하였다. 고리나노갭 구조에 입사된 강한 테라파가 완전-정류됨을 확인하였고, 광학적 방법을 통해 테라헤르츠 터널링 전류의 시공간적 특성을 가시적으로 보였다. 본 연구는 초고속 광전자학, 테라파 멀티플렉싱, 초고대역폭 통신기술 및 무선에너지 전송 등의 연구에 응용이 될 것으로 기대한다.

주요어: 광학적 전기장 증폭현상, 나노갭, 비선형 광학, 전자 터널링, 테라파 정류
학번: 2011-20387

Keywords : optical field enhancement, nanogap, nonlinear optics, electron tunneling, terahertz rectification.
Student Number : 2011-20387